A MEASUREMENT OF THE RATE OF MUON CAPTURE IN AN ULTRA-PURE PROTIUM GAS TIME PROJECTION CHAMBER

BY

BRENDAN E. KIBURG

DISSERTATION

Submitted in partial fulfillment of the requirements
for the degree of Doctor of Philosophy in Physics
in the Graduate College of the
University of Illinois at Urbana-Champaign, 2011

Urbana, Illinois

Doctoral Committee:

Professor Kevin T. Pitts, Chair
Professor David W. Hertzog, Co-Director of Research
Research Professor Peter Kammel, Co-Director of Research
Professor James N. Eckstein
Professor Scott S. Willenbrock

Abstract

The MuCap experiment is designed to measure the disappearance rate of negative muons in an ultra-pure protium gas to a precision of 15 ppm using a time projection chamber (TPC). Combined with precise knowledge of the rate of free muon decay, this determines the capture rate for the μp atom in the singlet hyperfine state, Λ_S, with a precision of 1%. The experimental conditions suppress sensitivity to the poorly known molecular transition rate, λ_{op}, which allows for an unambiguous determination of the proton's pseudoscalar coupling, g_P, with a precision of 6.5%. Chiral perturbation theory makes a precise calculation, $g_P = 8.26 \pm 0.23$, so a comparison with MuCap's experimental determination of g_P will probe our understanding of low-energy QCD and its underlying symmetries.

This dissertation begins with the motivation for the measurement and a summary and brief analysis of previous efforts. The critical role played by the molecular kinetics is described, especially as it is relevant to the design of MuCap and to the analysis of the data. The experimental apparatus and hardware upgrades implemented for the 2007 data collection period are described. The analysis methods are optimized to minimize effects caused by muon physics processes as well as subtle effects caused by interference between muon track and electron signals in the TPC gas. The stability of the disappearance rate with respect to the analysis choices is demonstrated. The remaining systematic studies are summarized, and a relative comparison of Λ_S between the 2006 and 2007 data sets is reported. The full statistics of 1.5×10^{10} μ^- decays has been collected and analyzed, and a final unblinding of the data will take place in 2011. The final steps to extract g_P with a precision of $\delta g_P = 0.54$ from the measured capture rate, Λ_S, are detailed.

To my dear friends and family.

Acknowledgments

The work described in this thesis would not have been possible without the significant efforts of the MuCap collaboration. I am grateful to have had the opportunity to work with scientists from a diverse set of backgrounds, and I believe the collaborative experience has helped shape me as a researcher. Many people have contributed to the experimental effort, from the proposal planning through the analysis of the data, and it is a pleasure to thank the members of our international collaboration that made this thesis possible: V.A. Andreev, T. I. Banks, R.M. Carey, T.A. Case, D.B. Chitwood, S.M. Clayton, K.M. Crowe, J. Deutsch, J. Egger, S.J. Freedman, V.A. Ganzha, T. Gorringe, F.E. Gray, D.W. Hertzog, M. Hildebrandt, P. Kammel, S. Knaack, P.A. Kravtsov, A.G. Krivshich, B. Lauss, K.R. Lynch, E.M. Maev, O.E. Maev, F. Mulhauser, C.S. Özben, C. Petitjean, G.E. Petrov, R. Prieels, G.N. Schapkin, G.G. Semenchuk, M.A. Soroka, V. Tishchenko, A.A. Vasilyev, A.A. Vorobyov, M. Vznuzdaev and P. Winter.

Throughout the data collection periods at PSI, I received excellent laboratory guidance from a variety of collaborators from other institutions. For those experiences, I thank Rob Carey, Kevin Giovanetti, Tim Gorringe, Malte Hildebrandt, Bernard Lauss, and Claude Petitjean.

Several sets of individuals have been part of the precision muon physics group at Illinois during my time as a graduate student. I extend a thanks to Dan Chitwood, Steven Clayton, Jason Crnkovic, Fred Gray, Sara Knaack, Chris Polly, Noah Schroeder and David Webber, all of whom shared the graduate student experience with me at Illinois. I thank the post-docs, visiting scientists and professors for providing senior leadership: Paul Debevec,

David Hertzog, Peter Kammel, Serdar Kizilgul, Francoise Mulhauser, Ron McNabb, Gerco Onderwater, Cenap Özben and Peter Winter. I thank Penny Sigler for her tireless dedication to the group. I am honored to thank Peter Winter and offer my gratitude for his technical guidance in my analysis efforts, advice on my thesis writing and thesis editing, as well as his personal and professional guidance as a friend. I thank my advisors David Hertzog and Peter Kammel, who patiently helped me develop a wide range of skills in detector hardware, data analysis, and conference presentations as well as precision muon physics and the broader field of particle physics.

In my personal life, I owe my gratitude to Liz for her enthusiastic support, optimism and unending patience as I have forged this path. I thank Mom and Dad for nurturing my curiosity of the world and encouraging me to explore it and define my own goals. I wish to thank Nicole, Brian and Natalie for always being supportive of their brother. The research has taken me far from home, and I have missed a few holidays, birthdays and anniversaries. Finally, I thank a set of people that started out as a casual social group and have become another family for me at Illinois: Bob, Brad, Charlie, Chris, Dave, Jason, Kevin, Mike, Nick, Noah, Pat, Peter, Q, and Rob. I am profoundly grateful for my friends and family, who have always supported my decisions and actively encouraged my efforts.

I thank the Felix T. Adler fellowship committee at the University of Illinois Urbana-Champaign for the recognition of my research in 2010.

Funding for the University of Illinois at Urbana-Champaign Nuclear Physics Group is provided by the National Science Foundation under grant #0855569, and CRDF. The analysis effort was partially supported by the National Center for Supercomputing Applications under the research allocation TG-PHY060011N. The MuCap experiment utilized the MSS systems and developed and executed analysis code on the tungsten and abe analysis clusters at NCSA.

Table of Contents

Chapter 1

Introduction

The muon burst onto the physics scene in 1936 when Carl Anderson and his graduate student Seth Neddermeyer first observed the tracks of the particle while studying properties of cosmic rays in a cloud chamber [1]. Yukawa's theory of mesons predicted a strongly interacting particle with a similar mass, and initially the muon was believed to be this particle [2]. However, the muon does not participate in strong interactions and it quickly became apparent that the observed particle was something new. Robert Marshak and Hans Bethe subsequently postulated that the observed tracks were not Yukawa's particle, but rather a secondary particle born from the meson [3]. Murray Gell-Mann's classification of the era as a "period of confusion" [4] and Rabi's famous quip "Who ordered that?" [5] succinctly represent that the muon had no obvious theoretical role in physics in the early 1940s.

The muon is a spin-$\frac{1}{2}$, charged particle. With a mass $m_\mu = 106$ MeV/c^2, the muon is about 207 times heavier than the electron, but is relatively light compared to other known particles [6]. Unlike the electron, it is unstable, and decays with a characteristic lifetime of about 2.2 μs. This is measured by observing the decay rate of the positively charged muons:

$$\mu^+ \rightarrow e^+ + \nu_e + \bar{\nu}_\mu. \tag{1.1}$$

After the basic properties of the muon were established, electrons, muons and neutrinos were properly placed together in the tables of fundamental particles and the concept of multiple lepton generations was born. Leptons are fermionic particles that are sensitive to

the electromagnetic force, gravity and the weak force, but insensitive to the strong force. The electrically charged leptons, from lightest to heaviest, consist of three "flavors": electron (e), muon (μ) and tau (τ). Each lepton flavor has a corresponding electrically neutral light partner neutrino: ν_e, ν_μ and ν_τ. The neutrinos in process (1.1) are the particles postulated by Pauli to satisfy conservation of momentum and energy. Furthermore, two neutrino flavors are required to satisfy the empirically observed lepton flavor conservation in nature.

The understanding of the muon has undergone a major transition in the last 60 years, evolving from an unexpected guest in the cloud chamber to a fundamental probe in many aspects of particle physics. One of the earliest scientific measurements using the muon was the demonstration of the time-dilation component of Einstein's Theory of Relativity [7]. The flux of muons from cosmic rays was measured on the 6265-ft tall Mt. Washington in New Hampshire and compared to the flux at sea level in Cambridge MA. The experiment stopped the cosmic muons and ensured the particles were actually muons by measuring their lifetime. Since these cosmic rays take about 6.4 μs to travel 6265 feet, simple exponential decay predicts a survival probability of $\approx 5\%$. However, the ratio of the flux at sea level to the flux on the mountain top demonstrated that over 70% of the muons survived. This large surplus of surviving muons confirmed that their internal clock runs slower due to time-dilation.

1.1 Muon Decay and Capture

The muon has been used to characterize properties of the Standard Model of particle physics, which describes the interactions of quarks and leptons via electromagnetic, weak and strong interactions. The weak force is responsible for two of the muon's most fundamental and interesting reactions: muon decay and muon capture. The primary decay mode for the

negative muon is given by the equivalent to process (1.1)

$$\mu^- \rightarrow e^- + \nu_\mu + \bar{\nu}_e. \tag{1.2}$$

Negative muons can also be captured by a proton:

$$\mu^- + p \rightarrow n + \nu_\mu. \tag{1.3}$$

The muon plays an essential role in shaping the understanding of the weak interaction, as both of these processes can be described to high precision within the Standard Model. The muon's unique properties of a light mass and relatively long lifetime make it an excellent particle for studying fundamental processes. The MuLan collaboration recently made a 1 part-per-million (ppm) measurement of the positive muon lifetime and produced a high-precision determination of the Fermi constant: [8]

$$G_F = 1.1663788(7) \times 10^{-5}\ \text{GeV}^{-2}. \tag{1.4}$$

G_F is essentially the strength of the weak interaction; the larger it is, the faster weak processes proceed. While there are other weak interactions that allow the extraction of G_F, the muon lifetime allows for the cleanest theoretical interpretation and is the most sensitive by far. A comparison of the Fermi constant from various processes allows for a stringent test of the universality of the weak interaction [9].

The MuCap experiment described in this thesis determines the proton's pseudoscalar form factor, g_P. This basic quantity can be precisely calculated within the Standard Model, so comparison with experiment would establish an important test of low-energy QCD and chiral symmetries [10]. The rate of process (1.3), Λ_S, is related through the theory of the weak interaction to the strength of the proton's form factors: the vector $g_V(q^2)$, axial vector $g_A(q^2)$, weak magnetism $g_M(q^2)$, and pseudoscalar $g_P(q^2)$. At the momentum transfer

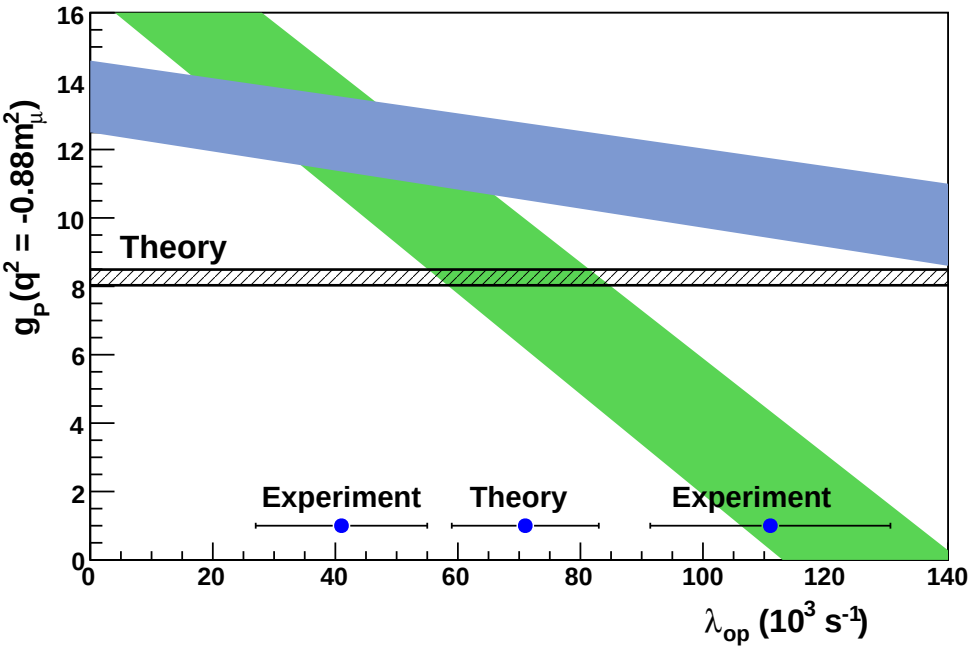

Figure 1.1: Dependence of g_P on the muon chemistry parameter λ_{op}. The value for g_P as a function of λ_{op} is shown for the two most precise experiments, prior to MuCap. Two measurements and a theoretical prediction for λ_{op} are shown, and are mutually inconsistent. Depending on the value assumed for λ_{op}, a wide range of g_P values can be extracted, offering little comparative power with the precise theoretical prediction.

relevant to process (1.3), $q_0^2 = -0.88m_\mu^2$, the form factors $g_V(q_0^2)$, $g_M(q_0^2)$ and $g_A(q_0^2)$ are well determined by other experiments and Standard Model symmetries [11]. There is a rich history of measurements that have extracted the pseudoscalar coupling from muon capture experiments. However, the experimental determination of g_P relies on precise knowledge of the atomic or molecular state from which the muon captured, which has resulted in an experimentally puzzling situation over the past 50 years. Experimental efforts usually report g_P as a function of a difficult to measure muon chemistry parameter, λ_{op}. Figure 1.1 shows the experimental dependency of g_P on λ_{op} for the two most precise results, prior to MuCap.

The history of conflicting measurements of λ_{op} will be examined in more detail in Section 3.1.1. For now, Figure 1.1 illustrates that the uncertainties in λ_{op} decisively affect the interpretation of experimental results. A mutually consistent comparison between the theoretical prediction and the experimental determination of g_P is not possible. Accounting

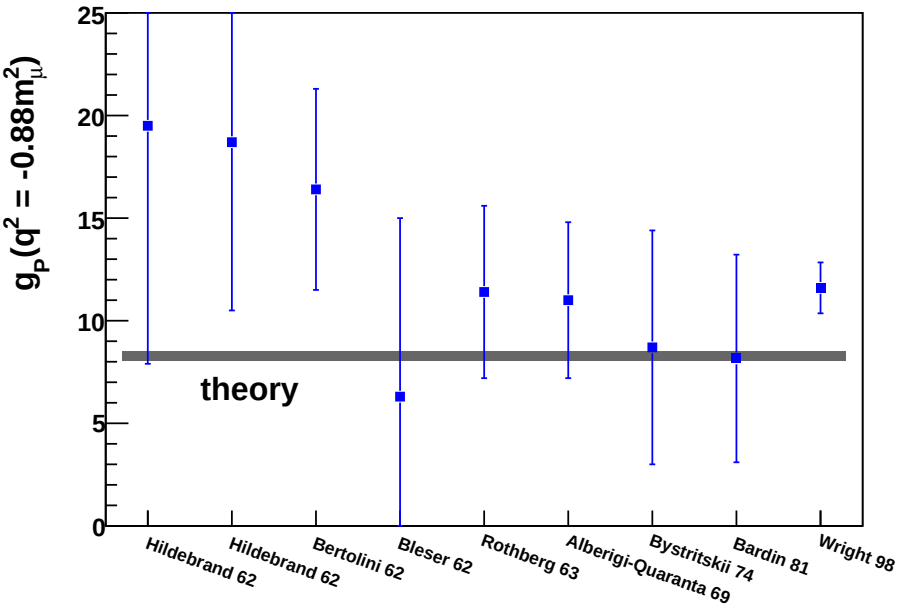

Figure 1.2: Extraction of g_P from experimental results. The historical values are shown prior to the MuCap experiment. Values have been updated to reflect recent improvements in theory [12] and as well as new data that affects the interpretation [13]. The values shown are calculated in the review of precision muon capture [11].

for the large uncertainty in λ_{op}, extractions of g_P from previous experimental efforts are shown in Figure 1.2. The fundamental nature of g_P and the ambiguous interpretation of experiments motivate an updated effort.

The MuCap experiment was designed to have low sensitivity to λ_{op}. An initial production data set was analyzed and first results were published for the capture rate of process (1.3) [14],

$$\Lambda_S = 725.0 \pm 13.7_{\text{stat}} \pm 10.7_{\text{syst}} \text{ s}^{-1}, \tag{1.5}$$

and the pseudoscalar coupling constant,

$$g_P \equiv g_P(q_0^2) = 7.3 \pm 1.1, \tag{1.6}$$

which are in good agreement with theoretical predictions.[1] Significant hardware developments have been made to reduce systematic uncertainties and increase the data rate to achieve the full statistics goals of 1.5×10^{10} muon decays in 2006 and 2007. This thesis describes the experimental procedure, data collection and analysis techniques necessary to analyze the full statistics. This analysis will produce our final, precise and unambiguous determination of g_P to compare with theory.

1.2 Other Current Topics in Muon Physics

Before discussing my thesis topic in detail, I will briefly summarize the versatility of the muon for fundamental and applied topics in current research. In addition to illuminating fundamental constants, the muon allows scientists to probe for physics beyond the standard model (BSM) [15]. The g - 2 experiments have studied the muon's magnetic moment, $\vec{\mu}_\mu$, which is related to the muon's spin by the expression

$$\vec{\mu}_\mu = g_\mu \frac{e}{2m_\mu} \vec{S}. \tag{1.7}$$

Here, $\vec{S}$ is the muon spin, e is the electric charge, m_μ is the muon mass and g_μ is the Landé g-factor [16]. Since the muon has no internal structure, the Dirac theory predicts that $g_\mu \equiv 2$. However, basic quantum electrodynamic (QED) processes account for a small deviation from $g_\mu = 2$, expressed as $a_\mu = \frac{g_\mu - 2}{2}$. The technique used in the recent g - 2 experiment at Brookhaven National Lab (BNL) [17] and the proposed New g - 2 at Fermi National Accelerator Lab (FNAL) [18] is to inject polarized muons into a storage ring and observe the spin precession. The beat frequency between the cyclotron frequency and the spin precession frequency can be directly attributed to the anomalous magnetic moment. The world average for a_μ disagrees with theoretical predictions at the 3.6σ level [19]. The

[1] The values in equations (1.5) and (1.6) are from the PRL [14], and have not been updated to account for the recent MuLan measurement of the positive muon lifetime. That measurement shifts these results into even better agreement with theory, and will be recomputed and discussed in Chapter 8.

ongoing efforts to improve both theory and experiment are critical for understanding BSM models. On the eve of potential discoveries at the LHC, the muon's anomalous magnetic moment will prove to be a critical tool in interpreting those findings. While the LHC will be sensitive to most weak-scale extensions to the SM, the BSM contributions of additional terms to g - 2 vary from model to model.

The g - 2 experiments also include searches for non-zero, muon electric-dipole moments (EDMs). [20] Any intrinsic, non-zero EDM for the muon would violate both time and parity symmetry. While standard model EDMs are permissible, they are predicted to be extremely small. Measurements of either an anomalous magnetic moment that disagrees with QED or a non-zero EDM in these modern experiments would be clear evidence of BSM physics [15,20].

A new generation of experiments is also underway to probe the current limits of lepton flavor violation. Within the Standard Model, each lepton generation has been observed to have its own conservation number: L_e, L_μ and L_τ. In a lepton flavor violating (LFV) process, the individual lepton numbers in the initial and final states are different.[2] The mu-e-gamma experiment (MEG) at PSI is searching for neutrinoless, radiative muon decay: $\mu^+ \to e^+\gamma$ [21]. In contrast to process (1.2), no neutrinos are emitted; instead, a γ particle allows for conservation of energy and momentum. The decay particles are emitted back to back with energy equal to half of the muon mass. A liquid Xenon calorimeter is used to observe the gamma, and the positron is deflected by a solenoidal magnetic spectrometer and tracked with a series of wire chambers. These methods allow for a precise reconstruction of the positron and photon energies. The presence of a signal at the proposed sensitivity of 10^{-13} would be a clear indication of BSM physics [22].

Another search for LFV is underway in the proposed muon to electron conversion experiment (Mu2e) at FNAL, which searches for the process $\mu^- N \to e^- N$ [23]. In this case, the presence of a nucleus is required to account for momentum conservation in the neutrinoless

[2]Neutrino oscillation is a well documented process by which, in principle, one could observe a LFV SM process. However, branching ratios for LFV processes via neutrino oscillation are at the 10^{-54} level, about 40 orders of magnitude smaller than the branching ratios of the processes discussed in this section.

reaction. The converted electron would then be detected with an energy equal to the muon mass, and tracked and measured with a calorimeter. The individual lepton numbers are not conserved and, in the absence of any BSM physics, this process should not occur at any appreciable rate. Many extensions of the standard model predict rates comparable to the current limits [24]. In the supersymmetric (SUSY) models, muon conversion would involve the exchange of neutralinos. To achieve sensitivity to these tiny signals, both MEG and Mu2e have to suppress large backgrounds. However, the discovery of LFV reactions would be a major scientific achievement, as they would reveal direct evidence of BSM physics and help to constrain the competing models.

The muon has also been instrumental in creating a new field of applied physics called μSR[3] (muon-spin-rotation) that characterizes magnetic properties of materials [25]. In these measurements, a polarized beam of positive muons is stopped in a magnetic target material. Because the muon is a spin-$\frac{1}{2}$ particle, it will undergo a Larmor precession in the presence of a magnetic field. As a consequence of the weak interaction being parity violating, when the positive muon decays, the positron is emitted preferentially in the direction of the muon spin. An analysis of the decay direction versus time for ensembles of muons stopped in these targets allows for the characterization of the internal magnetic properties of the material.

Muons have also been used to probe the structure of nucleons. A recent measurement of the energy difference between the $2S_{1/2}$ and $2P_{1/2}$ states (the Lamb Shift) in muonic hydrogen allowed for the extraction of the charge radius of the proton [26]. Since the muon is about 200 times heavier than an electron, a μp system has a much smaller Bohr radius than a hydrogen atom. This more tightly bound system is more sensitive to the effective size of the proton. A triggered laser system was used to excite metastable muonic hydrogen atoms from their $2S$ to the $2P$ state and the subsequent X-ray emitted as the atom de-excited to the ground state was measured. By scanning over a laser frequency range, the appropriate Lamb shift energy splitting was determined and a new value of the proton charge radius has

[3] μSR stands for muon-spin-rotation, relaxation or resonance, depending on the exact application.

been extracted: $r_p = 0.84184(67)$ fm. This measurement has triggered significant attention from the community, as its value was 5 sigma smaller than the CODATA determination of r_p [27].

1.3 Summary

Overall, the muon has been used to probe many areas of modern physics. The muon has helped verify time-dilation, and allowed for the determination of fundamental parameters in the Standard Model like G_F and the proton charge radius. Measurements of the anomalous magnetic moment and searches for non-zero EDMs have been used to constrain BSM physics and probe QED. New experiments are underway to search for LFV that will test models like SUSY. Muons have been used to characterize magnetic materials and will almost certainly be used in applications that scientists are just beginning to explore [28–30].

I now return the focus to our experiment, MuCap, which uses muons to probe the weak axial current of the proton. The muon capture process was one of the earliest muon processes that was studied, and our modern experiment revisits the subject.[4]

[4]A glossary of commonly used terms can be found in Appendix A.

Chapter 2

Weak Interaction Physics

The theory of weak interactions was first conceived by Enrico Fermi in the 1930s in an effort to explain neutron beta decay, $n \to p + e^- + \bar{\nu}_e$, as shown in Figure (2.1a).[1] Fermi proposed a Hamiltonian that directly coupled hadronic and leptonic currents without a propagator, which is a very reasonable formulation for the low-energy regime. The modern theory of weak interactions of Glashow, Salam, Weinberg (GSW) includes massive charged bosons (W^+ and W^-) and a neutral boson (Z) with masses of 80 GeV/c^2 and 91 GeV/c^2 respectively. Figure (2.1b) displays the Feynman diagram for neutron beta decay in the modern formulation. The energy scale of beta decay is very small compared to the mass of the W^- boson, so the effective range of the interaction is tiny and the contact interaction approach described by Fermi is essentially correct.

Fermi modeled his theory on the electromagnetic interaction and its familiar vector current and wrote the Hamiltonian,

$$\mathcal{H}_W = \frac{G_\beta}{2} \bar{\psi}_e \gamma^\mu \psi_\nu \bar{\psi}_p \gamma_\mu \psi_n. \tag{2.1}$$

However, this initial attempt only included vector terms in the charged currents. A priori, the full expression could contain any Lorentz-invariant combination of vector, axial-vector, scalar, tensor and pseudoscalar, all of which were explored theoretically or experimentally [31].

A breakthrough occurred with the definitive experiment of Wu et al. in 1957 which stud-

[1] Throughout this document, I use the convention that time is oriented horizontally, with particles having forward arrows, and antiparticles having backward arrows.

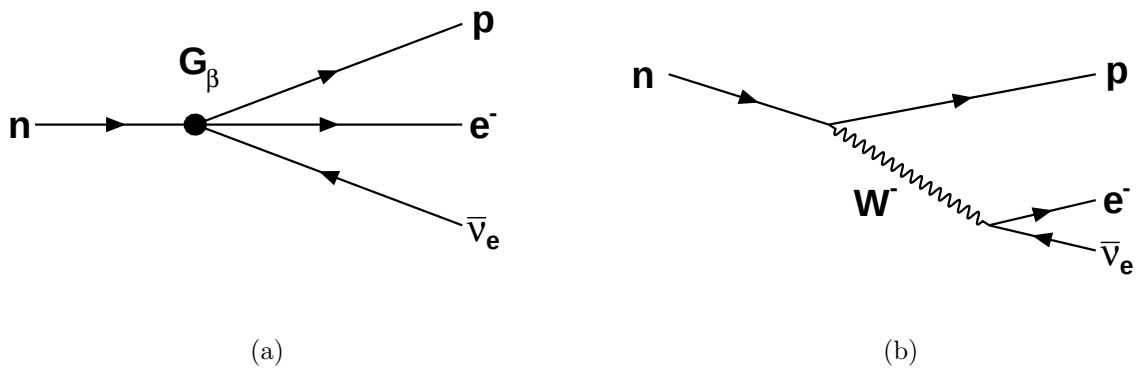

(a) (b)

Figure 2.1: Neutron beta decay diagrams shown for (a) Fermi's point interaction theory (b) The Standard Model with the W^- boson propagator.

ied the β decay of ^{60}Co nuclei [32]. Polarized cobalt atoms were aligned in a magnetic field and the direction of the decay electron was observed. By comparing the electron momentum and cobalt spin angular momentum coupling, this experiment was able to determine the effect of the parity operator on the weak hamiltonian. The parity operator, $\hat{P}$ inverts vectors taking each coordinate $\hat{P}\vec{x}_i \rightarrow -\vec{x}_i$. However, angular momenta arise as the cross product of two vectors, so although the parity operator changes the sign of each vector individually, the overall product is unchanged ($\hat{P}\vec{s}_i \rightarrow \vec{s}_i$). Thus, for the beta decay process to be parity conserving, there cannot be any difference in rate between electrons emitted parallel and antiparallel to the spin direction.

Wu found that the electrons were emitted preferentially in the direction opposite of the spin of the cobalt, demonstrating that the weak interaction is parity violating. This observation constrained the possible descriptions of the current-current weak interaction. Further experiments determined that the spin and momentum vectors are antiparallel for real leptons.[2] This configuration is known as left-handed or left-chiral, which is a "vector minus axial vector" coupling – usually written as "V-A". As a result, the modern theory has slightly modified Fermi's original formulation of the weak interaction to reflect its empirical

[2]The spin and momentum vectors are aligned for antiparticles.

"V-A" nature.

2.1 Free Muon Decay

The dominant decay mode for a free, negative muon is

$$\mu^- \rightarrow e^- + \nu_\mu + \bar{\nu}_e. \tag{2.2}$$

Because the muon is light compared to the W boson, this process can be interpreted through Fermi's point interaction theory. The decay rate is simply expressed as

$$\lambda_0 = \frac{1}{\tau_\mu} = \frac{G_F^2 m_\mu^5}{192\pi^3}(1 + \Delta q), \tag{2.3}$$

where G_F is the Fermi constant, m_μ is the muon mass and Δq includes well determined QED, phase space and hadronic radiative corrections. G_F gives the overall scale of the strength of the weak interaction and can be expressed as

$$G_F = \frac{\sqrt{2}g^2}{8M_W^2}(1 + \Delta r), \tag{2.4}$$

where g is the bare electroweak coupling constant, M_W is the mass of the W boson and Δr represents radiative corrections. An improved value for G_F has been determined recently by the MuLan collaboration by measuring the positive muon lifetime, $\tau_{\mu^+} = 2196980.3 \pm 2.2$ ps (1.0 ppm) [8], which corresponds to a free decay rate of $\lambda_{\mu^+} = 455170.2 \pm 0.5$ s^{-1}. The updated world average is $G_F = 1.1663788(7) \times 10^{-5}$ GeV^{-2}.

Rare decays such as radiative muon decay ($\mu^- \rightarrow e^- + \nu_\mu + \bar{\nu}_e + \gamma$) and pair production ($\mu^- \rightarrow e^- + \nu_\mu + \bar{\nu}_e + e^+ + e^-$) are included in the full expression relating G_F to the decay rate, λ_0.

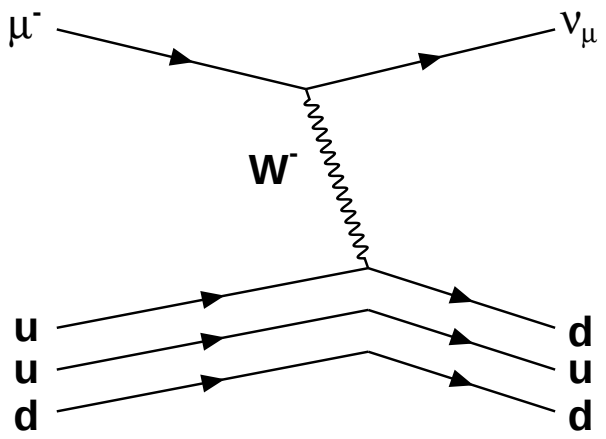

Figure 2.2: Tree-level Feynman diagram for equation (2.5), with time running horizontally. A W boson is exchanged between the muon and one of the proton's up quarks, resulting in a neutrino and a neutron in the final state. The spectator quarks are included as a cue that this process occurs in a hadronic environment, and a full description must reflect that.

2.2 Muon Capture

In the presence of a proton, additional disappearance channels are available to the negative muon. While the decay channel from process (2.2) dominates, (branching ratio (BR) = 0.9985) , the overlap between the muon's wavefunction and the proton's wavefunction allows for the possibility of nuclear capture through ordinary muon capture (OMC)

$$\mu^- + p \rightarrow n + \nu_\mu \ \ (BR = 1.5 \times 10^{-3}), \tag{2.5}$$

and radiative muon capture (RMC)

$$\mu^- + p \rightarrow n + \nu_\mu + \gamma \ \ (BR < 10^{-8}). \tag{2.6}$$

The tree-level Feynman diagram for process (2.5) is shown in Figure 2.2. The kinematics of this interaction uniquely determine the momentum transfer, $(q_n - q_p)^2 = q_\mu^2 = -0.88 m_\mu^2$. Because this momentum transfer is small compared to the weak scale, once again this reaction can be simplified to the Fermi point interaction, with a transition amplitude determined by

the matrix element

$$M_{fi} = \frac{G_F V_{ud}}{\sqrt{2}} L_\alpha J^\alpha. \tag{2.7}$$

Here, L_α and J^α are the leptonic and hadronic currents, and V_{ud} is a factor from the Cabibbo-Kobayashi-Maskawa (CKM) matrix which modifies the hadronic contribution to account for quark flavor coupling. For muon capture, the "V - A" nature of the weak interaction manifests itself in both currents. The leptonic term is given by $L_\alpha = \bar{u}_\nu \gamma_\alpha \left(1 - \gamma_5\right) u_\mu$ and the hadronic term is given by $J^\alpha = \bar{q}_d \gamma^\alpha \left(1 - \gamma^5\right) q_u$, where $\bar{u}_\nu$, u_μ, $\bar{q}_d$ and q_u are the neutrino, muon, down and up fields, respectively. However, the relevant quark is embedded in a nucleon, and the strong interaction is nonperturbative at the low energy associated with this process. Therefore, the hadronic current must be parametrized to account for these modifications. Replacing the quark level spinors with nucleon spinors, the most general weak hadronic current is fully expressed as

$$J^\alpha = \bar{u}_n \left(\underbrace{g_V \gamma^\alpha + \frac{i g_M}{2 m_N} \sigma^{\alpha\nu} q_\nu + \frac{g_S}{m_\mu} q^\alpha}_{V^\alpha} - \underbrace{g_A \gamma^\alpha \gamma_5 - \frac{g_P}{m_\mu} q^\alpha \gamma_5 - \frac{i g_T}{2 m_N} \sigma^{\alpha\nu} q_\nu \gamma_5}_{A^\alpha} \right) u_p, \tag{2.8}$$

with the first three terms comprising the vector current and the last three the axial vector current. The current is parametrized by the coupling constants $g_V(q_\mu^2)$, $g_M(q_\mu^2)$, $g_A(q_\mu^2)$, $g_P(q_\mu^2)$, $g_S(q_\mu^2)$ and $g_T(q_\mu^2)$, which are functions of the momentum transfer. The last two terms, $g_S(q_\mu^2)$ and $g_T(q_\mu^2)$ are referred to as second class-currents, and vanish in the limit that G-Parity[3] is a good symmetry of QCD. Any contribution to the current in equation (2.8) is limited to the scale of isospin symmetry breaking.

The vector form factor, $g_V(q_\mu^2)$, and weak-magnetic form factor, $g_M(q_\mu^2)$, are equivalent to the electromagnetic form factors of the nucleon by the conserved-vector-current (CVC) hypothesis. The CVC is a statement of conservation of weak charge stemming from $\partial_\alpha V^\alpha = 0$, where V^α is the vector current density in equation (2.8), and it requires the vector currents

[3]G-Parity is the product of charge conjugation and an isospin rotation.

to be conserved in both electromagnetic processes and the charged-current weak processes. Previous electron scattering experiments precisely determine these couplings which are then extrapolated to the momentum relevant for muon capture, $g_V(q_\mu^2) = 0.976 \pm 0.001$ and $g_M(q_\mu^2) = 3.583 \pm 0.003$ [11, 12]. The remaining axial-vector coupling constant, $g_A(q^2)$, and pseudoscalar coupling constant, $g_P(q^2)$, are determined experimentally from weak processes such as nuclear beta decay and muon capture. The momentum transfer of beta decay is very small, and the extracted $g_A(q^2 = 0) = 1.2695 \pm 0.0029$ is extrapolated to the momentum transfer associated with muon capture, $g_A(q^2 = -0.88m_\mu^2) = 1.247 \pm 0.004$ [11]. This leaves only the pseudoscalar undetermined.

In principle, several processes involving the nucleon weak axial current are sensitive to g_P. However, because the momentum transfer associated with nuclear beta decay is small, those experiments suppress the contributions of the $g_P q^\alpha$ term in equation (2.8). Neutrino scattering experiments are also potential candidates; however, direct detection of the neutrino is an obstacle that heavily suppresses the collection of statistics. Muon capture is the most practical process to study for the extraction of g_P.

Within the partially conserved axial current hypothesis (PCAC), g_P can be calculated by examining the current-current interaction in equation (2.8). The PCAC relates the divergence of the axial current, A^α, to the pion field, $\pi(x)$, which has the same quantum numbers: $\partial_\alpha A^\alpha \propto \pi(x)$. In the limit of a massless pion, the PCAC simplifies to a complete conservation of the axial vector current $\partial_\alpha A^\alpha = 0$. However, the pion is massive ($m_\pi \approx 140$ MeV/c^2), so evaluation of the PCAC equation at $q^2 = 0$ relates the axial coupling to parameters of the pion field. The result is the Goldberger-Treiman relation [10]:

$$g_A(0) = \frac{f_\pi g_{\pi NN}}{m_N}, \tag{2.9}$$

where m_N is the nucleon mass,[4] f_π is the pion weak coupling constant and $g_{\pi NN}$ is the

[4] $m_N \equiv (m_p + m_n)/2$

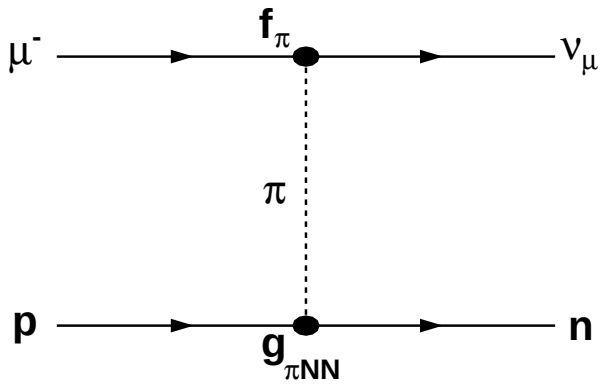

Figure 2.3: The QCD pion mediator is the dominant exchange diagram for muon capture.

strong-pion nucleon coupling. This pion exchange model is depicted for muon capture in Figure 2.3. The divergence of the axial current can also be evaluated for non-zero q^2 to relate g_P to g_A and physical constants[5]:

$$g_P(q^2) = \frac{2m_\mu m_N}{m_\pi^2 - q^2} g_A(0). \tag{2.10}$$

Evaluated at $q^2 = -0.88m_\mu^2$, equation (2.10) reduces to $g_P(-0.88m_\mu^2) = 6.77g_A(0) = 8.59$. It is convenient to define the pseudoscalar coupling at the momentum transfer of muon capture, $g_P \equiv g_P(-0.88m_\mu^2)$ for comparisons in Section 2.3 and for notational simplicity. There are higher order corrections that can be evaluated for this current-current interaction, but it is more interesting to examine the modern approach used to calculate g_P.

2.3 Chiral Perturbation Theory

Chiral perturbation theory (ChPT) is an effective field theory for QCD.[6] It is a low-energy expansion that incorporates the symmetries of QCD, and is used in the regime where the

[5]This assumes that the pion coupling is momentum-independent in the range between 0 and the pion mass.

[6]The specific class of ChPT when nucleons are involved is referred to as heavy baryon chiral perturbation theory (HBChPT).

external momenta (q) are much smaller than the chiral symmetry breaking scale, $\Lambda_\chi \sim$ 1 GeV. The systematic expansion in powers of q/Λ_χ contains several low-energy constants (LECs), which are free parameters that must be determined experimentally. The LECs parametrize the integrated effects of the high-energy physics for low-q processes. The nucleon and pion fields are the effective fields relevant in chiral perturbation theory.

ChPT predictions can be compared to the expressions from PCAC, and have the additional benefit of allowing systematic calculations of higher order:

$$g_P(q^2) = \frac{2m_\mu g_{\pi NN} f_\pi}{m_\pi^2 - q^2} - \frac{1}{3} g_A(0) m_\mu m_N r_A^2. \tag{2.11}$$

The leading order term in equation (2.11) reproduces the prediction of PCAC, and the second term accounts for the axial radius of the nucleon, r_A [33]. The result of ChPT calculations is a precise numerical prediction for the pseudoscalar coupling, g_P [10, 11, 33, 34]:

$$g_P^{\mathrm{ChPT}} = 8.26 \pm 0.23 \tag{2.12}$$

A comparison between an experimental determination of g_P and the prediction from ChPT is an important test of our understanding of QCD and its underlying symmetries.

2.4 Singlet Capture Rate

The rate of OMC in (2.5) depends on the hyperfine spin configuration of the atomic system. While in general a μp system has two spins available, experimental conditions are chosen in MuCap to populate primarily the singlet state.[7] The singlet capture rate is then calculated by inserting the hadronic current from equation (2.8) and the simpler lepton current L_α into equation (2.7) and squaring the matrix element [33]. The recent paper from Czarnecki [12]

[7] A correction will be applied in Chapter 8 to account for the small fraction of events that capture from the triplet configuration.

contains the full expression for the singlet capture rate:

$$\begin{aligned}\Lambda_S &= |\psi_\mu(0)|^2 \frac{G_F^2 |V_{\rm ud}|^2}{2\pi} \frac{E_\nu^2}{M^2} (M - m_n)^2 \\ &\cdot \left\{ \frac{2M - m_n}{M - m_n} g_V + \frac{2M + m_n}{M - m_n} g_A - \frac{g_P}{2} + (2M + 2m_n - 3m_\mu) \frac{g_M}{4m_N} \right\}^2 , \quad (2.13)\end{aligned}$$

where M is the reduced mass of the μp atom,[8] E_ν is the uniquely determined neutrino energy and $\psi_\mu(0)$ is the wavefunction of the atom at the origin. Equation (2.13) is evaluated numerically by inserting $g_P^{\rm ChPT}$ and allowing a variation of Δg_P to highlight the sensitivity of Λ_S with respect to g_P:

$$\Lambda_S(g_P^{\rm ChPT} + \Delta g_P) = (692.3 \pm 3.4)(1 + \Delta r)(1 - 0.0108 \Delta g_P)^2 \ {\rm s}^{-1}, \quad (2.14)$$

where the first term includes the uncertainty of the form factors[9] and Δr contains radiative corrections relevant for muon capture. The central value for the non-radiative part of Λ_S in equation (2.14) is $\Lambda_S = 692.3$ s^{-1}, when evaluated without a variation in g_P ($\Delta g_P = 0$). This result is similar to other calculations by Bernard ($\Lambda_S = 687.4$ s^{-1}) [35] and Ando ($\Lambda_S = 695$ s^{-1}) [36].[10] Czarnecki performed the first complete calculation of the electroweak radiative corrections to muon capture by studying the related process of beta decay and determined the value, $\Delta r = 0.028 \pm 0.004$. Thus, the theoretical prediction for Λ_S is

$$\Lambda_S^{\rm Theory} = 711.5 \pm 3.5 \pm 3 \ {\rm s}^{-1}, \quad (2.15)$$

where the two uncertainties come from the uncertainty of the form factors and radiative corrections, respectively. The formulation in equation (2.14) has the attractive feature that the sensitivity of Λ_S with respect to g_P is analytical. Thus, an experimental extraction of

[8] $M \equiv (m_p m_\mu)/(m_p + m_\mu)$

[9] This uncertainty is dominated by the contribution from δg_A.

[10] The review by Kammel and Kubodera [11] contains a table of numerical values used for the form factors in each of these calculations.

g_P can be written in terms of a measurement of Λ_S:

$$\Lambda_S^{\text{Experiment}} = (692.3)(1+\Delta r)(1-0.0108\Delta g_P)^2 \tag{2.16}$$

$$\Lambda_S^{\text{Experiment}} = \Lambda_S^{\text{Theory}}(1-0.0108\Delta g_P)^2$$

$$\Delta g_P = 92.59\left(1-\sqrt{\frac{\Lambda_S^{\text{Experiment}}}{\Lambda_S^{\text{Theory}}}}\right) \tag{2.17}$$

$$g_P^{\text{Experiment}} = g_P^{\text{Theory}} + 92.59\left(1-\sqrt{\frac{\Lambda_S^{\text{Experiment}}}{\Lambda_S^{\text{Theory}}}}\right). \tag{2.18}$$

The experimental determination of Λ_S^{MuCap} is the focus of the remaining chapters of this thesis.

Chapter 3

Experimental Challenges and Design

The previous chapter described the calculations required to extract g_P from a measurement of the rate of muon capture on the proton in a singlet μp atom. This chapter presents some of the experimental challenges related to making that measurement at a level commensurate with the precision reached in recent theoretical calculations.

In an ideal experiment, a single muon is observed coming to rest in a pure hydrogen target, and its arrival time is recorded. Environmental conditions are chosen to ensure that the μp atom is in the singlet configuration of the ground state. Subsequently, either the decay electron in process (2.2) or neutron in process (2.5) is observed. Three major challenges must be addressed:

1. The relative spin configuration between the proton and the muon must be known.

2. The environment must be controlled to avoid capture on other materials.

3. The capture rate must be extracted from the detection of the decay electron or capture products.

The purpose of this chapter is to connect these requirements to the practical choices available in experimental design. The interaction of muons with matter and formation of atoms is described. The effects of environmental conditions on the observed disappearance rate is addressed. The principal technique used to extract the capture rate, the lifetime method, is outlined. The prescription for a successful measurement is clear, but the components required to achieve an interpretable result are complicated.

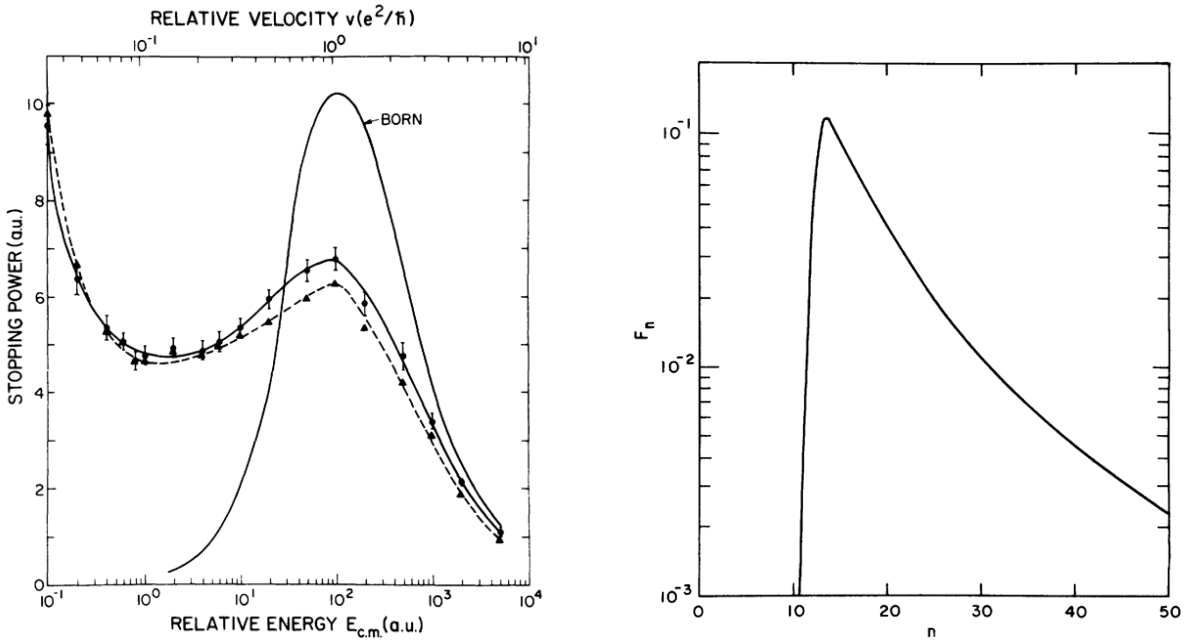

(a) (b)

Figure 3.1: Properties of muons stopping in hydrogen. (a) The average stopping power is shown as a function of energy. The relevant energy range for MuCap is $E_\mu < 5$ MeV. As muons stop, the average dE/dx increases. (b) A normalized distribution of the initial principal atomic orbital of muons captured atomically. The distribution is shown on a log scale and is highly peaked around $n = 14$. Both figures are reproduced from the calculations of Cohen [41].

3.1 Negative Muons in Materials

Experiments that measure the rate of OMC in hydrogen typically use either liquid or gaseous protium targets. The density is an important factor for many of the processes discussed here, so it is convenient to define the density, ϕ, relative to the density of liquid hydrogen $\phi_{\mathrm{LH}_2} \equiv 1$. The relevant densities for gaseous targets are in the range $0.01 \leq \phi \leq 0.1$ [37–40].

Muons entering a hydrogen target slow down via electromagnetic interactions with the gas or liquid. As the muons reach the end of their range, the energy loss (dE/dx) increases, as shown by the low energy portion of the curve in Figure 3.1a [41, 42]. The muons are then captured atomically, forming μp atoms in highly excited orbitals ($\bar{n} \sim 14$) as shown in Figure 3.1b. The muons rapidly cascade to the ground state via a combination of radiative

decay

$$(\mu p)_n \rightarrow (\mu p)_{n'} + \gamma, \tag{3.1}$$

Coulombic de-excitation

$$(\mu p)_n + p \rightarrow (\mu p)_{n'} + p, \tag{3.2}$$

and Auger emission

$$(\mu p)_n + e \rightarrow (\mu p)_{n'} + e. \tag{3.3}$$

As the muons reach the ground state, the singlet $(\mu p)_S$ and triplet $(\mu p)_T$ 1s ground state configurations are populated in a statistical manner. The triplet configuration is filled preferentially in a ratio 3 to 1 compared to the singlet configuration. The μp atoms lose energy via elastic scattering

$$(\mu p)_{T,S} \leftrightarrow (\mu p)_{T,S}, \tag{3.4}$$

and via the spin-flip reaction

$$(\mu p)_T + p \leftrightarrow (\mu p)_S + p. \tag{3.5}$$

The energy difference $\Delta E = E((\mu p)_T) - E((\mu p)_S) = +0.18$ eV drives the thermalized μp atoms into the singlet configuration, and prohibits subsequent hyperfine transitions to the triplet configuration [11]. The transition rate to the singlet state scales inversely with hydrogen density. Approximately 10 ns is required to ensure that the μp atoms reach the singlet state for experiments with density $\phi \sim 0.01$.

The hyperfine distinction is relevant because the capture rate from these states is drastically different. The capture rate for $(\mu p)_S$ is $\Lambda_S \approx 700\ s^{-1}$ while the capture rate for $(\mu p)_T$ is $\Lambda_T \approx 12\ s^{-1}$ [11].[1] This large discrepancy is a consequence of the "V-A" structure of the weak interaction - the relative chirality of the muon and the proton in the triplet

[1] This can be computed from Equation (2.7) in the same manner that Equation (2.13) was produced.

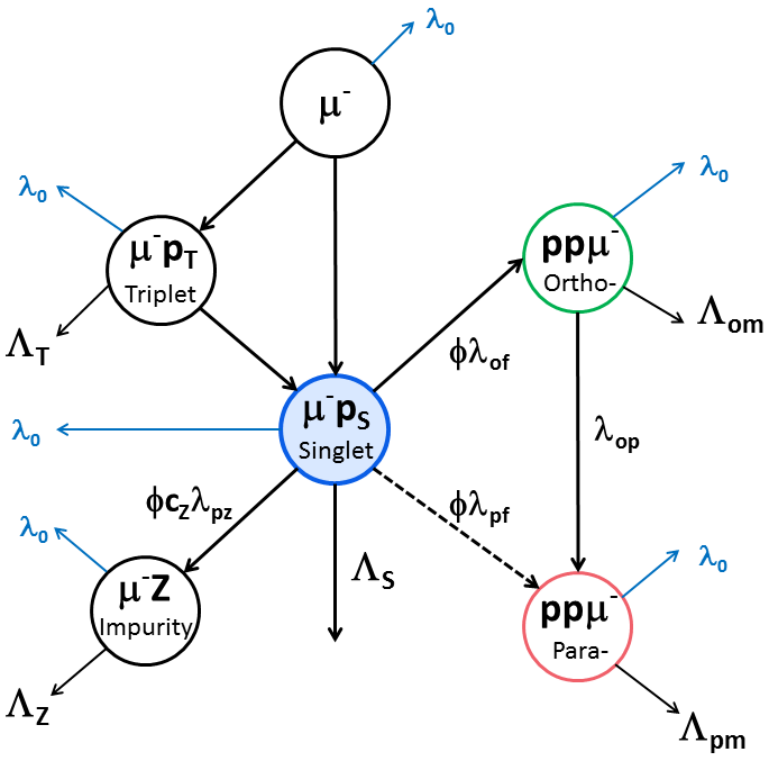

Figure 3.2: Muon kinetics diagram. The muon populates the singlet μp state within 10 ns. Molecular formation occurs at rates proportional to the density of the gas. The ortho formation rate is much higher than the para formation rate ($\lambda_{of} >> \lambda_{pf}$), but transitions from the ortho- to the para-molecular states do occur. Muons will also transfer to impurities at a rate proportional to the impurity concentration in the gas. The muon can capture from any atomic or molecular state, denoted by Λ. The muon can also decay with rate λ_0 from any state.

configuration greatly suppresses the capture process.

3.1.1 Molecular Formation

The μp atom quickly occupies the singlet hyperfine state, and the capture rate in this state is related to g_P through equation (2.18). It would be ideal if the μp atom remained in the singlet configuration until either capturing or decaying. However, several other channels are available for the μp atom, as depicted in Figure 3.2.

The μp atom interacts with other hydrogen molecules in the target, and forms muonic hydrogen molecules, $pp\mu$, at a rate $\Lambda_{pp\mu}$ via the process $\mu p + H \rightarrow pp\mu + e^-$. The forma-

tion rate scales linearly with ϕ. Because the relative spins of the particles are critical for determination of the capture rate, the molecules are categorized into two types: orthomolecular – when the proton spins are aligned – and paramolecular – when the proton spins are anti-parallel. When the muon transfers to a molecule, the formation of the orthomolecular state dominates.[2] Muon capture proceeds from the orthomolecular state with either of the available protons at an observed rate

$$\Lambda_{OM} = 2\gamma_{OM}\left(\frac{3}{4}\Lambda_S + \frac{1}{4}\Lambda_T\right), \tag{3.6}$$

where $2\gamma_{OM} = 1.009$ is a factor that takes into account the modification of the muon's wavefunction in the molecular state. Neglecting the small value of Λ_T relative to Λ_S yields $\Lambda_{OM} \approx \frac{3}{4}\Lambda_S$. From the paramolecular state, the relative spin-orientations between the muon and the available protons result in a capture rate of

$$\Lambda_{PM} = 2\gamma_{PM}\left(\frac{1}{4}\Lambda_S + \frac{3}{4}\Lambda_T\right), \tag{3.7}$$

with a paramolecular wavefunction overlap factor of $2\gamma_{PM} = 1.143$. The paramolecular rate reduces to roughly $\Lambda_{PM} \approx \frac{1}{4}\Lambda_S$. The molecular formation rate depends on the hydrogen density. As shown in Figure 3.3a, at LH_2 density, the molecular populations quickly dominate the atomic population. For $\phi = 0.01$, as shown in Figure 3.3b, the molecular formation is highly suppressed and the muon remains in a μp atom.

The muon chemistry is further complicated because the transition rate from the orthomolecular state to the paramolecular state, λ_{op}, has a large uncertainty stemming from several experiments that produced conflicting results. The two experimental results are $\lambda_{op} = 4.1 \pm 1.4 \times 10^4$ s^{-1} [37] and $\lambda_{op} = 11.1 \pm 1.9 \times 10^4$ s^{-1} [13] and a theoretical calculation yields $\lambda_{op} = 7.1 \pm 1.2 \times 10^4$ s^{-1} [43]. The discrepancy between these values is important for

[2]The kinetics diagram shows both molecular formation channels (λ_{of} and λ_{pf}) are available, but λ_{of} dominates ($\approx 250 \cdot \lambda_{pf}$) and is approximately equal to the total molecular formation rate $\lambda_{pp\mu}$.

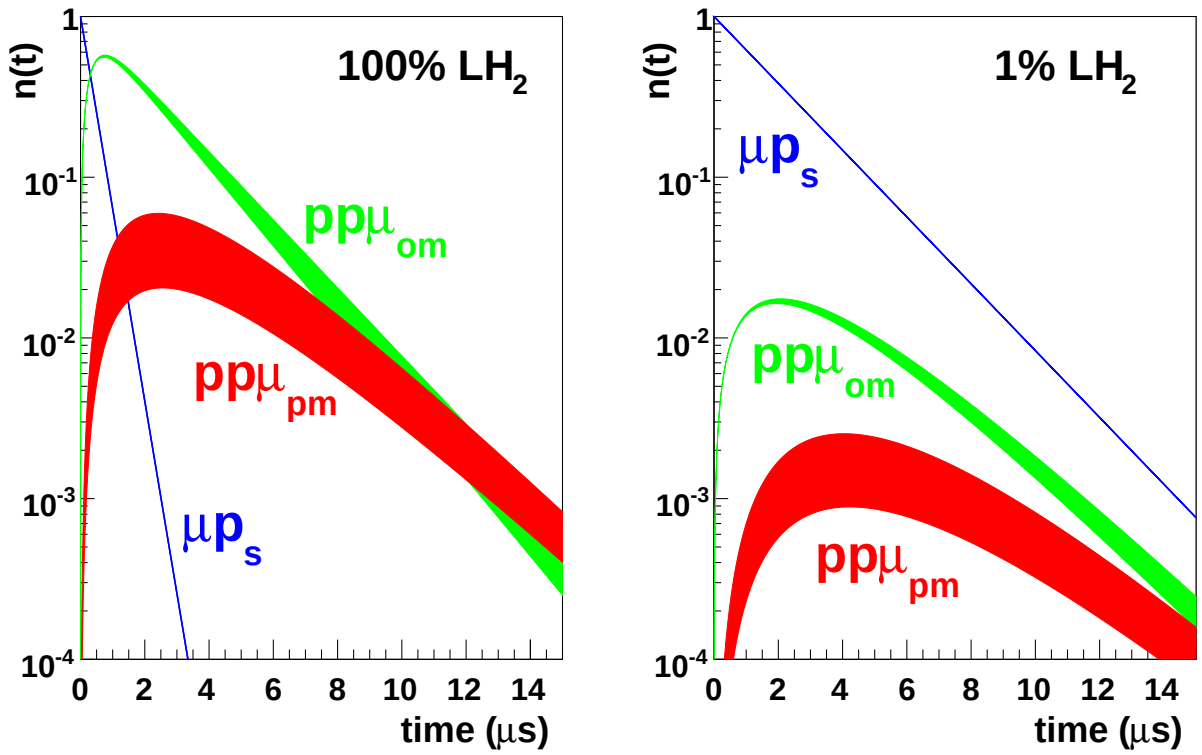

(a) (b)

Figure 3.3: Time evolution of atomic and molecular populations. The relative population of singlet μp (blue), orthomolecular $pp\mu_{om}$ (green) and paramolecular $pp\mu_{pm}$ (red) are shown for (a) 100% liquid hydrogen density and (b) 1% liquid hydrogen density. The bands indicate the uncertainties in the populations that arise from the uncertainty of λ_{of} and λ_{op}. An averaged value of $\lambda_{op} = 6.6 \pm 3.4 \times 10^4$ s^{-1} is used, which accounts for the discrepancy in the measured value of λ_{op}. In liquid hydrogen, the molecular species quickly dominate, while at low density ($\phi = 0.01$), the singlet state dominates, even at late times. This figure is reproduced from the Kammel and Kubodera precision muon capture review [11].

the interpretation of the observed disappearance rate in muon capture experiments.

Experiments that use high density hydrogen targets are more sensitive to this time-dependent population shift, which makes the interpretation of the observed disappearance rate difficult. An ideal experiment is one that quickly populates the singlet μp state and suppresses transitions to the molecular states.

3.1.2 Elemental Impurities

To ensure that the muons capture on hydrogen, it is necessary to minimize elemental impurities in the target. Typical impurities in a hydrogen target come from residual air molecules and humidity outgassing from the walls of the target, and mainly consist of oxygen and nitrogen. A μp atom is neutrally charged and has a Bohr radius that is ≈ 200 times smaller than the hydrogen atom. Consequently, the neutral μp atom can get much closer to any impurity atom it encounters. This leads to a large wavefunction overlap with the protons in the impurity atom, increasing the probability that the muon will be transferred to that atom. The effective transfer rate to an atom of nuclear charge Z is a function of the nuclear charge, the density of the gas and the concentration of the impurity: $\Lambda_{pZ} = \phi c_Z \lambda_{pZ}$, where λ_{pZ} is the transfer rate to the impurity in LH_2. For the common impurities in muon capture experiments, $\Lambda_{pN} = \phi \cdot c_N \cdot 3.4 \times 10^{10}$ s^{-1} and $\Lambda_{pO} = \phi \cdot c_O \cdot 8.5 \times 10^{10}$ s^{-1}.

The presence of impurities in the target is problematic because the process

$$\mu^- + Z \rightarrow (Z-1) + \nu_\mu. \tag{3.8}$$

distorts the observed disappearance rate. After the muon has transferred to the impurity atom, process (3.8) occurs with a rate

$$\Lambda_c(A,Z) = Z_{\text{eff}}^4 \kappa_1 \left(1 - \kappa_2 \frac{A-Z}{ZA}\right), \tag{3.9}$$

where Z_{eff} is the effective nuclear charge available to interact with the muon, and is very close to Z for light nuclei. The coefficient κ_1 is related to capture rate on hydrogen and κ_2 is related to the size of the nucleus [44].

Because muon capture on other elements scales with $\sim Z_{\text{eff}}^4$, their presence in the hydrogen target produces a distortion of the measured disappearance rate. For this reason, all elements with $Z > 1$ are classified as high-Z. The measured values for the capture rates on

the most common impurities are $\Lambda_N = 8.6 \times 10^4$ s^{-1} for nitrogen and $\Lambda_O = 15.9 \times 10^4$ s^{-1} for oxygen, compared to $\approx 0.07 \times 10^4$ s^{-1} for hydrogen [44]. The combination of an efficient transfer rate to elemental impurities coupled with the high disappearance rate from those states make elemental impurities undesirable for capture rate measurements on hydrogen.

3.1.3 Isotopic Impurities

The presence of isotopic impurities in a hydrogen target also leads to distortions in the measured disappearance rate. In the presence of deuterium, the μp atom transfers the muon to the deuteron at a rate proportional to the deuterium concentration, c_d. The transfer process

$$\mu p + d \rightarrow \mu d + p \tag{3.10}$$

is driven by the lower binding energy in the μd state, $\Delta E = 134.7$ eV [45]. The capture rate for deuterium is not the primary problem as it is not much different from Λ_S ($\Lambda_D \sim 400$ s^{-1}),[3] so a small concentration of this isotopic impurity would lead to a very small distortion to the overall rate. The reason deuterium distorts the measured rate is more subtle. When process (3.10) occurs, the μd atom is created with ≈ 45 eV of kinetic energy [45]. The cross section has a minimum because of a Ramsauer-Townsend interference around 7 eV, as shown in Figure 3.4. The μd that is initially formed with 45 eV is quickly downscattered into this energy range, where it diffuses with a large mean free path.

During an average muon's lifetime, the diffusion distance is of the scale of centimeters. Figure 3.5 shows the distribution of the diffusion distances for two deuterium concentrations in a hydrogen target. This process leads to distortions of the result in two different ways that are relevant to MuCap. First, μd diffusion is a mechanism that can transport muons from the good fiducial volume filled with hydrogen, to a boundary constructed from high-Z materials.

[3] Modeling the nucleon structure leads to some variation in the theoretical calculations for Λ_D (from 386 s^{-1} to 416 s^{-1}). Experimental measurements are in the range of 369 ± 96 s^{-1} to 470 ± 29s^{-1}. A discussion of these results is covered in the Kammel and Kubodera review [11] and references 14,48,49,70,118-121 within.

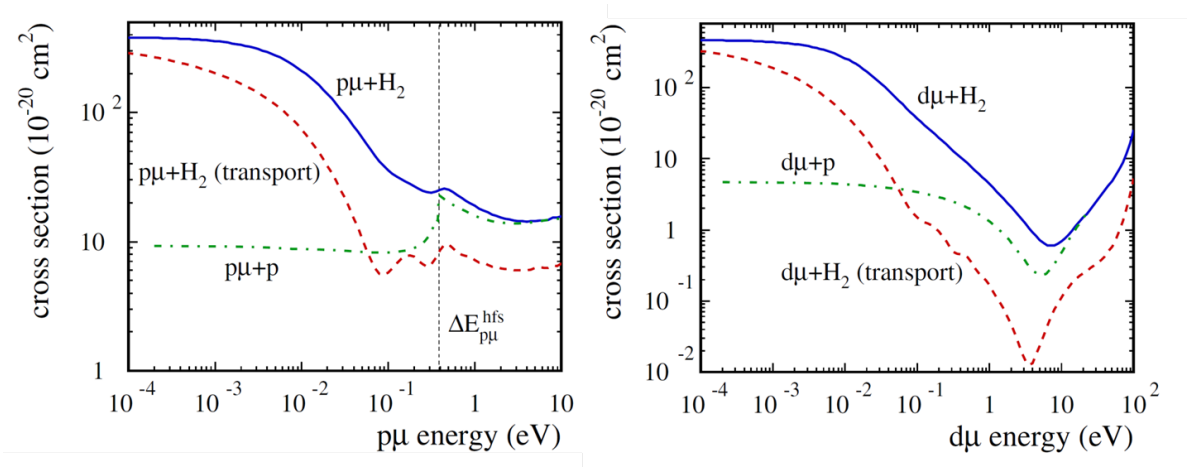

Figure 3.4: The cross sections for μp and μd in gaseous hydrogen are shown in blue. The cross-section for ≈ 45 eV μd atoms is near the Ramsauer-Townsend minimum. The diffusion scale is ~ 10 mm/μs. These figures are reproduced from Adamczak and Gronowski [45]

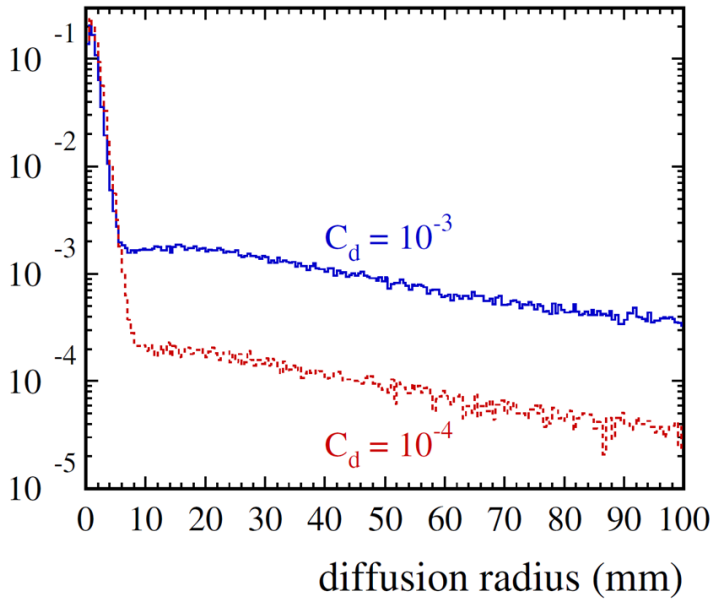

Figure 3.5: The diffusion distances for 1000 ppm and 100 ppm deuterium concentrations. The unchanged peak for < 10 mm demonstrates the μp component of diffusion, and the tails are caused by μd diffusion. These figures are reproduced from Adamczak and Gronowski [45]

The muon can then transfer to the high-Z materials and distort the observed disappearance rate, as described in Section 3.1.2. Second, in MuCap, the muon stop location is imaged in three dimensions by a TPC, which will be discussed in Section 4.5. Wire chambers are used to detect the decay electron and determine its trajectory. A pointing requirement is imposed to ensure the detected electron originates from the muon stop location. If the μd atom diffuses away from the stop location, the pointing requirement may fail. Furthermore, the mean diffusion distance is a function of time, so the fraction of events that pass this cut decreases as a function of time. The time-dependent acceptance probability manifests as a distortion in the observed disappearance rate of muons from the target, and is dangerous for a precision experiment.

3.1.4 Target Density Choice

The choice of stopping target density critically affects the interpretation of the measured result. Several factors influence the choice of target density, and past measurements have been made using gas ($\phi = 0.01 - 0.10$) as well as liquid hydrogen (LH_2) ($\phi = 1.0$) targets. Figure 3.6 summarizes the previous efforts to determine g_P and categorizes the method used in each experiment.[4]

Early experimental efforts made use of LH_2 targets that were part of bubble chambers [10, 39]. Incoming muons destabilized the superheated hydrogen along their paths and created small bubbles which were imaged. External magnetic fields were applied to allow charged particle identification. These detectors had excellent stopping power for low energy muons, which ensures that the muon stop location is far away from high-Z wall materials. However the consequence of using a LH_2 target is the increased molecular formation rate described in Section 3.1.1. The rapid formation of the orthomolecular species and the transition to the paramolecular species introduces a time-dependent effective capture rate for the

[4]The extraction of g_P from the past experiments has been updated in the recent review on precision muon capture [11] in light of the recent radiative corrections [12] and λ_{op} measurement [13]. The initial MuCap result, Andreev 07 [14] has been recalculated to include the new positive muon lifetime [8].

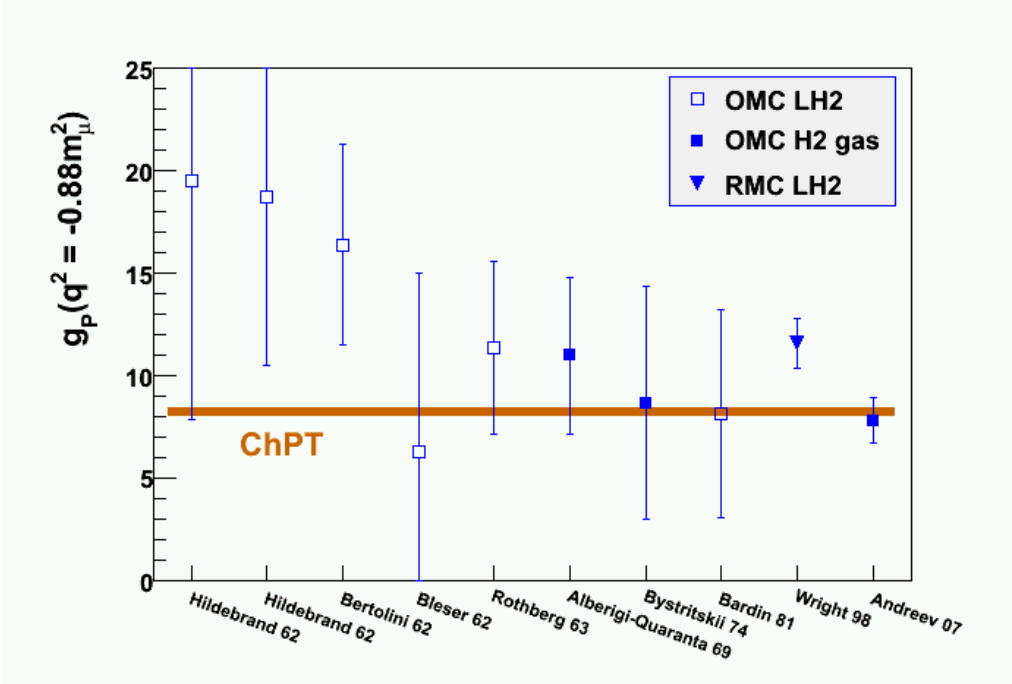

Figure 3.6: History of measurements to determine g_P. The type of target (LH_2 vs. gas) is shown, and the first MuCap result (Andreev 07) is included. The extraction of g_P from previous experiments has been updated based on improvements to theory [12] and a new measurement of λ_{op} [13]. This figure is reproduced from the recent review on precision muon capture [11].

ensemble. By suppressing the molecular formation rates, these effects can be described by small corrections to the observed disappearance rates.[5] Figure 3.7 demonstrates the relative sensitivity of the extracted value of g_P with respect to λ_{op} for the three most precise results. By using a gaseous hydrogen target with $\phi \approx 0.01$, the pseudoscalar coupling g_P can be extracted without controversy.

3.2 Positive Muons in Materials

An auxiliary μ^+ lifetime measurement is made to directly compare a measurement with the MuCap detector to the world average for τ_{μ^+}. Positively charged muons behave differently from negatively charged muons in hydrogen. The charged-particle stopping procedure is

[5] This is addressed in Section 8.3.

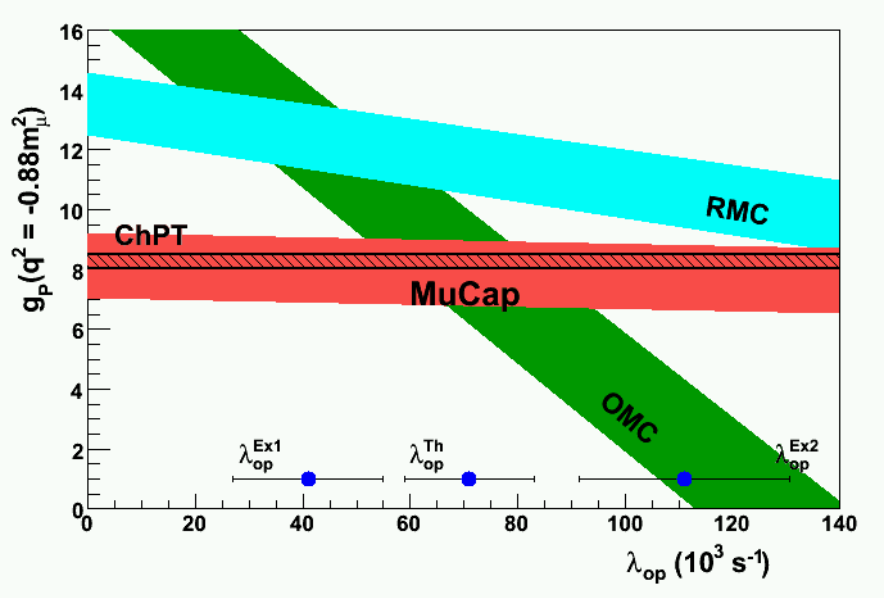

Figure 3.7: The extraction of g_P vs λ_{op}. The three most precise measurements, including the recent MuCap result, are shown as a function of λ_{op}. The choice of density in MuCap makes the result mostly insensitive to λ_{op}. This figure is reproduced from the recent review on precision muon capture [11] with the same corrections as in Figure 3.6.

similar,[6] however μ^+ are not attracted to the hydrogen atoms and are not captured atomically by the nuclei. Muonic hydrogen is not formed, and conservation of charge prohibits muon capture on the protons. The only available disappearance channel for μ^+ particles is regular muon decay.[7]

Since muon beams are generated via pion decay, the muons are usually polarized when they enter the target. The stopping process preserves some of this polarization, with the fraction depending on the internal structure of the stopping target. The result is a residual polarization of the stopped ensemble of muons, and this spin precesses in the presence of a magnetic field.

Because the muon spin precesses, it is useful to impose a known magnetic field so that the oscillation signal can be observed directly. In the absence of an imposed field, the μ^+ will rotate slowly (compared to its lifetime) in the residual background field from the

[6]There are small differences in the dE/dx curves for μ^+ and μ^- at low energies [46].

[7]Radiative muon decay ($\mu^+ \to e^+\nu_e\bar{\nu_\mu}\gamma$) and mu to 3e ($\mu^+ \to e^+\nu_e\bar{\nu_\mu}e^+e^-$) modes also exist with small branching ratios [6]

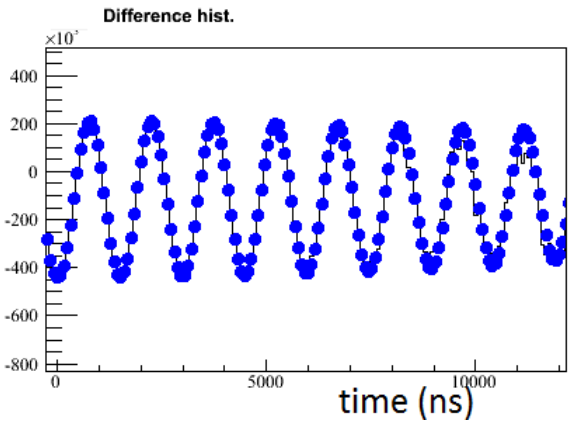

Figure 3.8: Difference between opposite detectors vs time. The oscillation signal is present in the individual detectors, and the difference between opposite detector elements is plotted to decouple the oscillation from the muon decay rate. The observed oscillation period of $\sim$ 1500 ns is generated by a 50 Gauss field.

earth and other nearby magnetic sources. A slow rotation causes problems if the detector elements have different relative efficiencies, and would manifest as a distortion of the observed disappearance rate. An example of the oscillation signal is shown in Figure 3.8 from the MuCap data analysis for a 50 G external magnetic field. The clear oscillation signal allows for decoupling of the decay rate from any slow precession effects.

The positive muon can form an atom with a free electron μ^+e^- (muonium), with the muon acting like the nucleus. The decay rate for muons in the muonium system is the same as for the free muon to the sub-ppb level due to cancellations in the various bound state effects, so this does not lead to a distortion of the observed disappearance rate, λ_{μ^+} [47]. This has been experimentally verified by MuLan at the ppm level [8].

3.3 Decay Channel

Experiments studying OMC need to detect the decay electron when the muon decays, or the neutron produced in muon capture. Some previous experiments directly detected the capture neutron, but the associated systematic uncertainties disfavor this method for the precision required in the MuCap proposal. The capture neutron has an energy of E_n =

5.2 MeV, and the absolute energy calibration of the neutron detector must be precisely determined. The muon decay and subsequent interaction with the stopping target and neutron detector produces large electron and gamma backgrounds that must be identified. The overall detection efficiency must be modeled with Monte Carlo, and these requirements make this method challenging.

The modern approach is to detect the decay electron and use the lifetime method [37]. The time difference between the muon entering the detector and the subsequent decay electron or positron is measured. The lifetime method then compares the disappearance rate for the free μ^+ and the μ^- in hydrogen, and the difference is attributed to the capture process:[8]

$$\begin{aligned} \Lambda_S &\approx \lambda_{\mu^-_{obs}} - \lambda_{\mu^+} \\ &= (\tau_{\mu^-})^{-1} - (\tau_{\mu^+})^{-1}. \end{aligned} \tag{3.11}$$

Figure 3.9 demonstrates equation (3.11) qualitatively; quantitatively the individual rates λ_{μ^+} and λ_{μ^-} must be precisely determined. To achieve a 1% uncertainty on Λ_S, it is necessary to measure each decay rate to 10 ppm.[9] This requires $\mathcal{O}(10^{10})$ muons of each polarity. It is useful to measure the disappearance rate for each polarity in the same detector system to provide a handle on systematic effects. Ultimately, the lifetime method will make use of the MuLan experiment's new benchmark for the positive muon lifetime, which has a precision of 1 ppm [8]:

$$\tau_{\mu^+} = 2196980.3 \pm 2.2 \text{ ps}. \tag{3.12}$$

The lifetime method is robust against backgrounds because the decay electrons are easy to detect with scintillators that have excellent timing resolution. The main challenges of this technique are ensuring that the muons remain in the μp atomic state and measuring the

[8]Corrections for the molecular formation and bound state effects are also required and will be explained in Section 8.3.

[9]Because of the precision of the world average for τ_{μ^+}, only a ~ 15 ppm measurement of τ_{μ^-} is required to reach the same precision. The 10 ppm number refers to the precision needed to extract the capture rate from an independent measurement of μ^+ data.

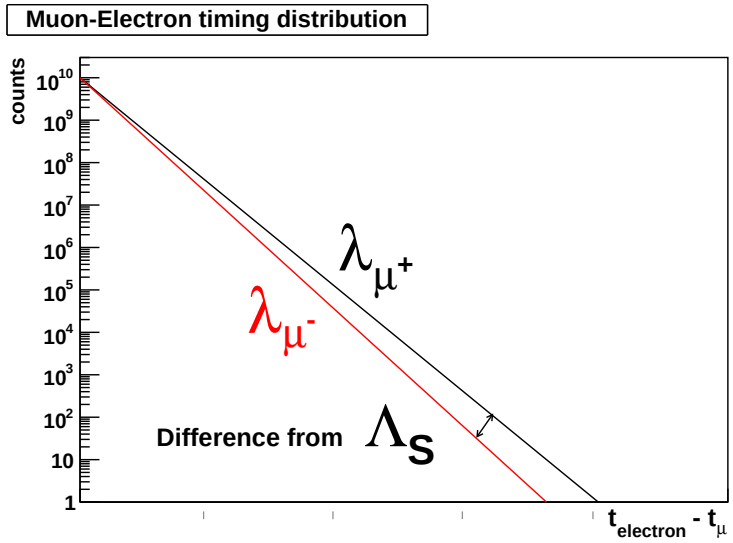

Figure 3.9: A qualitative depiction of the lifetime method. The μ^+ lifetime (black) and the μ^- lifetime in hydrogen (red) are measured, and the difference is attributed to the capture rate. The difference in this plot has been increased to demonstrate the method.

lifetime in the complex hydrogen system to the required precision.

3.4 Summary

The ideal muon capture experiment must address the potential distortions to the observed disappearance rate discussed in this chapter. The muons should be prepared in the singlet spin configuration of an atomic μp system, and environmental conditions chosen to maintain this configuration. This strongly favors employing low density gaseous hydrogen as the target. Additionally, the concentration of elemental and isotopic impurities should be minimized, since their presence distorts the observed disappearance rate. High-Z captures from materials surrounding the target must also be avoided, so the muons selected in the analysis must stop in an acceptable fiducial volume. Finally, the disappearance rate must be determined by measuring the decay or capture product. The positive muon lifetime has been precisely determined, but immense statistics are required for negative muons. The MuCap experiment is a modern effort designed to address these challenges.

Chapter 4

The MuCap Experiment

The MuCap proposal [48] was the product of detailed consideration of the challenges described in Chapter 3. The fundamental design choice is to use a gaseous hydrogen time projection chamber (TPC) as an active target. The clean interpretation of the disappearance rate for low density hydrogen gas motivates the choice of target density ($\phi = 0.011$). The active target is needed at low density to ensure that the selected muons come to rest in the gas and not in the surrounding materials.

This chapter provides a brief overview of the experimental strategy implemented by the MuCap experiment to achieve the proposed goal of determining g_P to 7% precision. Technical descriptions of the various hardware elements are provided and experimental upgrades made after the first MuCap result (run 8) are highlighted. Two production data sets were taken after the publication data and are labeled run 10 and run 11. The experimental conditions used for the final data collection period, run 11, are described in this chapter and a few comparisons to the other data sets are made.

4.1 Experimental Overview

To determine the disappearance rate of negative muons in hydrogen in the MuCap experiment, a muon must be detected entering the target, and a decay electron must be detected leaving the target. The experiment is conducted in the πE3 beamline at the Paul Scherrer Institut (PSI) in Villigen, Switzerland. A continuous low energy muon beam is transported magnetically in vacuum and delivered to the detectors. A thin plastic scintillating counter

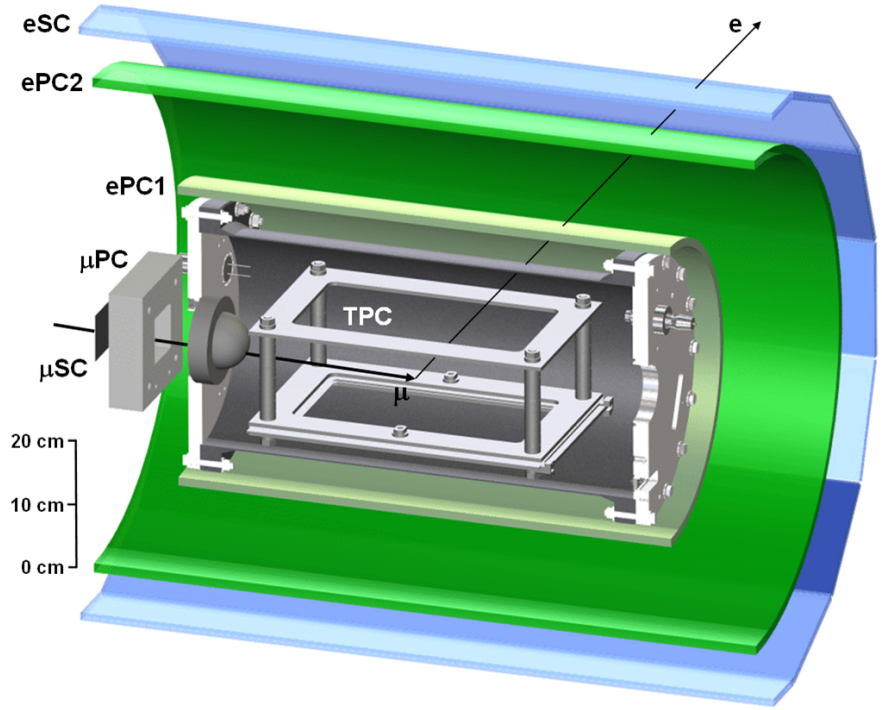

Figure 4.1: A cutaway view of the MuCap detector is shown. The beam enters from the left and encounters the μSC and μPC before entering the TPC through a beryllium window. The muon is imaged by the TPC, and predominantly decays to an electron and two undetected neutrinos. The outgoing electron track is detected by two projection wire chambers (ePC1 and ePC2) and a segmented scintillating hodoscope (eSC).

(μSC) and a small multiwire proportional chamber (μPC) record the arrival time and position of the incoming muons. The arrival time serves as the start time, t_{start} for extracting the decay time of a muon. Upon detection of a muon in the μSC, the beam is deflected by a kicker. This suppresses the possibility of additional muons entering the target during the measurement period[1] and distorting the decay spectrum. Measurement periods that contain multiple muons are discarded later in the analysis.[2] The sequence of detectors encountered by the incoming muon and an outgoing electron is depicted in Figure 4.1.

Muons enter the pressure vessel that surrounds the TPC through a thin window that minimizes the scattering of the incoming muon beam. The muons then stop in the ultra-pure

[1]The measurement period is the 25 μs immediately following the arrival of a muon in which decay electrons are observed.

[2]The presence of multiple muons during a measurement period is called pileup, and the rejection of these events in the analysis is called pileup protection.

hydrogen gas inside the TPC, which is continuously filtered to remove chemical impurities. The muons ionize electrons in the hydrogen gas, which drift to a readout plane at the bottom of the TPC. Thus, the TPC images the stopping muons and the analysis can select events that stop in the fiducial volume, away from the surrounding high-Z materials.

The dominant disappearance mode for negative muons in hydrogen is ordinary muon decay, and several detectors are positioned to observe the outgoing decay electron. Three concentric cylinders surround the pressure vessel supporting the TPC. Two layers of proportional wire chambers (ePC1 and ePC2) allow for spatial tracking of an outgoing electron. The outermost layer is a segmented scintillating detector (eSC) which determines the decay time for the muon decay spectrum. The geometry of the electron detectors results in $\approx 3\pi$ coverage of the target, with the main acceptance holes occurring along the beam direction. In the analysis, electron tracks are constructed from clusters of hits in the planes of the wire chambers. Requiring the electron track to point back towards the imaged muon stop location reduces the background from uncorrelated events. The combination of information from the muon entrance counters and the cylindrical electron detectors determines the muon decay spectrum, and the imaging TPC ensures that the selected events correspond to muons that have stopped in hydrogen.

4.2 PSI Beamline

The Paul Scherrer Institut maintains the highest intensity muon beamlines in the world, resulting in manageable length data collection periods. A series of particle accelerators is used to produce a 590 MeV proton beam that operators with milliamp-scale currents [49]. Protons are first accelerated to 0.8 MeV by an electrostatic Cockcroft Walton accelerator. The second stage consists of a 4-sector cyclotron that boosts the protons to 72 MeV. The main beam is produced by an 8-sector ring cyclotron that accelerates the protons to 590 MeV. During the accelerator maintenance period in the winter of 2007, prior to our final data

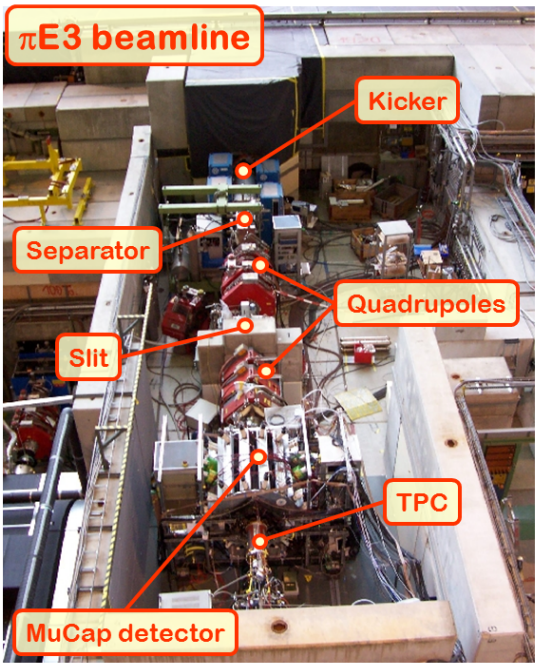

Figure 4.2: The πE3 beamline from an overhead perspective. The muon beam enters from the top of the picture and passes through the kicker and separator. Quadrupoles and slits are used together to focus the beam and make selections in position and momentum space. The muons stop in the TPC and the subsequent electron decay is measured by the surrounding detectors. In this photo, the TPC has been pulled out from the center of the electron detector for clarity. In normal operating conditions, it is inserted into the center of the MuCap detector.

collection period, upgrades were made that boosted the proton current from 1.6 mA to 2.1 mA.[3]

4.2.1 πE3 Secondary Beamline

The primary proton beam is aligned to collide with a graphite target and produces pions, muons, electrons and other backgrounds. Multiple secondary beamlines extend from the target, allowing users to produce muon beams in the energy range of 0.5 keV to 60 MeV. The MuCap experiment was set up in the πE3 secondary beamline, which is shown in Figure 4.2. In order to stop a sufficient fraction of the muons in the target gas, low energy muons

[3]The original design anticipated producing currents up to 0.2 mA in the 1970s. Accelerator engineers have done a remarkable job of tuning the system to significantly outperform the specifications. Without their achievements, the data collection phase for our experiment would be unreasonably long.

are required (4-5 MeV).

The muons used for MuCap come from the decay of "cloud" pions, which have just enough energy to leave the target before decaying weakly via $\pi^- \to \mu^- \bar{\nu}_\mu$. The chirality constraints of the weak interaction result in highly polarized muon beams. Because the π^- particles often capture on the target, the beamline is intrinsically capable of producing much higher beam rates for μ^+ than for μ^-. With the πE3 beamline elements appropriately adjusted, μ^- rates in excess of 70×10^3 muons/s were obtained. In contrast, the MuLan experiment used a similar setup in πE3 and obtained μ^+ beam rates of $\approx 10 \times 10^6$ muons/s [8].

MuCap tuned dipole elements to select a beam momentum of $\approx 32.6 \pm 1$ MeV/c , which corresponds to a kinetic energy of 5.0 MeV/c^2. Series of quadrupole fields allow for focussing and defocussing of the muon beam, akin to a lens system. Collimating slits are operated remotely and produce a focus of $\sim 2 \times 2$ cm at the muon entrance counters.

The muon beam is contaminated with electrons produced at the production target, as well as electrons produced by muons decaying in flight. The muons and electrons have a common momentum, so the electrons have a higher velocity than the muons. A separator combines a magnetic field and a compensating electric field that are tuned to produce no net deflection for the muons. The electrons in the beamline receive a smaller net impulse from the electric field than the magnetic field and are stopped by a collimator at the end of the separator. The μSC measured the ratio of beam muons to beam electrons to be 15:1 in the μ^- beam.

4.3 Kicker

The beamline contains a noteworthy element that was designed specifically for the MuLan and MuCap experiments and was constructed at TRIUMF: an electrostatic kicker [50].[4] The kicker allows users to introduce a customizable time structure to the continuous muon beam.

[4]The switching of the kicker is a dynamic process. Here, electrostatic is used to refer to the constant electric field used during a measurement period.

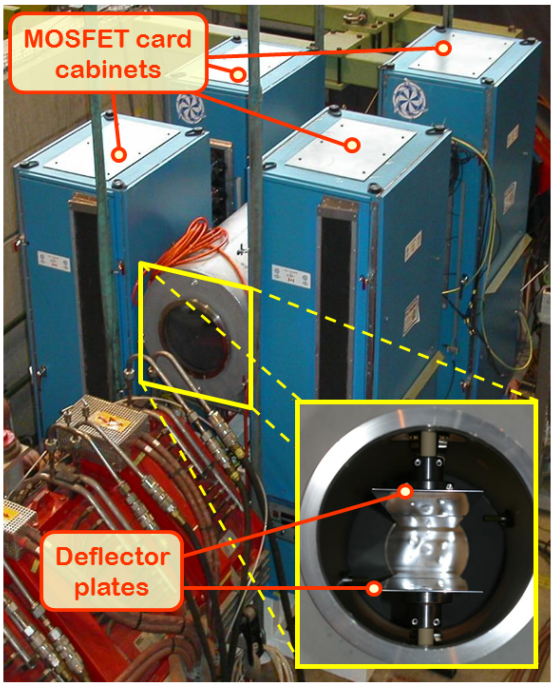

Figure 4.3: A closeup of the kicker being installed in the πE3 beamline. Four cabinets filled with MOSFET stacks provide the power for the fast-switching fields. A head-on view of the beam pipe shows the parallel deflector plates, electrically isolated from the vacuum pipe.

When the kicker is turned on, the beam is deflected into collimating slits and is prevented from reaching the experimental target. When the kicker is off, the beam is undeflected as it passes through the kicker.

Figure 4.3 shows a photograph of the kicker being installed in the beamline. Conducting deflector plates are aligned horizontally to produce a vertical electric field across the muon beam, and are shown in the cutout in the photograph. The plates are separated by 12 cm and are 1.5 m long. A potential difference of 25 kV is held across the deflector plates when the kicker is turned on. Four sets of fast-switching stacks of MOSFET cards are housed in large cabinets around the beam pipe and are capable of producing fully charged plates that remain stable within 40 ns of being turned on.[5] The underlying electronics and hardware performance were described in the thesis of MuLan graduate student David Webber [51].

[5]During part of the experiment, breakdowns in some of the MOSFET cards prevented us from running all 4 cabinets. Two cabinets were used, which increased the rise time from 40 to 60 ns, but resulted in better voltage stability.

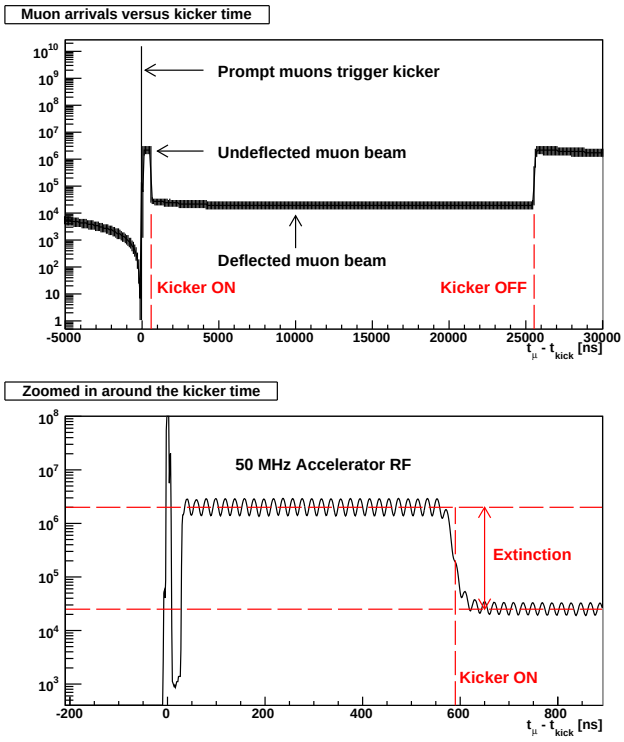

Figure 4.4: Time distribution of muons relative to the kicker signal. The upper figure shows the prompt muon peak (muons that trigger the kicker), the unsuppressed beam during the 600 ns the kicker requires to turn on, and the suppressed beam during the measurement period. The bottom panel zooms in on the first microsecond and shows the 50 MHz RF in the accelerator, and the ≈100 extinction factor between the unsuppressed and suppressed beam rates.

The MuCap experiment operates the kicker in a Muon-On-REquest (MORE) mode. In this mode, a muon is detected by the μSC and a signal is generated that turns the kicker on, deflecting the beam. The beam remains deflected for the measurement duration of 25 μs, at which point the kicker turns off, allowing the full beam rate. Although the MOSFET cards are designed to switch very quickly, they can become permanently damaged if they are switched on and off in rapid succession, so a safety buffer of 500 ns is imposed between successive transitions.

Figure 4.4 shows the arrival distribution of muons in the μSC with the kicker operating in MORE mode. The delay between detection of an incoming muon and the subsequent

deflection of the beam is about 600 ns[6], during which the experiment is exposed to the full, unkicked beam rate. When switched on, the kicker is very effective at deflecting the beam, however a small fraction of muons still make it to our experimental apparatus. The extinction factor is defined as the ratio of the unsuppressed beam rate to the suppressed beam rate in the entrance counters. MuCap operated with an average extinction of nearly 100, as shown in the lower panel of Figure 4.4.[7] Because of the beam extinction, approximately 90% of kicker cycles contain only a single muon. Since the analysis rejects measurement periods containing multiple muons, this increases the effective good data accumulation rate.

When operated in DC mode, the beam rate must be limited to $\sim 20 \times 10^3$ muons/s to optimize the acceptance rate with the pileup protection constraint. In this mode, the average waiting time for a muon is ~ 50 μs, and nearly 70% of event cycles contain multiple muons. With the beamline tuned to a muon rate of 70×10^3 muons/s in MORE mode, the average waiting time for a muon is ~ 14 μs. Thus, the implementation of the MORE mode allows for a shorter waiting time for muons to enter the system, and a higher acceptance rate once they do. Figure 4.5 shows the effective good data accumulation rate at the time when the kicker was first switched on. Table 4.1 contains a summary of the number of usable muon-electron pairs observed in the MORE mode compared to DC mode for runs 8–11. The implementation of the MORE mode was critical for meeting the goal of 10^{10} muons in a reasonable measuring time of ~ 6 months.

4.4 Muon Entrance Detectors

4.4.1 Scintillators

The muons exit the beamline through a 75 μm mylar window and encounter a series of muon detectors. A 5 mm-thick scintillating veto counter with a 40 mm-diameter hole in the

[6]The full 600 ns consists of processing time in the electronics (≈350 ns), signal speed (≈100 ns), switching time of kicker (≈40-60 ns) and time of flight of the undeflected muons (≈100 ns).

[7]The empirically observed extinction varied from run to run, and usually was in the range of 80 to 120.

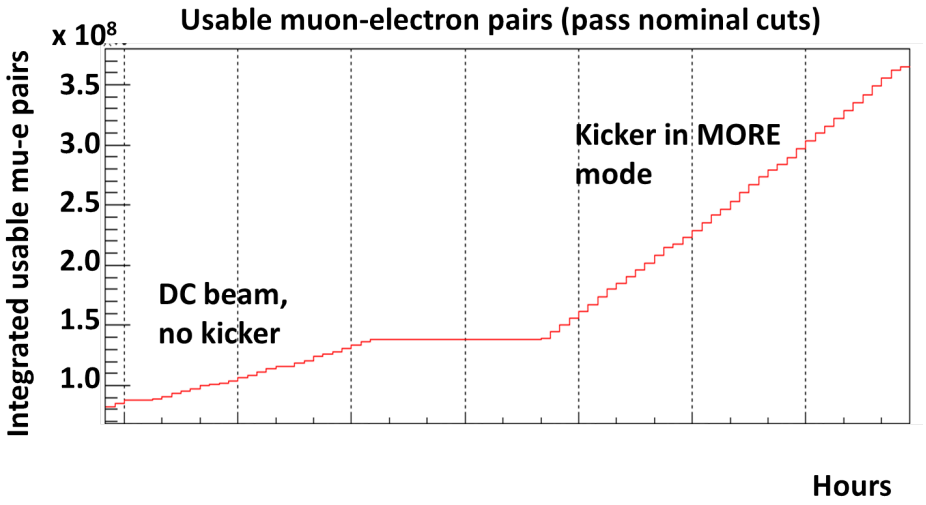

Figure 4.5: The transition from the DC data collection mode to the MORE kicker mode is shown. The effective usable data rate increases because the beam rate is increased and the fraction of events that are rejected due to pileup protection is greatly decreased.

Data set	Year Collected	Polarity	Pileup Protected $\mu - e$ pairs $[10^9]$	Beam Mode
Run 8 [14]	2004	μ^-	1.6	DC
Run 8 [14]	2004	μ^+	0.5	DC
Run 10	2006	μ^-	5.4	MORE
Run 10	2006	μ^+	1.6	MORE
Run 11 (This work)	2007	μ^-	5.0	MORE
Run 11 (This work)	2007	μ^+	4.0	MORE

Table 4.1: Summary of the data collected in different operating modes. The Muon-On-REquest mode (MORE) was implemented during run 10 and increased the effective data collection rate.

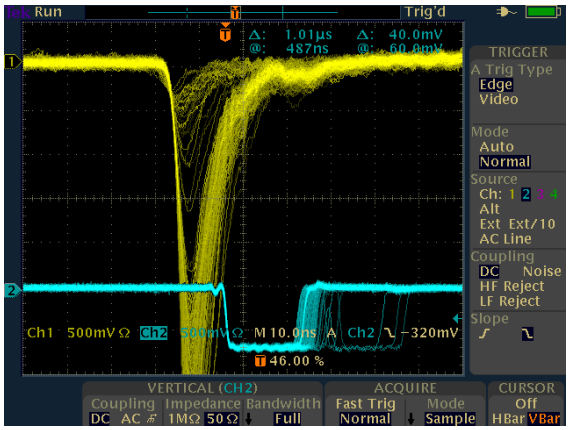

Figure 4.6: An oscilloscope trace of the entrance muon scintillator is shown in yellow, with 500 mV per division settings in persistent mode. The muons have a pulse height of approximately 3 V. A second band is formed by beam electrons is visible with $\approx$ 500 mV pulse height. The primary μSC counter threshold is set to trigger only on muons.

center is the first detector downstream of the vacuum window. The hole allows the passage of good muons along the optical axis, and the primary purpose of the veto counter is to detect divergent muons that are unlikely to stop in the TPC. The downstream side of the veto counter is lined with lead which is thick enough to stop these low energy muons. This combination collimates the muon beam and actively monitors background events that stop upstream of the target. The lead is used to increase the disappearance rate of the stray muons, as the capture rate of $\lambda_{Pb} = 12 \times 10^6$ s^{-1} is high compared to the muon decay rate [44]. The lead reduces potential decay electron backgrounds by allowing access to a high rate muon capture channel.

Directly downstream of the veto counter is the μSC: a 500 μm-thick scintillator that is used to measure the arrival time of muon candidates in the detector. The μSC is thick enough to distinguish between muons and the background electrons in the beam, as shown in Figure 4.6, but thin enough to maintain a low level of scattering and minimize divergence of the beam in the target. Pileup protection uses both the veto counter and the μSC to reject cycles with multiple muons.

4.4.2 Wire Chamber

The μPC is a multiwire proportional chamber positioned directly downstream of the μSC. The x and y coordinates of the incoming muons are determined by vertically and horizontally aligned anode wires, respectively. Each set of anodes consists of 24 wires with a 2 mm spacing and is surrounded by two cathode planes. The active area is 50×50 mm^2.

50 μm-thin mylar windows are used at the entrance and exit of the μPC to minimize the amount of scattering introduced by the counter. The μPC provides two additional planes to observe incoming muons and was used to help align the beam during beam tuning. In combination with the scintillators, the muon entrance counters observe almost all of the muons that enter our system, which allows for excellent overall pileup rejection (see Section 6.8).

4.5 TPC

At the core of the MuCap experiment lies the time projection chamber (TPC) [52]. The TPC uses the ultra-pure protium target as its operating gas.[8] The TPC is housed inside a cylindrical pressure vessel which maintains a pressure of 10 bar, which corresponds to a density of $\phi = 0.011$ with respect to liquid hydrogen. It was designed with bakeable materials in order to allow for extremely pure experimental conditions. Figure 4.7a shows the TPC detector mounted to one endcap of the pressure vessel. A saddle coil is mounted on the outside of the pressure vessel, shown in red in Figure 4.7b. When turned on, the coil produces a uniform magnetic field and is used during μ^+ data accumulation to introduce a μSR signal. During run 11, two μ^+ data subsets were accumulated with the coil operating with two different field orientations.

A 0.5 mm-thick hemispherical beryllium window is located at the entrance of the pressure vessel. The window must be thin to minimize the scattering of the incoming muon beam, but

[8] See Section 4.6.1 and 4.6.2 for the details of the gas purity.

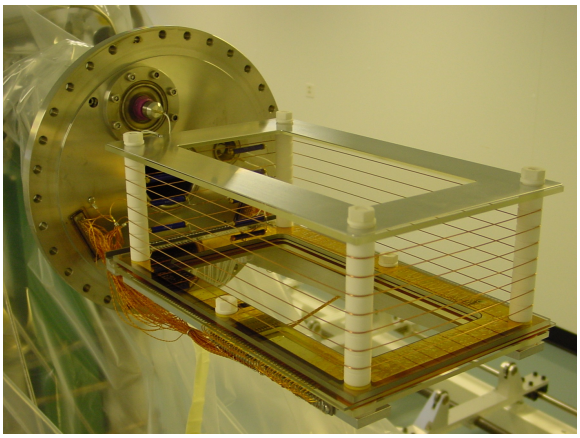

(a)

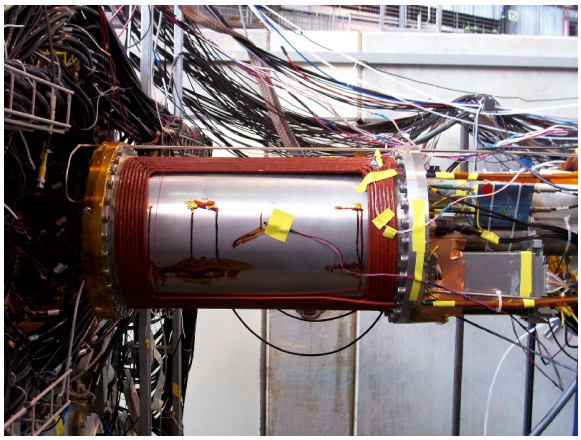

(b)

Figure 4.7: Photographs of (a) the exposed TPC mounted to one endcap of the pressure vessel. Horizontal wires wrap around four insulating pillars and generate a constant drift field. A MWPC is located at the bottom of the TPC, and the readout of these wires are fed through the endcap. (b) the TPC mounted inside of the pressure vessel (PV). Around the outside of the PV is a saddle coil used to create a uniform magnetic field for μSR precession for the μ^+ measurement.

must be thick enough to safely hold the hydrogen gas. As incoming muons enter the TPC, electrons are ionized from the hydrogen gas. The electrons then drift to a readout plane where the TPC records the signals, which allows for the determination of a muon's stopping location. The TPC consists of two sections: a drift region and a multiwire proportional chamber (MWPC). The drift region is defined by a cathode plane at the top and the upper cathode wires of the MWPC at the bottom. The active area of the MWPC is 150×280 mm^2, and the height of the drift region is 120 mm. The upper cathode plane is held at -29.1 kV and the upper surface of the MWPC is held at -5.1 kV during operation. These potentials produce an electric field of 2 kV/cm in the drift region, and the electrons drift towards the bottom of the TPC with a speed of ≈ 0.55 cm/μs .

When the ionization electrons reach the bottom of the drift region they are accelerated by the local electric field in the MWPC, generated by two outer cathode planes at -5.1 kV and a plane of anode wires that are grounded. The cathode frames contain 35 wires that are oriented in the z direction, allowing determination of the x-coordinate along the parti-

cle's track. The cathode wires are 50 μm in diameter and adjacent wires are separated by 4 mm. The anode wires are constructed from gold-plated tungsten and have a diameter of 25 μm. They are spaced 4 mm apart and are oriented parallel to the x-axis, which allows determination of the z-coordinate.

The MWPC explicitly provides spatial information in the transverse (x) and longitudinal (z) directions. The vertical spatial dimension (y) is coupled to the drift time required for the charge to reach the readout planes. The vertical coordinates of the muon track can be extracted by using external knowledge of the arrival time of the muon and relating the time delay in the arrival of the charge at the readout plane to the drift velocity. The entanglement of the vertical spatial coordinate with the time coordinate is a fundamental complexity of the TPC that requires significant attention in the analysis.

4.6 Target Gas

MuCap requires a hydrogen target gas that is both isotopically and chemically pure. The presence of deuterium in pure hydrogen can lead to distortions in the observed disappearance rate of muons due to the Ramsauer-Townsend diffusion minimum described in Chapter 3.1.3. This diffusion process leads to time dependent losses from the fiducial volume so the deuterium concentration must be suppressed. The presence of high-Z impurities provides an additional disappearance channel for the muons and leads to an increase in the observed value of λ_{μ^-}, as described in Section 3.1.2. Because the μp atoms rapidly transfer to impurity atoms and capture at higher rates, concentrations of high-Z impurities must be suppressed and measured.

To meet these requirements, hydrogen is produced via electrolysis of deuterium-depleted water, and subsequently processed by a cryogenic distillation column to further improve the isotopic purity. A continuous circulation system is employed to maintain the gas purity during operation. The PNPI collaborators developed novel hardware solutions to produce

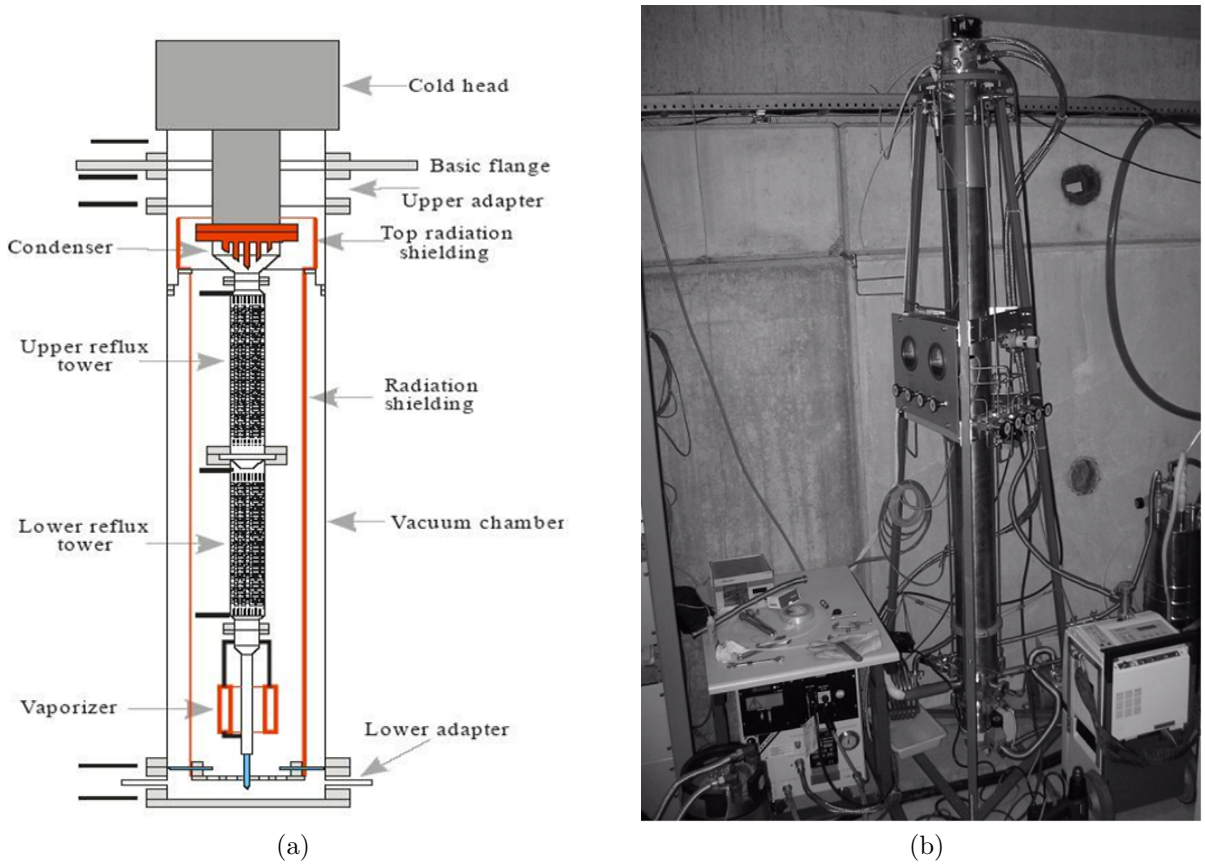

(a) (b)

Figure 4.8: The Deuterium Removal Unit (DRU). (a) A schematic view of the DRU contains the principal elements. The distillation column separates the deuterium from the protium via a condenser and reboiler cycle, reducing the deuterium concentration in the production target. (b) A picture of the DRU.

and maintain the world's cleanest protium gas.

4.6.1 Deuterium Removal Unit

The need for a systematic correction for μd diffusion can be avoided by reducing the deuterium concentration to < 10 ppb. The PNPI collaborators designed a cryogenic distillation column called the Deuterium Removal Unit (DRU) to separate the isotopic species in the target gas [53].

Figure 4.8a shows the schematic for the DRU. A cold-head liquefies the gas which collects at the bottom of the column. The liquid is reboiled, and the different vapor pressures of the

isotopes causes the deuterium to remain in the liquid. The pure protium gas is siphoned off for use as the target gas, and the enhanced deuterium liquid "waste" is collected. This cycle was run several times, and the deuterium enhanced samples were measured with gas chromatography in order to determine the separation efficiency. Based on the concentration of the deuterium extracted in the samples, it was determined that the remaining protium contained less that 10 ppb deuterium.

Throughout the run, gas samples were periodically extracted from ports in the gas system and sent to the ETH laboratory in Zurich for external analysis. A tandem accelerator mass spectroscopy (AMS) method was implemented to separate the components of the samples by atomic mass [54]. A series of measurements revealed undetectable levels of deuterium in the target gas. The sensitivity of the ETH accelerator set an upper limit of 6 ppb of deuterium. There is no systematic distortion stemming from the presence of ppb-level deuterium in our system.

4.6.2 CHUPS

The hydrogen gas is initially filled into the TPC via a palladium filter, which efficiently traps atoms that are larger than hydrogen. This prevents most high-Z impurities from entering the TPC. However, outgassing of elemental impurities from the materials and surfaces inside the pressure vessel occurs during the weeks of data collection, and those impurities need to be removed. The Circulating Hydrogen Ultra-high Purification System (CHUPS) was developed to continuously remove impurities from the TPC target gas [55]. An automated control panel manages a series of mass flow controllers that are connected in series with the TPC pressure vessel, as shown in Figure 4.9. The TPC is a sensitive device that operates with high voltage and caution was taken to ensure stable circulation conditions. Mechanical safety valves are included in the circuit to prevent unsafe overpressure. Buffer volumes are also included between CHUPS and the TPC to allow the mass flow controllers to stabilize the pressure in the TPC.

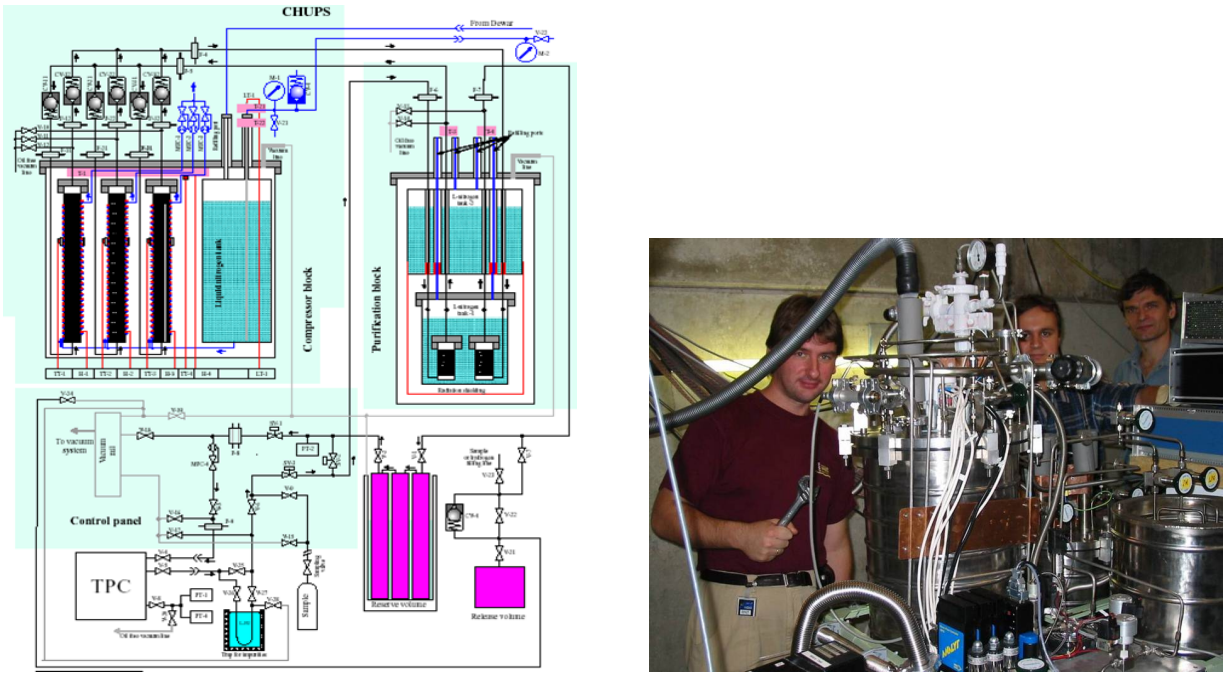

(a) (b)

Figure 4.9: (a) The left panel contains a schematic view of the Circulating Hydrogen Ultra-high Purification System (CHUPS), featuring a control panel, compressor block, purification block and the TPC. (b) The physical realization of CHUPS with the 3 PNPI scientists that built it.

The technical core of CHUPS is an adsorption cryopump system that alternatively heats and cools activated carbon to pump the hydrogen through the circulation system. The hydrogen is also passed through a purifier that utilizes Zeolite filters. The purifier operates at liquid nitrogen temperatures and traps the high-boiling elemental contaminants. The purified hydrogen is heated to room temperature and returned to the TPC.

A series of gas chromatography measurements determined the nitrogen concentration was less than 20 ppb. An in-situ humidity monitor measured 15 ppb. These external measurements of gas samples will be verified by direct monitoring of muon capture reactions on impurity atoms by the TPC in systematic studies. These impurity levels are improvements on the conditions used for the previous MuCap publication, which contained $\sim$ 50 ppb of high-Z impurities. The suppression of deuterium, nitrogen and water to $\sim$ 10 ppb is an excellent hardware achievement that reduces the uncertainty associated with making a large

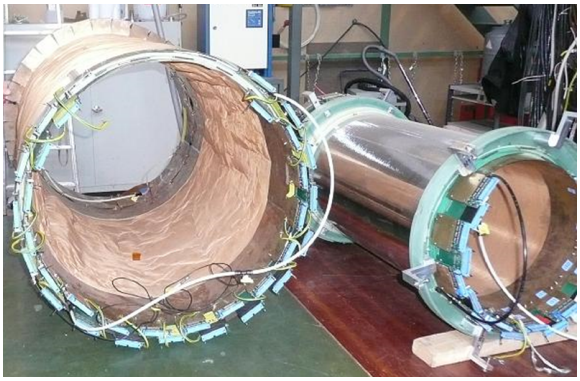

(a)

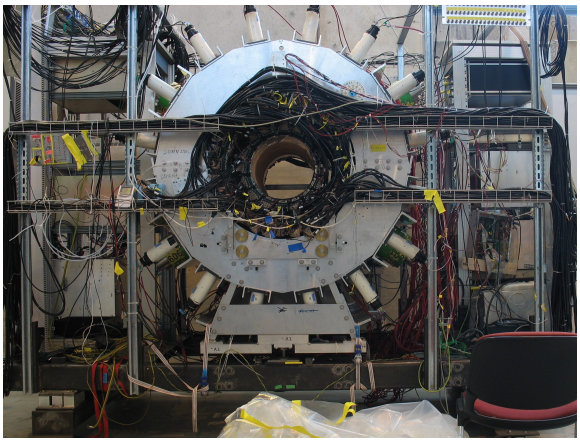

(b)

Figure 4.10: Photographs of the detector elements (a) ePC1 and ePC2 disassembled in a test lab. In measurement position, ePC1 is nested inside of ePC2. (b) ePC1 and ePC2 positioned inside the eSC. A donut-shaped metal ring holds the eSC elements in place. White plastic cylinders used to mount the eSC photomultiplier tubes (PMTs) are visible protruding radially. The system is on rails and nests around the TPC in the measurement position.

correction for the presence of impurities in the analysis.

4.7 Electron Detectors

Two cylindrical wire chambers and a segmented scintillator are positioned around the TPC pressure vessel. The electrons from muon decay travel outward from the TPC and are detected by all three devices, allowing the analysis to reconstruct tracks. The ensemble has a coverage of approximately 3π for events originating in the TPC.

4.7.1 Electron Wire Chambers

Figure 4.10a shows the two electron proportional chambers (ePC1 and ePC2) in a test lab setting. Each chamber is outfitted with readout electronics and assembled into the electron detector apparatus, shown in Figure 4.10b.

The inner electron projection chamber (ePC1) has a radius of 192 mm and length of

690 mm and fits snugly around the pressure vessel of the TPC. There are 512 anode wires with ≈ 2 mm spacing, and 192 cathode strips in each of the two cathode planes. The outer chamber (ePC2) has a radius of 320 mm and length of 910 mm. There are 1024 anode wires with a similar ≈ 2 mm spacing, and 320 cathode strips in each of the two cathode planes.

Each wire chamber consists of three planes that are read out: one anode plane and two cathode planes. The anode wires are oriented parallel to the beam axis and are lines of constant ϕ. The two sets of cathode strips follow left-handed and right-handed helical trajectories. A coincidence between the anode and a cathode results in a unique position on the surface of the chamber. A three-fold coincidence using both cathode planes can be constructed to reduce backgrounds. The temporal resolution of the wire chambers is coarse compared to the timing requirements for the lifetime measurement, so these chambers are used primarily to determine the direction of the decay electron.

ePC1 was operated with a nominal high voltage of 2640 V and was extremely stable. The nominal high voltage for ePC2 was set to 2790 V. However, ePC2 began to develop hot spots – regions that draw larger currents – and the voltage was reduced to 2740 V to avoid causing irreversible damage to the detector. There was a malfunction of one of the anode wires that required disconnecting several anode readout cards from high voltage in that region. A total of three sets of 16 anodes were removed from high voltage so that ePC2 could be operated safely and stably. This produced a blind region in ePC2 and reduced the overall coverage of the wire chambers by a few percent.

4.7.2 Electron Scintillators

To achieve a precision measurement of the disappearance rate, a precise electron decay time must be measured. A scintillating hodoscope (eSC) was installed around the ePCs to measure the electron time. The eSC consists of 16 segments in ϕ that extend over the length of the wire chambers (900 mm). Each eSC element consists of two, 5 mm planes of scintillators, and each plane has an upstream and downstream photomultiplier tube (PMT)

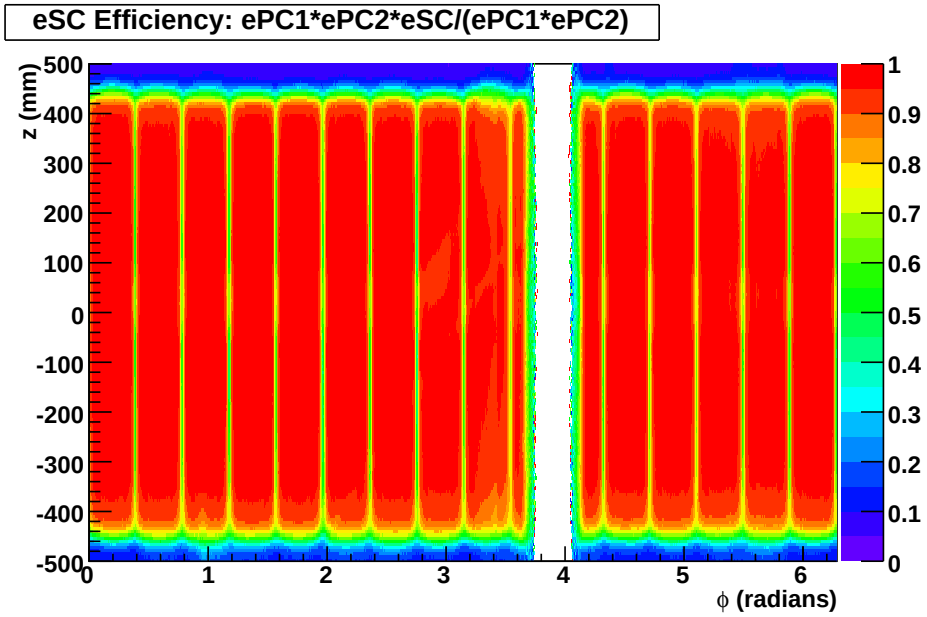

Figure 4.11: The eSC efficiency is determined by dividing the 3-fold coincidence of eSC & ePC1 & ePC2 by the 2-fold coincidence of the two wire chambers. The blind region of ePC2 accounts for the inefficient region around $\phi = 4$.

allowing for the formation of background reducing coincidences. The eSC hits have a precise timing resolution of 1.25 ns and this information is combined with the tracking information from the ePCs to fully describe the decay electron. Figure 4.11 shows the eSC efficiency by taking the ratio of the 3-fold coincidence (eSC & ePC1 & ePC2) and dividing by the wire chamber coincidence. The blind region around $\phi = 4$ is an artifact of the missing anode wires in ePC2.

4.8 Neutron Detectors

Eight liquid scintillating neutron calorimeters are positioned along the outer surface of some of the eSC segments for the purpose of studying systematics. The solid angle coverage is approximately 1%. The data from the neutron detectors is used to make an auxiliary measurement of the molecular formation rate $\Lambda_{pp\mu}$, in order to constrain the systematic uncertainty for the Λ_S measurement. Some systematic studies are made by doping the

hydrogen with Argon and the time distribution of the capture neutrons is studied directly with these detectors. The study of the capture neutrons and extraction of $\Lambda_{pp\mu}$ is the primary focus of the thesis work of fellow Illinois graduate student, Sara Knaack.

4.9 Electronics

The μSC and muon veto scintillator, μPC and the eSC are all read out with time to digital converters (TDCs) made by CAEN. The ePC detectors are read out with a customized set of TDCs (COMP) and a second copy of the eSC signals are read out by this system to verify the timing stability of the CAENs. Waveform digitizers (WFD) were also developed to read out the eSC and are used as a cross-check on the CAEN TDC timing. The WFDs are now being used as the primary electron timing device for the follow up experiment, MuSun [56]. The MWPC region of the TPC is read out with customized, self-triggering TDCs for the primary analysis. The TPC signals are also split for processing with newly developed flash analog-to-digital converters (FADC). The neutron counters are read out with these FADCs. The WFD and FADC upgrades serve as a cross-check of the timing stability of the principle electronics and provide the foundation for the electronics readout of the MuSun experiment.

4.10 Data Collection

The raw data from the various electronics components is streamed into the Maximum Integration Data Acquisition System (MIDAS) [57], which collects the information from the electronics systems. Figure 4.12 shows the flow of the data through the data acquisition system (DAQ). Frontend software programs are used by each set of the electronics systems to communicate with MIDAS, and this framework assembles all of the data streams into a single data file on the backend PC. During this assembly, MIDAS allows the users to run an analyzer module on the incoming data in order to make online diagnostic plots. Only a

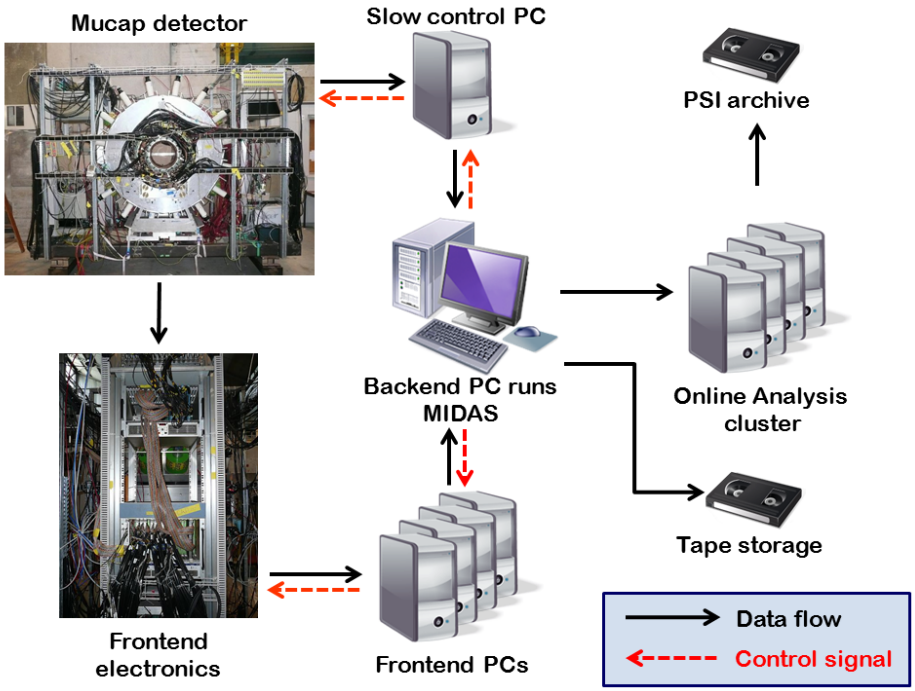

Figure 4.12: The data is generated in the detector and flows through frontend computers to the MIDAS data acquisition system running on the backend computers. A fraction of the data is processed by online analysis machines for diagnostic purposes and the raw data is stored to tape and backed up at the PSI archive.

small fraction of the data is processed in this manner, but the online analysis is a critical component in monitoring the quality of incoming data and ensuring successful data collection. Each data file is about 1.6 GB large, corresponds to 2-3 minutes of data collection and is labeled chronologically with a five digit run number. During the course of run 10 and run 11, approximately 35,000 runs were collected, corresponding to about 50 TB of raw data. Each run is copied to an LTO2 magnetic tape for transporting the data to the analysis center at Illinois, and a backup is copied to the PSI archival system. At the conclusion of the running period, the LTO2 tapes are shipped to the National Center for Supercomputing Applications (NCSA) at the University of Illinois Urbana-Champaign, and transferred to their mass storage system (MSS) archive. The data analysis procedure is detailed in Chapter 5.

4.11 Summary

The data used for the run 10 and run 11 analyses were collected in the spring of 2006 and the fall of 2007 at PSI. Each beamline allocation period lasted approximately 10 weeks and consisted of several phases. The experimental apparatus was installed in the πE3 beamline and signal cables were connected between the experimental apparatus and the data counting room. A climate controlled tent was installed around the setup to ensure constant operating temperature and humidity for the detectors and electronics, improving their overall stability and reliability. The high voltage on the TPC was ramped up over several days as a safety precaution. This patient approach conditioned the HV systems conservatively to increase their reliability. Precision adjustments were made to the beam tune to optimize the beam rates and position. Simultaneously, CHUPS cycled the hydrogen to reduce the residual elemental contamination in the system. Upon achieving stability in the multiple systems, data collection proceeded.

The run 10 data set yielded approximately 5×10^9 good muon-electron pairs. A smaller systematic measurement of μ^+ data was also collected. Systematic measurements with nitrogen-doped gas were also performed. The final production data run 11 accumulated another 5×10^9 good muon-electron pairs and a comparable μ^+ data set was collected. During run 11, systematics studies were were performed with water- and argon-doped hydrogen in order to reduce the uncertainty in the final result associated with the systematics of impurities and the molecular formation rate.

The main scope of the last four chapters of this thesis is two-fold:

i. Methods and algorithms are developed to analyze the high-statistics MuCap data set with ultimate systematic precision.

ii. These methods are applied to the main analysis of run 11. Run 10 and several auxiliary analyses for run 11 are performed by other members of the MuCap collaboration.

Chapter 5

Data Analysis

The primary function of the analysis software is to determine the muon disappearance rate in our target. Muons and electrons are each identified separately from the signals generated by the detectors, and then combined into a muon-electron pair. The muon decay time is histogrammed and the decay spectrum is fit.

5.1 Analysis Software

The MuCap analysis software is a multi-staged procedure that first converts the raw data into data structures[1] that represent particles, and then combines those particles to investigate the effects of various cuts on the decay spectrum. Figure 5.1 shows a schematic representation of the analysis procedure. After the data collection is complete, the $\sim$ 35000 data files (runs) are classified based on several parameters to select runs of good quality for the analysis. The chosen run files are sorted into run groups based on the high-voltage (HV) settings of the main detector systems during data collection, because the HV setting is related to the gain of the detector.[2]

To initialize the first stage of the analysis, the relevant data files are copied from the tape archive to a staging disk, and the analysis job is farmed out to an analysis node on the NCSA computing cluster. At this stage, the raw data ($\sim$ 1.6 GB/file) is converted into two output files. One file ($\sim$ 0.04 GB/file) contains diagnostic plots of the detector

[1] C^{++} objects.

[2] The gain is the factor between the intrinsic signal generated by a physics process and the signal that is read out by the electronics. The gain is one parameter that characterizes the detector response.

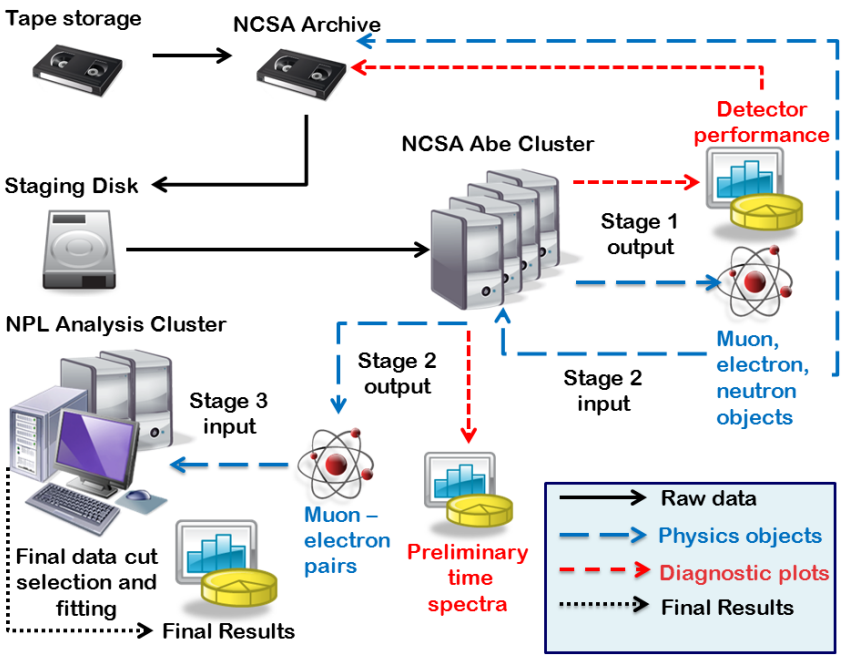

Figure 5.1: A schematic representation of the multi-staged analysis in the MuCap experiment. Solid lines (black) show the flow of raw data from the storage tapes to the analysis cluster on NCSA, small dashed lines depict the creation of diagnostic plots (red) and the large dashed lines show the reorganization of the data into "physics objects" (blue). The final data cut selection and histogram fitting is performed on the NPL analysis cluster.

system, such as raw hit distributions and hit rates. The second file ($\sim$ 1.9 GB/file) contains a tree filled with data structures corresponding to the particles observed in the detectors (i.e. muons, electrons and neutrons). Position, time and other basic properties of each particle are identified and recorded. This stage requires about 3-4 weeks to process all runs on NCSA[3] and the derived data files are stored on the NCSA archive for future processing to avoid repeating this computationally expensive step.

The second stage of the analysis uses the tree of particles as the input and constructs muon-electron pairs. Additional diagnostic plots are formed ($\sim$ 0.06 GB/file) and the muon-electron pairs are stored in a tree ($\sim$ 0.15 GB/file). Each entry in this tree contains the main properties of a single muon from the time it enters the entrance counters through the time its decay electron leaves the detector. The second stage of the analysis requires about one week

[3]This includes data transfer, job queuing, CPU time, post-processing and archiving as well as competition with other NCSA users.

to process on NCSA. This allows for the study of various properties of the muon-electron pairs based on multiple passes over the stage-one trees.

Several studies are performed on the muon-electron pair tree to test the stability of the observed disappearance rate with respect to parameters such as stop position, decay angle and distance of closest approach between the electron track and the muon stop. The third (final) stage only requires a few hours to process because the particle reconstruction procedure and coincidence finding loops are performed in the first two stages. Histograms are formed containing the muon decay spectrum, and the data are fit on the NPL computing cluster.

5.2 Blinding

The MuCap experiment uses a double-blind analysis technique. Blinding techniques protect the integrity of the experimental result by preventing accidental bias in analysis choices [58]. In an unblinded environment, honest experimentalists may subconsciously use agreement with a previous experiment as evidence that their analysis is complete.[4] The blinding procedure charges the analyzers with the task of producing an internally consistent result, regardless of how it fits in the landscape of previous measurements. Only when the collaboration is satisfied that all outstanding systematic issues have been properly addressed does the collaboration agree to unblind the data and examine the result in a physically meaningful space.

During the MuCap data collection, the master clock frequency was set in the range $498.5 \leq f_{\mathrm{run11}} \leq 499.5$ MHz, and recorded by two members of the collaboration that are not directly involved in the data analysis. The analysis assumes that the clock frequency is precisely 500 MHz, so the time metric becomes artificially compressed. In addition to the

[4]For a discussion of potential causes of "experimenter's bias" and standard solutions, I highly recommend the Klein and Roodman review [58]. MuCap uses the "hidden offset method" discussed in section 3.2.2 within that reference.

hardware blinding of the clock frequency, an additional additive offset is imposed when the analyzers report fit results to the collaboration. This prevents the clock frequency managers from using the knowledge of the clock offset to decode the analysis results. The final fitting procedure involves refitting the data with the analysis offset removed and modifying the time metric by the ratio of the true clock frequency to the assumed frequency: $r_{\text{blinding}} = f_{\text{run11}}/(500\text{ MHz})$. Throughout this document, results are presented with both offsets still imposed, as parallel analyses to determine systematic corrections are ongoing.

5.3 Muon Stop Definition

The most critical component of the analysis is the creation of a robust muon stop definition that ensures that a selected muon stops in the hydrogen gas target. The muon stop definition must include an arrival time, and a three dimensional stop location (x, y, z) within the TPC to allow for fiducial volume cuts. The muon stop definition pairs the information from the kicker, the muon entrance counters (μSC and μPC) and the TPC to fully describe the properties of muons that stop in the target.

5.3.1 Entrance Time

The raw hit times in the μSC counter and the μPC counters are examined to determine the muon arrival time (t_μ). The measurement period is defined as the 25 μs time interval immediately following a muon arrival. During the measurement period, only one muon is allowed; if an additional muon is detected, both muons are rejected. Muon entrance times are determined by the following procedure:

μSC time. When a muon is detected in the μSC, no other hits in that detector are accepted for 29 ns (software deadtime). This prevents an afterpulse generated by one muon from creating multiple entries in the data stream. Figure 5.2 shows a temporal auto-correlation plot for the raw μSC signal (black) and the processed signal (blue) after the

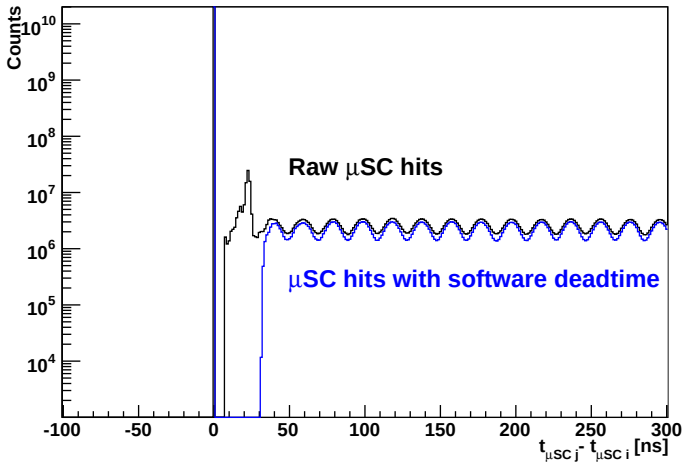

Figure 5.2: A temporal autocorrelation plot for the raw μSC hits is shown before (black) and after (blue) a software deadtime window of 29 ns is imposed. The afterpulses that are present at early times are removed, and the cleaned curve is used for the formation of coincidences and pileup protection.

signal-cleaning window is imposed.

μPC clustering. When a muon passes through the μPC, energy is typically deposited on several adjacent wires in each plane, producing multiple hits. A software deadtime of 650 ns is applied to each wire separately to remove afterpulses. The analysis combines hits that are temporally and spatially coincident into clusters for each wire plane separately. A temporal coincidence window of $\pm$230 ns is used. Hits are spatially coincident if they occur on adjacent wires, or if there is one wire separating them. If a gap of two wires exists, two distinct clusters are formed and processed individually. The earliest hit in a cluster determines the cluster time, and the average position of the participating wires determines the cluster position. The final step pairs the μPC-x and μPC-y clusters. A temporal coincidence window of $\pm$190 ns is used to form μPC-xy hits. The distribution of these hits describes the profile of the incoming muon beam, and is shown in Figure 5.3.

Muon Entrance Counter Coincidence and Pileup. The μPC-xy hits are then combined with the μSC hits, using a temporal coincidence window of $\pm$130 ns. Wire chambers have poorer intrinsic time resolutions than scintillators, so the μSC time is used for candi-

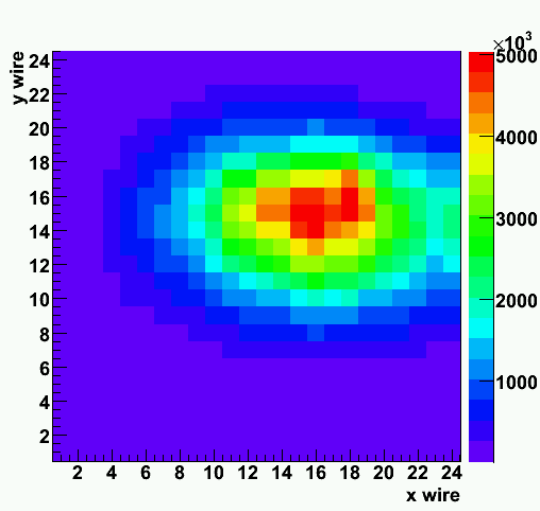

Figure 5.3: μPC-xy clusters. The clusters produce a profile of the incoming muon beam spot. Hit clusters are found in the x- and y-planes separately and then joined temporally.

date muon entrances ($t_\mu \equiv t_{\mu\text{SC}}$). A time-ordered array of the muon arrivals is stored for further processing.

A second array of times is constructed from the hit times in the entrance counters, which is used to enforce pileup protection. The pileup array contains the logical OR of the μSC, muon-veto counter, μPC-x clusters and μPC-y clusters. A muon entrance candidate is not permitted to have any additional hits on any of the counters in the pileup array within a pileup protection window of ± 25 μs. This ensures that the analysis only examines measurement periods with one muon in the TPC.[5]

Kicker coincidence. A copy of the signal that triggers the kicker is recorded in the DAQ. Muons are required to be temporally coincident with the kicker signal. To ensure that all candidate muons have the same background structure, only the muons that are responsible for triggering the kicker are accepted as candidates. In the extremely rare case that a muon enters the μSC out of time with the kicker signal and survives the pileup protection cuts, the kicker coincidence requirement discards the event. The full μSC-kicker

[5]The combined entrance counter inefficiency was measured to be $\approx 10^{-5}$, so the pileup protection is not perfect. This will be discussed in the Section 6.8.

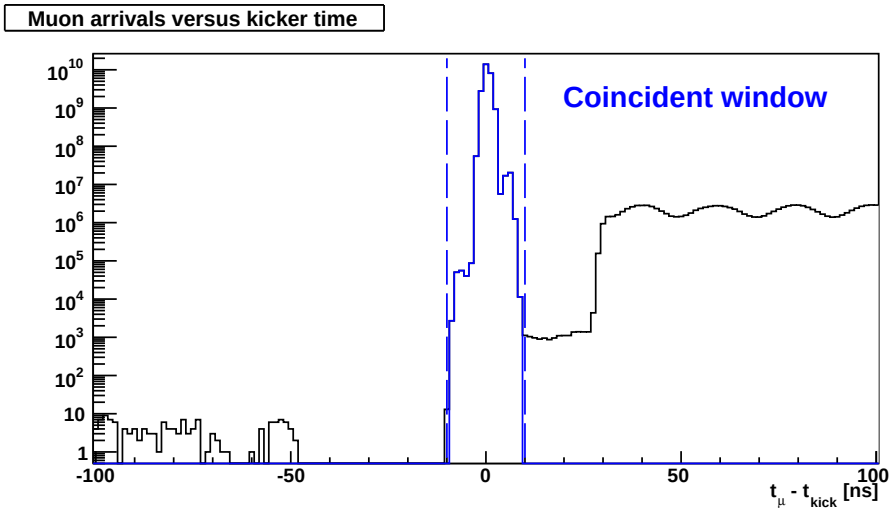

Figure 5.4: Time difference between muon arrival time and the kicker signal. The black curve shows the time differences between the raw muon arrival signals and the kicker. The blue overlay shows the muon arrival times that have the required temporal coincidence with the kicker signal ±10 ns.

time distribution[6] was shown in Figure 4.4. The muon arrival peak is magnified in Figure 5.4, and the accepted muons within the ±10 ns coincidence window are shown in blue.

The presence of a pileup protected hit in the entrance counters serves as a trigger for examining the TPC volume to identify a muon stop. When the muon enters the TPC, it deposits energy along its path, ionizing the hydrogen gas. Although the ionization signal is generated promptly by the incoming muon, time is required for the electrons to drift to the MWPC at the bottom of the TPC. This means that muons that stop near the top of the TPC will be detected later than muons that stop near the bottom of the TPC. The total drift time for ionization energy deposited near the top of the TPC is ≈ 22.5 μs. The digitization interval of the TDC is 200 ns, which corresponds to a ≈ 1.1 mm position resolution in the y-dimension. This y-t coupling is a critical complexity of the TPC and is worth emphasizing. While the cathodes and anodes directly provide x and z information, the y component of the muon stop is derived from the delayed readout time (t_{TPC}) in the MWPC and the assumption that the ionization occurred simultaneously with the muon entrance.

[6]prior to pileup protection

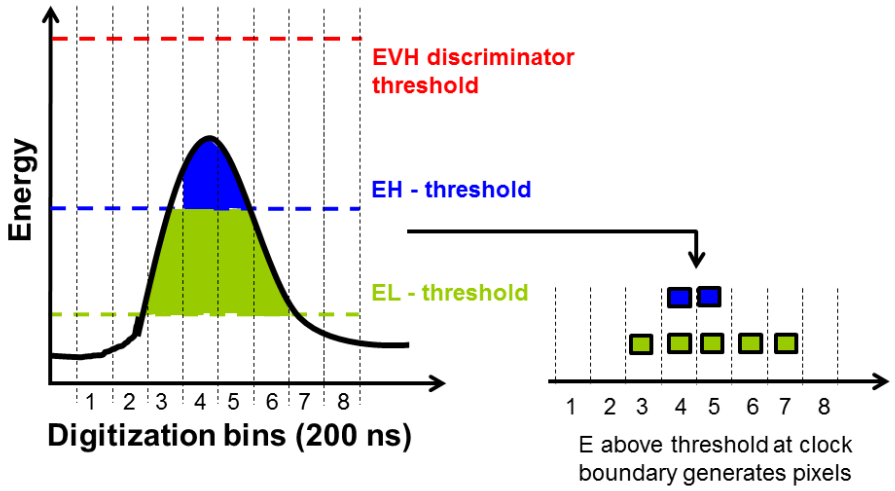

Figure 5.5: The analog signal from one TPC pulse is shown with three discriminator levels (not to scale). The low energy (EL) threshold and the high energy (EH) threshold are used to define the muon track. A very-high (EVH) threshold is used to detect rare events. A TDC hit is generated when a pulse is over the energy threshold at a clock boundary. The wire number and time word comprise a pixel.

The analysis uses discriminated TDC readout of the TPC data. A schematic representation of an analog pulse and the discriminated signals it generates are shown in Figure 5.5. When a pulse is over a specified threshold at a clock boundary, the discriminator produces a hit. The anode (or cathode) and time information from the TDC at a given threshold defines a pixel: $(wire, time)$. Three separate discriminator thresholds are applied to each anode wire. The lowest energy threshold (EL) is set just above noise, such that charge deposition from the ionization track created by the incoming muon will trigger it. The EL threshold is shown in green in the event display.

As muons slow down and stop in the target, there is a peak in the dE/dx distribution called the Bragg peak, as described in Section 3.1. A higher energy threshold (EH) is tuned to correspond to the Bragg peak energy. The EH threshold is displayed in blue in the event display, and was tuned such that the final $\approx$ 4 anodes traversed by the stopping muon produce EH pixels.

The third discriminator threshold was set above the Bragg peak energy in order to identify

"very-high" energy (EVH) depositions. In the rare case that a muon captures on a high-Z nucleus, the subsequent nuclear recoil can deposit a large amount of energy. This threshold is displayed in red in the event display, and is useful to determine the impurity concentration in the gas. Only the EL and EH thresholds are used in the muon stop definition.

Two thresholds, EL and EH are similarly defined for the cathode strips, which are displayed in the upper portion of the event display (from $y = 81$ to 116). The beamline is parallel to the z-axis of the TPC. The muon track is (mostly) perpendicular to the orientation of the anodes, and parallel to the orientation of the cathodes. A channeling effect can occur for tracks that have small deflections in x, with a concentration of the ionization energy on one or two cathode strips. Only the EL cathode signals are used in the analysis because the cathode EH threshold is difficult to interpret.

Clusters of TPC pixels are associated with a single muon track, and the track is fit to identify the muon stop location and other track characteristics. A sample event display that illustrates the data associated with a muon track is shown in Figure 5.6. The muon stop candidates are identified using the following procedure.

5.3.2 Stop Position

Region of Interest. The detection of a pileup protected muon arrival triggers a search for a muon stop in the TPC. The region of interest (ROI) is defined to be the 25 μs after an accepted muon entrance. This is slightly larger than the longest drift time in the TPC. The time windows relevant to the analysis intervals surrounding a muon arrival are organized in Table 5.1.

Track Finding. The EH pixels in the anode plane of the TPC are the primary signature of a stopping muon. The track finder considers all EH pixels in the ROI as potential muon stop locations. An EH pixel is selected within the ROI and is used as a seed position for the track finder. Figure 5.7 is a schematic representation of an ideal muon track that is easily identified. The track finder searches for EL threshold hits near the seed using a next-nearest-

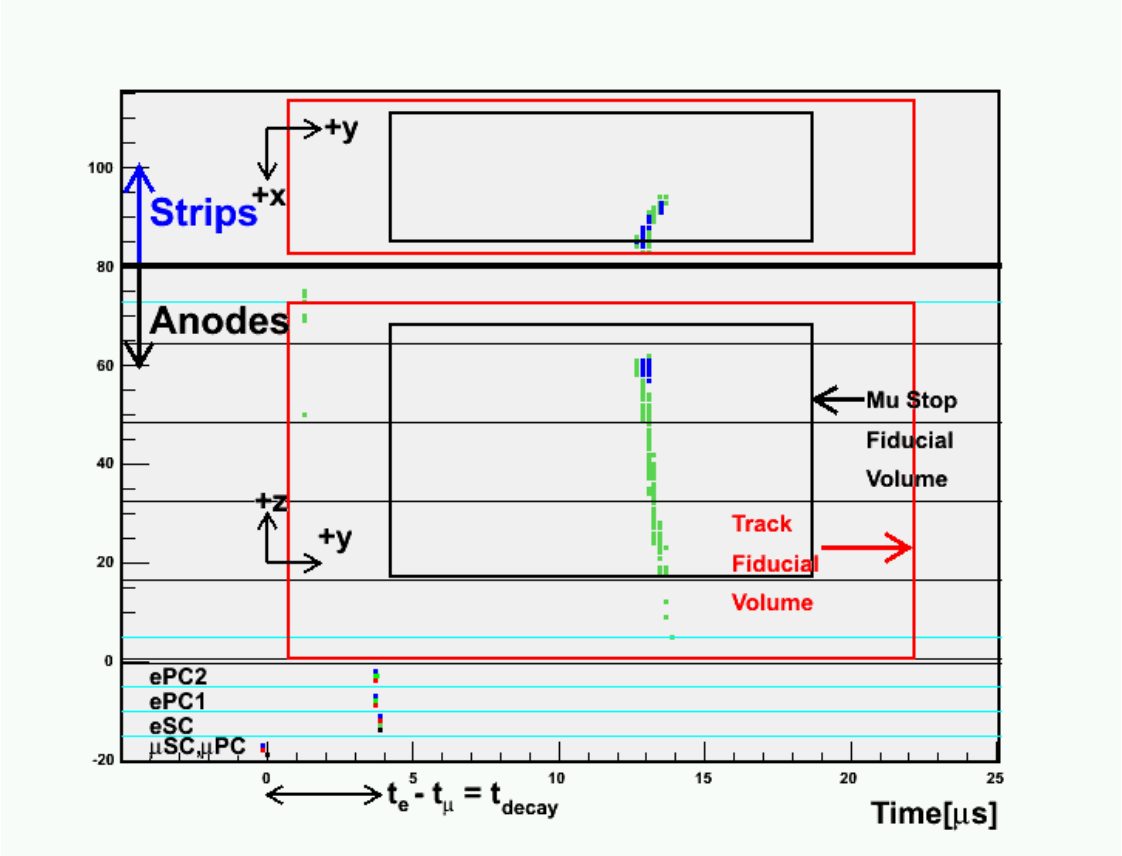

Figure 5.6: A sample event display shows a measurement period containing a muon track as imaged by the TPC (actual data). Hits in the muon entrance counter (μSC, μPC) are anchored at $t = 0$. The incoming muon ionizes hydrogen atoms in its path as it comes to rest near anode 60. A low energy (EL) discriminator threshold is applied to the anode signals and is displayed by green pixels. A high energy (EH) threshold discriminator is tuned to trigger on the peak energy deposition that occurs at the end of the muon track (Bragg peak) and is displayed by blue pixels. The threshold was tuned to trigger ≈ 4 anodes at the end of the muon track. The muon stop anode and the stop time are extracted from the EH pixel information. The upper portion of the event display is used to show the hits on the cathode strips, which provide the x coordinate of the track. The anode, cathode and time coordinates are converted to a stop location (x, y, z). Two fiducial volumes are displayed: the entire track must be contained within the red box (Track Fiducial Volume), and the muon stop position must be identified within the black box (Mu Stop Fiducial Volume). Hit cluster information for the electron detectors (eSC, ePC1 and ePC2) is summarized below the region of interest (ROI).

Event	Start time (μs)	Stop time (μs)	Notes
Muon arrival	t_μ	n/a	Muon arrival detected in the entrance counters
TPC drift region	t_μ	$t_\mu + 22.5$	Max drift time for ionization charge originating at top of TPC
TPC ROI	t_μ	$t_\mu + 25$	TPC hits after a muon arrival are grouped
Measurement period	$t_\mu - 25$	$t_\mu + 25$	Muon entrance counters enforce pileup protection during this window
Kicker (switches)	t_μ	$t_\mu + 0.6$	Detect muon and trigger kicker
Kicker (ON)	$t_\mu + 0.6$	$t_\mu + 25.75$	Beam is deflected

Table 5.1: The relevant time windows for a muon arrival are displayed. The TPC signals in the 25 μs following the muon arrival are grouped together. This is commensurate with the pileup protection window, and the timescale in which the kicker is ON, deflecting the incoming muon beam.

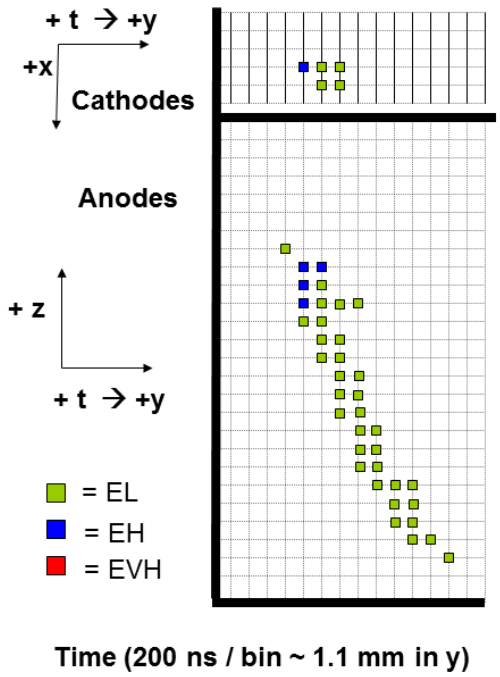

Figure 5.7: A schematic representation of a muon entering the TPC. The coordinates are the same as in the event display with the cathodes positioned directly above the anodes. The track finding algorithm groups neighboring pixels and allows for up to one gap in each dimension (z and t).

neighbor search algorithm. Pixels are added to the track if they are adjacent to any pixel already in the cluster, or if there is a gap of up to one pixel in either dimension.[7] Figure 5.8 is a schematic representation of this algorithm, and depicts the treatment of four example gaps. All of the pixels in this example are grouped together by the track finder, with the exception of the bottom-rightmost pixel in region D. The next-nearest-neighbor approach prevents slight inefficiencies in individual anode wires from breaking up muon tracks. When the algorithm fails to add any additional pixels to the track, it is stored as a muon stop candidate.

For most TPC regions of interest, all of the EH pixels are connected by EL pixels and are grouped together in one muon track. There are instances when the ROI contains two or more unique tracks, primarily when the entrance detectors fail to detect a second incoming muon. The track finder is recursively executed for any additional EH pixels that remain outside of the primary muon track. Each muon track within the ROI is paired with the muon entrance and stored as a muon stop candidate.[8]

For each muon candidate, the next-nearest-neighbor search is executed one final time using only the EH pixels and the resulting cluster is identified as the Bragg cluster. When a muon scatters in the gas, the nuclear recoil of the proton can deposit enough energy to trigger the EH threshold on one anode [59]. To avoid misidentifying a scatter location as a muon stop, a minimum of two EH anodes must be found at the end of a track. The number of consecutive anodes with EH signals in the Bragg cluster is recorded as NC_{EH}. The relevance of this parameter will be explained in Section 6.1.

Stop position ($z_{\mathrm{stop}}, y_{\mathrm{stop}}$) anode plane. Because dE/dx is largest as the muon comes to rest, only the EH pixels within a muon track are candidates when determining the stop pixel. The most downstream anode with an EH signal is identified as the stop anode (z_{stop}). The time of the earliest EH pixel (t_{stop}) on the stop anode is used to define

[7] This includes the diagonal direction as depicted in Figure 5.8 case (c).
[8] The track finding algorithm will search for up to 15 spatially separated tracks within a TPC ROI.

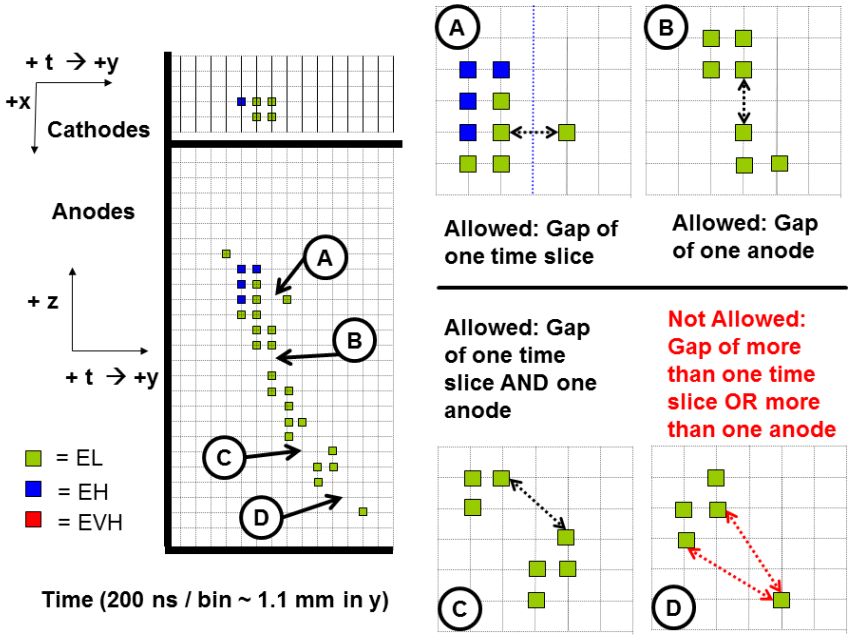

Figure 5.8: The left side shows the same muon track as in 5.7, however several pixels have been removed to illustrate the next-nearest-neighbor search algorithm. A schematic representation of a muon entering the TPC is depicted on the left. The coordinates are the same as in the event display with the cathodes positioned directly above the anodes. The track finding algorithm groups neighboring pixels and allows for up to one gap in each dimension (z and t). Four example gaps are labeled on the left and zoomed in on for closer examination on the right. Gap (A) is missing one time pixel and is accepted. Gap (B) is missing one anode and is accepted. Gap (C) is missing one pixel in both the time and anode dimensions. Gap (D) does not satisfy the next-nearest-neighbor algorithm, and the pixel in the bottom right is not included as part of the muon track.

the vertical stop coordinate (y_{stop}). The drift time is $t_{\text{drift}} = t_{\text{stop}} - t_{\mu}$. The vertical stop coordinate is $y_{\text{stop}} = v_{\text{drift}} \cdot t_{\text{drift}}$, where $v_{\text{drift}} = 5.5$ mm/μs.

Stop position (x_{stop}) cathode plane. Because the muon trajectory is approximately parallel to the cathode strips, the signals collected are often concentrated on a few cathodes, resulting in a very short track. The cathode information is used primarily to confirm the stop location identified in the anode plane. The same track finder algorithm is run to identify cathode tracks using the cathode EL pixels as seeds. The muon stop candidate drift time is then used to link the anode and cathode information. A coincidence is found if any cathode track has any pixels within ± 1 time slices of t_{stop}, which is the inter-

val ($t_{\text{stop}} - 200$ ns, $t_{\text{stop}} + 200$ ns). If multiple cathode islands are found in coincidence, the cathode island containing the largest number of pixels is chosen.

Once an island is identified, the x-position is calculated by taking the weighted sum of the position of all cathode wires on the stop time-slice t_{stop}. In the event that no cathode pixels are coincident with t_{stop}, the weighted sum of the adjacent time slices are used instead. Studies indicate that the precision to which the identified stop position is known is ± 1 time-slice, so the anode-cathode coincidence window need not be any larger.

Track Fitting. Each muon stop candidate that is identified by the anode track finder is fit to a straight line using a linear regression method. All EL pixels in the track are included and a goodness of fit is determined. Approximately 5% of the tracks are not well-described by a straight line fit. It is relatively common for a muon to scatter on a proton in the target and deviate from a straight path. Most of these deflections are forward scatters with a small deflection angle. To accommodate these events, the fitter tests a two-line hypothesis, which uses two line segments connected at a common vertex. Examples of a one-line fit and a two-line fit are shown in Figure 5.9.

Several key parameters are extracted from the track fitter, which are used to further characterize the muon stop definition.

* χ^2_{track}: The reduced chi squared of the fit. One-line fits with $\chi^2_{\text{oneline}} > 1.2$ are tested with the two-line hypothesis. Events with $\chi^2_{\text{twoline}} > 2$ are not well described by the two-line fit and revert to the one-line fit. Tracks with a larger χ^2 will been shown to have a disappearance rate that is consistent with the one observed for the accepted tracks. Processing these events is computationally expensive, so they are discarded. The analysis accepts $\chi^2_{\text{track}} < 2$, for both cases of a one- or two-line fit.

* l_{track}: The length of the fitted track in the anode space. Adjacent anodes and adjacent

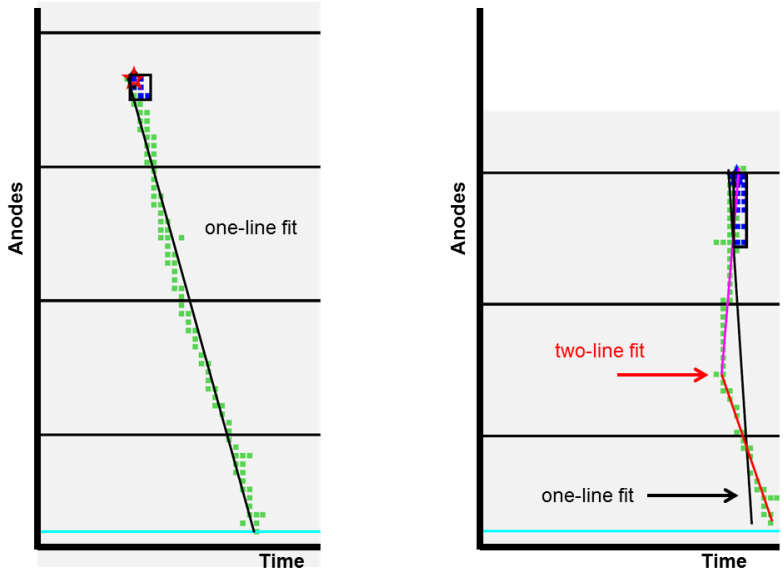

(a) (b)

Figure 5.9: A highly zoomed version of the event display for the anode regions of two muons with the fit results overlayed. The stop location is identified by a star. The identified EH Bragg island is represented by a black box. Figure (a) shows a muon that is well-described by a straight line (black line). (b) shows a muon that fails the straight line fit (black line), and requires a two-line fit. The two-line fitter includes two line segments that share a common vertex (red and magenta lines).

time-slices have different physical separations, so the track length is computed by:

$$l_{\text{track}} = \sqrt{(dz \cdot 4 \text{ mm})^2 + (dt \cdot 1.1 \text{ mm})^2}, \tag{5.1}$$

where dz and dt are the displacements in the anode and clock tick spaces, measured in pixels. When a two-line fit is used, the track length is the sum of the lengths of the individual segments. This eliminates the short tracks which have the highest probability of being misidentified scatter events. The analysis requires $l_{\text{track}} \geq 32$ mm.

* h_{track}: The distance between the end of the fitted track and the identified stop position (track head). Sometimes the analysis identifies a muon stop, but a trail of EL pixels continues past the stop location. Applying a cut on the "track head" parameter rejects

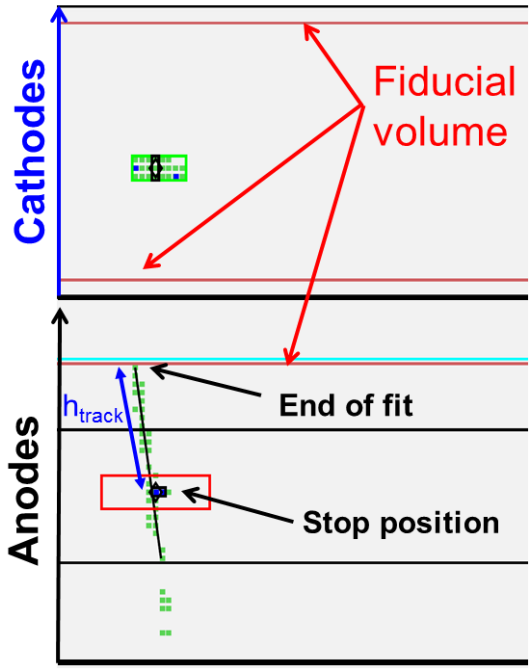

Figure 5.10: A highly zoomed version of a portion of the event display for the anode and cathode regions of a muon with a large h_{track}. The muon stop position is identified far from the end of the track. The EL pixels lead all the way to the back boundary of the TPC. The analysis rejects such events.

muons that probably did not stop in the fiducial volume but left a stop-like signature in the volume. Figure 5.10 shows a sample event display with a muon track having a large h_{track}. Events having a large h_{track} typically exit the back or sides of the TPC. The analysis requires $h_{track} \leq 18$ mm.

Fiducial volume. A fiducial volume cut is imposed to ensure that a muon stop is far away from high-Z materials. All muon track pixels are required to be contained within a loose fiducial volume, and the muon stop position is required to be within a more stringent fiducial volume. The fiducial volume constraints are listed in Table 5.2 and were depicted visually in Figure 5.6.

The requirements listed above represent the choices that were used in the final analysis. The muon stop candidates are not removed from the derived data stream if they fail any of the above cuts. All muon stop candidates are sent to the muon-electron pairing stage,

Coordinate	Pixel range (Track Fiducial Volume)	Coordinate range (Track Fiducial Volume) [mm]	Pixel range (Mu Stop Fiducial Volume)	Coordinate range (Mu Stop Fiducial Volume) [mm]
x	3 – 33	-60 – 60	5 – 31	-52 – 52
y	750 – 22175 ns	-59.3 – 59.3	4237.5 – 18687.5 ns	-40 – 40
z	1 – 72	-132 – 154	17 – 68	-66.4 – 137.6

Table 5.2: The fiducial volume requirements are shown for a location (x, y, z). The position coordinates correspond to information from (cathode number, time slice, anode number), respectively. All pixels in a muon track are required to be within the Track Fiducial Volume. The stop position is required to be within the Mu Stop Fiducial Volume. All ranges are inclusive.

where the cuts are tested to verify that the choices made in the analysis do not distort the extracted disappearance rate.

5.4 Electron Track Definition

The eSC, ePC1 and ePC2 surrounding the TPC are designed to detect outgoing decay electrons, and extract their appearance time, t_e. The minimal electron definition is the detection of a hit in one eSC segment. The additional information provided by the ePC detectors allows for tracking and suppression of backgrounds. The final analysis requirement is a coincidence between the eSC, ePC1 and ePC2.

A variety of electron track definitions were defined in the theses of Steven Clayton [60] and Tom Banks [61] who each analyzed the run 8 MuCap data. The number of coincident planes required in the ePC clustering was varied, but the observed decay rate was stable within 5 s^{-1}.[9] A detailed description of the electron clustering definition used in this analysis is included in Appendix C.2 of Clayton's thesis. The concepts were not changed; however, timing differences were fine tuned to match the run 11 experimental conditions.[10] Because

[9]The 5 s^{-1} uncertainty included in the PRL [14] was based on the differences between the analyses, and the variations within each analysis.

[10]With the addition of extra electronic readouts, the detectors were recabled. The cable lengths affect the

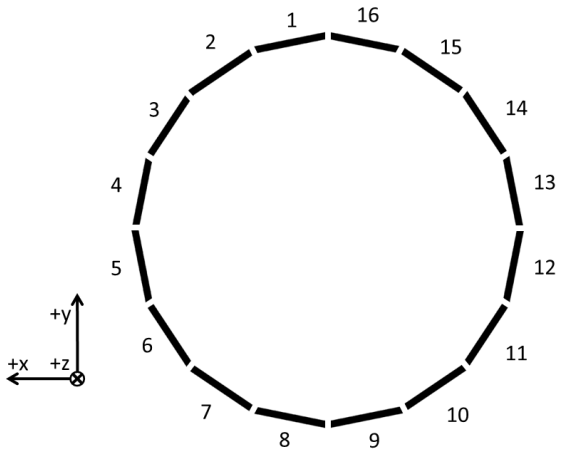

Figure 5.11: A schematic diagram showing the 16 eSC segments. They are numbered from 1 to 16 in a counter-clockwise direction, from the point of view of the muon beam (looking downstream).

of the symmetry of the electron detector, cylindrical coordinates are used to describe the electron track. A brief summary of the electron definition is described here.

5.4.1 Electron Time

The eSC is used to determine the electron time, and the procedure is similar to the determination of the muon time. Software deadtimes of 50 ns are applied to the discriminated signals on each channel.[11] Figure 5.11 is a schematic depicting the 16 eSC segments. Each segment has two scintillating layers, and each layer has two photomultiplier tubes (PMTs). The times of the hits in the individual PMTs are determined separately.[12] A coincidence window of 25 ns is used to pair signals at opposite ends of different layers. A four-fold coincidence is then constructed for the four PMT tubes in one segment. The electron time is defined as the average of the individual PMT times ($t_e \equiv \bar{t}_{eSC}$).

relative timing of the different detector systems.

[11] This deadtime is longer than the 29 ns used for the μSC, which is a very clean detector. The afterpulsing on the eSC tubes was more significant.

[12] The layer closest to the TPC is labeled Inner (I) and the other layer Outer (O). Each layer has a tube on the Upstream (U) and Downstream (D) end. For convenience, the individual tubes are usually labeled IU (inner-upstream), ID, OU and OD.

5.4.2 Electron Vector

The cluster finding in each plane of ePC1 and ePC2 is similar to the cluster finding algorithm described for the μPC in Section 5.3.1. Temporal coincidences are formed and nearby wires are clustered together. For each ePC, this is done for the anode plane and each of the two cathode planes. Temporal coincidences are then formed between clusters in the various planes within a $\pm$200 ns window. Three types of coincidences were constructed:

* cathode-AND : A three-fold coincidence between a cluster in the anode plane and a cluster in EACH of the two cathode planes.

* cathode-OR : A two-fold coincidence between a cluster in the anode plane and a cluster in EITHER of the two cathode planes.

* anode-only : The anode clusters are used and no cathode information is considered, and no coincidence with the cathode planes are formed.

The cathode-AND definition is a subset of the cathode-OR definition. Both definitions allow the extraction of ePC hit coordinates: (z_{ePC}, ϕ_{ePC}). The cathode-OR definition is used for the standard electron definition. The anode-only definition allows extraction of ϕ_{ePC}, but not z_{ePC}, as a coincidence with an additionally plane is necessary to make this determination.

The full electron track definition forms a temporal coincidence of $\pm$150 ns between clusters in ePC1 and ePC2. The coordinates (z_{ePC1}, ϕ_{ePC1}) at the radius of ePC1 and (z_{ePC2}, ϕ_{ePC2}) at the radius of ePC2 form a vector. All ePC1-ePC2 combinations that satisfy the temporal coincidence are created. Figure 5.12 shows the distribution of the ePC1-ePC2 tracks as a function of ϕ and z, projected onto the eSC radius and normalized by the eSC hits. The inefficient region corresponds to the disconnected cards that were described in Section 4.7.1.

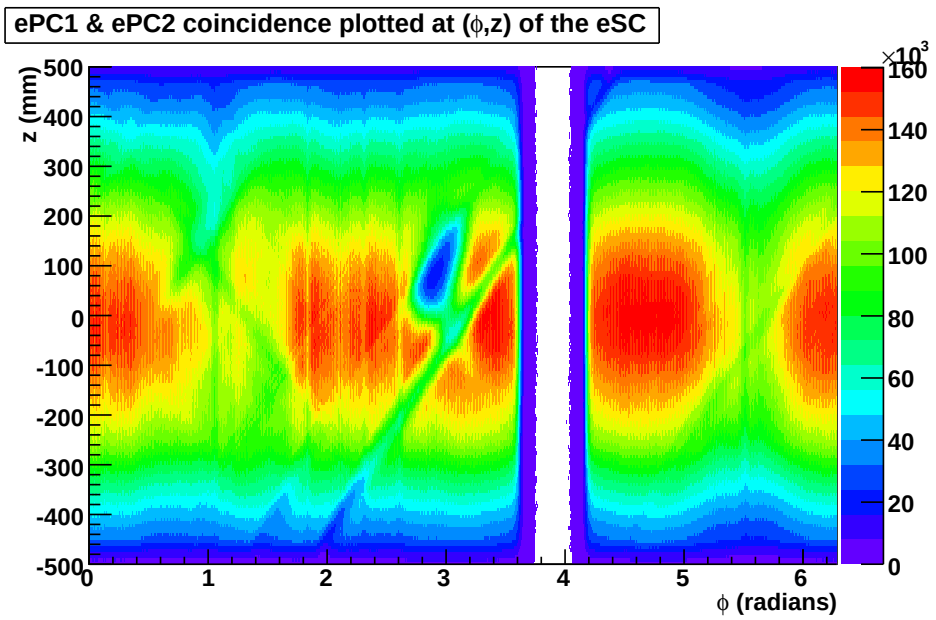

Figure 5.12: The coincidences of hit clusters in ePC1 and ePC2 are combined and plotted at the point of intersection with the eSC cylinder. Inefficient anodes are visible as vertical bands and inefficient cathodes are visible as diagonal bands. The blind region in ePC2 is the gap around ϕ =4.

Each ePC1-ePC2 pair is then matched temporally ($\pm$87.5 ns) and spatially ($\pm$0.3 radians) with the eSC four-fold coincidences. Ninety percent of the eSC four-fold coincidences are matched with exactly one ePC1-ePC2 pair. The remaining ten percent of the eSC hits are temporally coincident with at least two ePC1-ePC2 pairs. The ePC1-ePC2 track that points most directly at the eSC is selected and paired with the eSC.[13] The time of the full electron track is determined by the eSC and the track vector is determined by the ePC1-ePC2 spatial coordinates.

5.5 Muon-Electron Pairs

The analysis forms the muon tracks and the electron tracks separately, only pairing them at the final stages of the analysis. The principal motivation for the late joining of these

[13]The details of the algorithm that chooses between multiple ePC1-ePC2 pairs in the event that there are multiple eSC hits is more complex, and is described in Clayton's thesis [60].

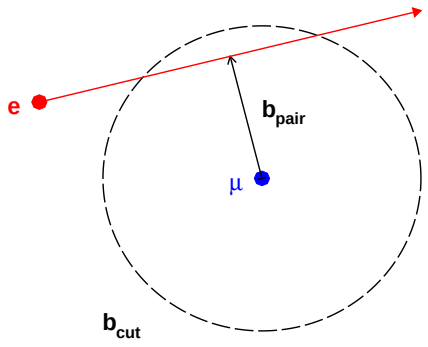

Figure 5.13: Diagram of the reconstructed impact parameter, b_{pair}. This is the distance of closest approach between the reconstructed electron vector (red) and the muon stop location (blue). The dotted circle represents a possible analysis choice b_{cut}. Muon-electron pairs with $b_{\text{pair}} \leq b_{\text{cut}}$ are accepted to reduce backgrounds.

objects is to avoid introducing a time-dependent component to either definition, which will be discussed in Section 6.2. Each muon-electron pair has two defining characteristics: impact parameter and decay time.

The impact parameter is defined as the distance of closest approach (b_{pair}) between the reconstructed electron vector and the stop position of the muon in the TPC, as shown in Figure 5.13. The electron vector is projected back towards the stop position of the muon in the TPC. The distance of closest approach (b_{pair}) between the electron vector and the muon stop position is computed for each pair. A pointing requirement is imposed in the analysis to reduce backgrounds:

$$b_{\text{pair}} \leq 120 \text{ mm}. \tag{5.2}$$

The muon decay time is defined as the time difference between the muon arrival and the electron appearance time:

$$t_{\text{decay}} = t_e - t_\mu. \tag{5.3}$$

5.6 Histogramming and Fitting

The decay times of each muon-electron pair, as defined in equation (5.3), are histogrammed over the interval 0-25000 ns, in 80 ns bins. The decay spectrum is then fit with a function containing three free parameters:

$$N(t) = N_0 \cdot w \cdot \lambda \cdot e^{(-\lambda t)} + B, \tag{5.4}$$

where N_0 is the amplitude, λ is the disappearance rate and B is a flat background.[14] The parameter w is fixed and corresponds to the histogram bin width of 80 ns. The nominal fit range is defined as 160-19000 ns for all plots throughout this document unless otherwise noted. The fitted λ is reported with an additive blinding offset[15]:

$$\lambda_{\text{observed}} = \lambda_{\text{fit}} + \lambda_{\text{offset}}. \tag{5.5}$$

When the collaboration decides to perform the final unblinding, the offset will be removed and the fit result will be reported directly.

As a measure of the goodness-of-fit, the χ^2 parameter is reported in this analysis. The χ^2 is computed by comparing the data to the fit hypothesis for all fitted bins containing data,

$$\chi^2 = \sum_i \frac{(D_i - H_i)^2}{\sigma_i^2} \tag{5.6}$$

$$\Delta\chi^2 = \sqrt{2 \cdot \text{NDF}} \tag{5.7}$$

where, for each bin i, D_i is the data, H_i is the fit hypothesis and σ_i is the uncertainty. The statistically allowed deviation of the χ^2 parameter, $\Delta\chi^2$, is a simple function of the number

[14] See Appendix B.3 for a discussion of the treatment of the cosmic background.

[15] The offset is chosen by the analyzer and is of the order of the singlet capture rate $|\lambda_{\text{offset}}| \sim \Lambda_S$. A separate offset is used when fitting the μ^+ data sets. This is in addition to the overall blinding of the clock frequency that is unknown to the analyzer.

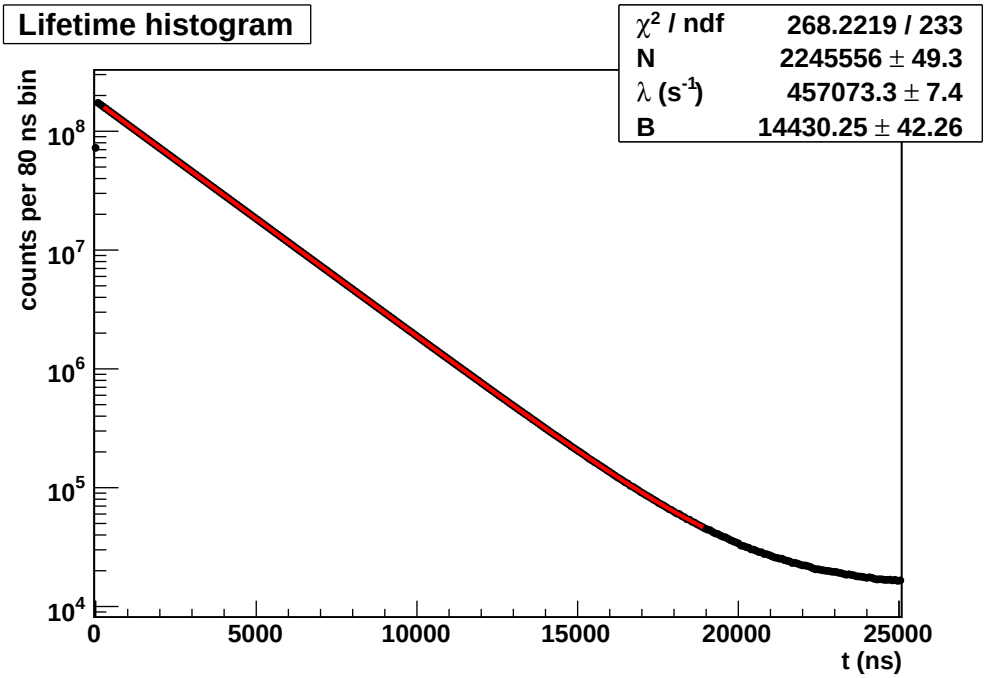

Figure 5.14: A fit to the full run 11 μ^- data set. The three-parameter fit function from equation (5.4) is used to fit the data, and is overlayed in red. The nominal fit range of 160-19000 ns is used.

of degrees of freedom (NDF) in the fit. It is convenient to construct a reduced χ^2 by dividing by NDF: χ^2/NDF. If the model accurately describes the data, χ^2/NDF should be consistent with one. When $\chi^2/\text{NDF} > 1$, the data contains more features than allowed for by the fit hypothesis. When $\chi^2/\text{NDF} < 1$, the fit hypothesis could contain too many parameters. In either case it is also possible that the bin uncertainties are improperly estimated, or that the data set contains a statistical fluctuation.

The analysis cuts are optimized and a full fit to the final data is shown in Figure 5.14. The observed disappearance rate is:

$$\lambda_{\text{observed}} = 457073.3 \pm 7.4 \text{ s}^{-1}. \tag{5.8}$$

This result will be the benchmark for determining systematic corrections in Chapter 6 and consistency checks in Chapter 7.

Chapter 6

Systematic Effects and Cut Optimizations

The MuCap experiment must identify sources of systematic uncertainty in the experimental procedure and in the analysis. Each source may require a correction to the observed result, an additional term in the systematic uncertainty, or both. This chapter explains the systematic effects identified in the run 11 analysis, and summarizes additional effects that are being analyzed by other members of the MuCap collaboration. The analysis cut parameters are studied, and the cuts are optimized to minimize systematic error contributions.

6.1 $\mu + p$ scatter

Muons that appear to stop in the TPC fiducial volume but actually stop somewhere else are problematic. Muons that capture in the surrounding materials introduce fast components to the observed disappearance spectrum. If the fraction of events is small, the additional component manifests as a change in the fitted λ without inflating the χ^2 of the fit. Figure 6.1a contains an event display that demonstrates the type of event that the analysis misidentifies as a muon stop. In this event the muon scatters on a proton in the target ($\mu + p$ scatter) and exits the TPC through the MWPC at the bottom, producing a signal that is prompt with the muon entrance. Beyond the scattering vertex, a few pixels are detected and then the track becomes sparse. The track finder identifies this as a muon stop candidate, and acceptance of such an event would result in a systematic error. This would require a correction, $\Delta\lambda_{\text{scatter}}$

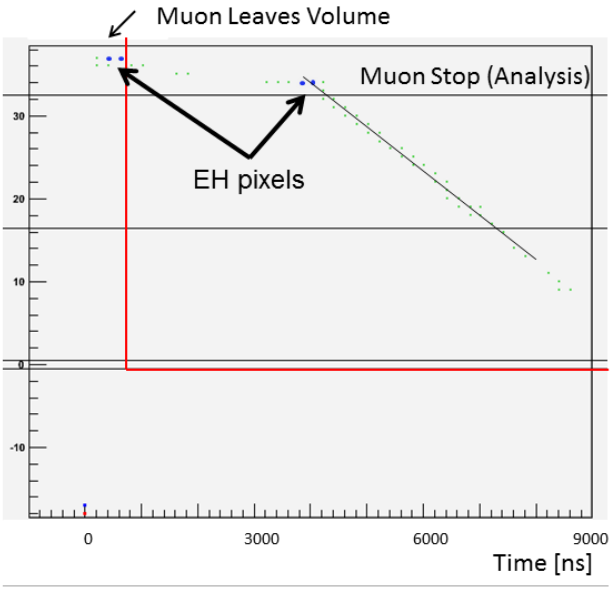

(a)

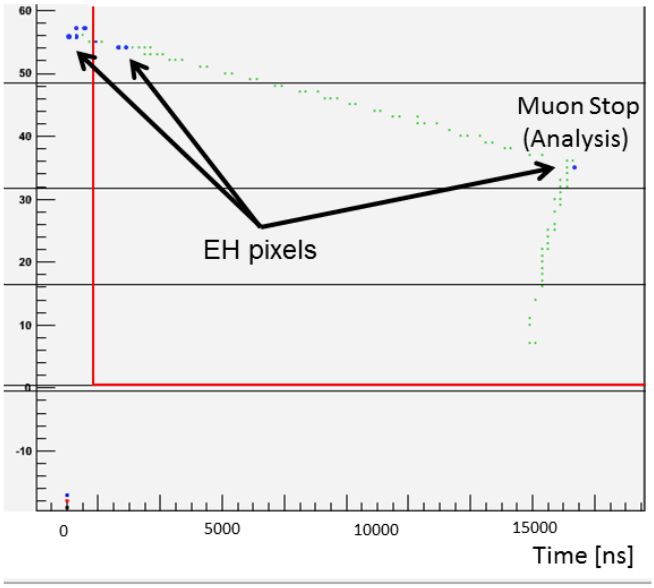

(b)

Figure 6.1: (a) A simplified version of the event display, zoomed to display a $\mu + p$ scatter. The muon enters from the bottom of the image and continues to the left in the event display (downwards towards the MWPC at the bottom of the TPC). The scattered muon leaves a sparse track that is not associated with the main track by the muon track finder. The analysis determines the muon stop position to be in the acceptable fiducial volume. Signals are detected in the MWPC immediately (t=200 ns) after the muon entrance, indicating it is likely the muon actually scattered down through the MWPC and out of the fiducial volume. Inclusion of such events leads to a systematic error; they must be rejected. (b) A similar event that could be identified with a specialized scatter finder in the analysis.

for the inclusion of $\mu + p$ scatter events:

$$\lambda_{\mu^-} = \lambda_{\text{observed}} + \Delta\lambda_{\text{scatter}}. \tag{6.1}$$

These events cannot be accepted in the analysis, and there are several approaches that are used to eliminate them and characterize how many remain in the data. The first approach uses a scatter finder that directly fits for scatter events. Sometimes the track is densely populated and it is obvious that the muon has scattered away from the muon stop vertex that is identified by the analysis. Such an event is shown in Figure 6.1b. It would be ideal to directly fit for a scatter hypothesis and reject all scatter events in this manner. In the analyses of the run 8 data by Clayton and Banks, a direct scatter finder approach was implemented.

There are a few limitations of this method. First, the absolute detection efficiency must be verified with Monte Carlo to ensure that the effects of all scatters are accounted for. There are many scatter candidates with tracks that contain fewer pixels leading away from the scattering vertex than the events shown in Figure 6.1. Depending on the input parameters of the Monte Carlo model, the scatter finding detection efficiency was measured to be between 50 and 95% in the previous analysis. Second, the noise level in the TPC was elevated during run 11 compared with previous data collection periods. Noise on one or two anodes is difficult to distinguish from a vertical scatter on an event-by-event basis. This artificially inflates the observed scatter signal and makes the determination of the scatter finding efficiency more difficult. Third, there is a track-direction-dependent efficiency for triggering the EL threshold in the TPC for the ionization charge along a scatter track. Without thorough Monte Carlo modeling, this could introduce subtle distortions to λ (compare to Section 6.2.3).

The second approach that is used to eliminate scatters applies a cut on the parameter NC_{EH}, which was defined in Section 5.3.2. NC_{EH} parametrizes the extent of the EH-

threshold Bragg island at the end of a muon track. When a muon scatters on a proton in the target, the proton recoils and ionizes electrons in the gas. The energy deposited by the recoil proton may exceed the EH threshold that is usually associated with the muon stop. Both Figure 6.1a[1] and Figure 6.1b contain an EH pixel at the scatter vertex, and in each case that point is (incorrectly) identified as the muon stop location.

The recoil proton has a very short range in the target gas. The Monte Carlo package SRIM was used to simulate $\mu + p$ scatters and to extract the range of the recoil protons in the TPC gas [59]. The maximum range of these protons for the MuCap experimental conditions is ~ 1 mm. Because the separation between the anodes is 4 mm, a recoil proton usually does not have enough range to trigger the EH threshold on adjacent anodes.[2] This implies that $\mu + p$ scatters can be eliminated by imposing an analysis cut requiring that at least two anodes trigger the EH threshold at the end of the track. This condition will be referred to as $NC_{\rm EH} = 2^+$ from now on.[3]

To corroborate the conclusion of the simulation, the data from the neutron counters is examined. The neutron counters are primarily used to make an auxiliary measurement of the molecular formation rate, $\lambda_{pp\mu}$, using Argon-doped data. The muon stop definition is available to that analysis, and a cross-check is performed. The time distribution of the neutron captures relative to the muon is constructed, $t = t_n - t_\mu$ and plotted for $NC_{\rm EH} = 1$ and $NC_{\rm EH} = 2$ in Figure 6.2. The $NC_{\rm EH} = 1$ curve (in black) contains a fast decay component that is prompt with respect to the muon entrance. This component corresponds to muon capture in high-Z materials. The $NC_{\rm EH} = 2$ curve (in blue) contains a much smaller fraction of high-Z capture. The fraction of the $\mu+p$ scatters that end up in $NC_{\rm EH} = 2^+$ bins

[1] There are actually two EH pixels in the first event, however they are on the same anode on adjacent time slices, and correspond to a signal that remains over threshold for two clock boundaries, as described in Figure 5.5.

[2] A small fraction of recoil protons could possibly trigger the EH threshold on adjacent anodes. This could occur (a) when a proton stops on a boundary between the sensitive volume for adjacent anodes, (b) when coupled with noise in the TPC and (c) via interference effects that will be discussed in Section 6.2. Geometrical arguments alone suggest that such events can be no greater than 1/4 of the μp scatter events identified with $NC_{\rm EH} = 1$, and the neutron data suggests that it is smaller.

[3] In general, the superscript notation n^+ will be used to indicate the variable $\geq n$.

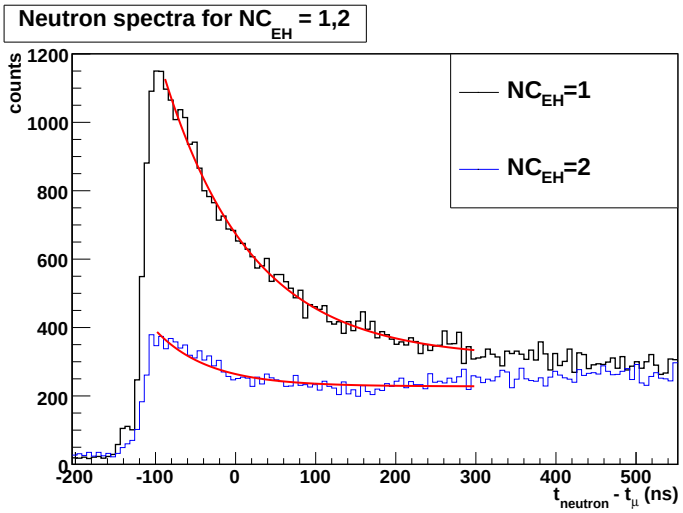

Figure 6.2: Neutron time spectrum with respect to the muon time for $NC_{\rm EH} = 1$ and $NC_{\rm EH} = 2$. The $NC_{\rm EH} = 1$ distribution exhibits a large fast component, visible at early times from events that scatter into the high-Z materials. The $NC_{\rm EH} = 2$ distribution shows a much small fraction of high-Z component. The data is fit with an exponential plus a flat background to determine the upper limit for the fraction of $\mu + p$ scatters with $NC_{\rm EH} = 2$. The muon stop requirements have been relaxed to emphasize the fast component.

is estimated to be no higher than 12%, based on the ratio of the integrals of the background-subtracted spectra from $0 - 1$ μs.

A cut on $NC_{\rm EH} = 2^+$ is imposed in the analysis to eliminate the $\mu + p$ scatter events. This approach was anticipated prior to the data collection of run 11, and the EH threshold was tuned to produce a larger average $NC_{\rm EH}$ for good muon stops. Figure 6.3 shows the distribution of $NC_{\rm EH}$ for all muons that pass all other cuts in the final fit. Only 5×10^{-3} potential muon stops are discarded, most of which are good muon stops. The scatter finder was investigated in the run 11 analysis, but the cut on $NC_{\rm EH}$ was chosen as the preferred method.

6.2 Interference Effects

The detection of the incoming muon and the decay electron and the subsequent formation of the muon stop and electron track in the analysis have been presented entirely independently

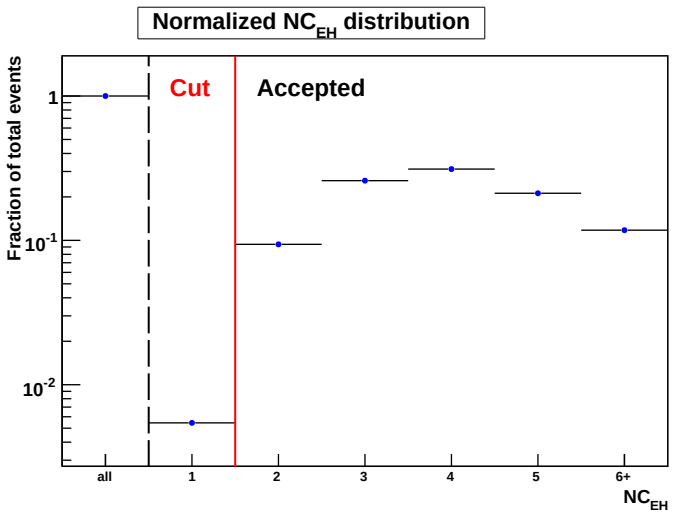

Figure 6.3: The distribution of $NC_{\rm EH}$ for events that pass all other requirements in the final muon stop definition, normalized to the total number of events (first bin). A cut of $NC_{\rm EH} = 2^+$ is imposed to remove the events that contain $\mu + p$ scatters that distort the disappearance rate. About 5×10^{-3} of the total events have $NC_{\rm EH} = 1$.

up to this point. The detector and electronics systems reflect an intrinsic design to keep them separated. The analysis constructs the muon and electron tracks independently, only combining them in the muon-electron decay spectrum in the final stage of the analysis. The beauty of the TPC is its ability to image the charged muons that enter the gas, ensuring that selected events have stopped in the target gas. However, the decay electrons that leave the TPC can also interact with the target gas and occasionally deposit energy along their trajectories. Thus, despite the efforts to keep the muon and electron systems isolated as much as possible, the TPC introduces an effective coupling between them. This energy deposition from the decay electrons is actually a significant process that interferes with the muon stop definition.

One might expect that the deposition of a small amount of energy at some delayed decay time should not introduce any problems. It is necessary to recall the nature of the TPC readout to understand how this interference effect arises. Figure 6.4 illustrates how the ionization energy from the muon track evolves in time. When the muon enters the TPC (Fig. 6.4a), the ionization track begins to drift towards the readout plane (Fig.6.4b). At the

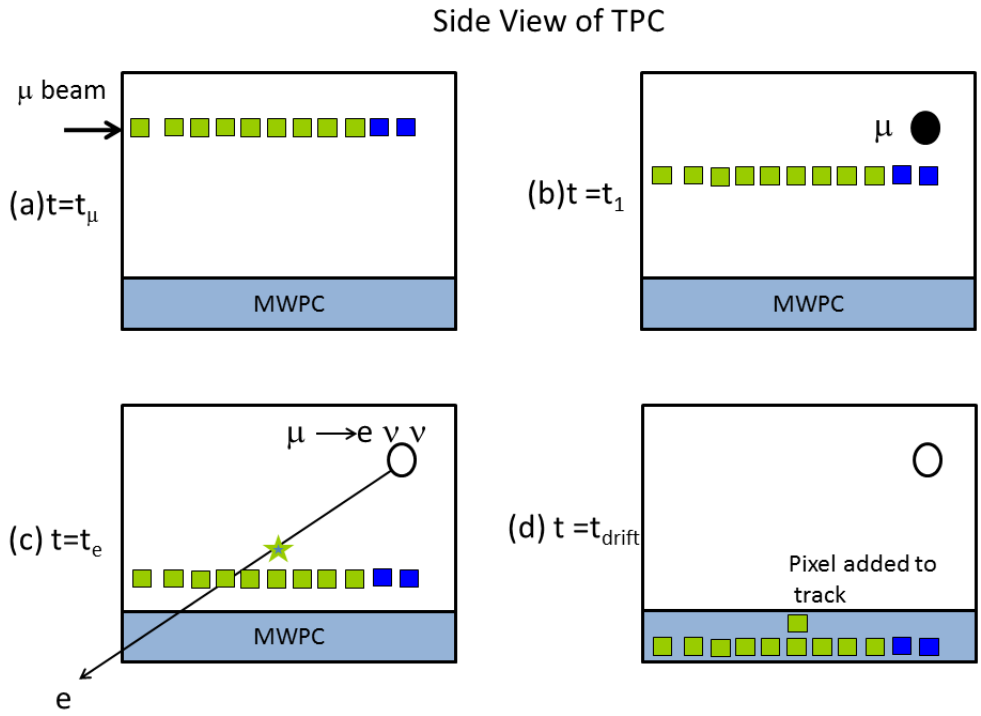

Figure 6.4: A schematic side view of the TPC. (a) The muon enters from the left at $t = t_\mu$ and stops in the TPC, depositing energy along its path. (b) The charge drifts towards the MWPC at some later time $t = t_1$. The muon remains in its stop position. (c) The muon decays at time $t = t_e$ and the decay electron track is shown. The decay electron can deposit energy along its path, depicted by a star in this case. (d) The ionization energy from the muon track reaches the MWPC readout at $t = t_{\text{drift}}$. The energy from the electron is also detected on the next time slice and the track finder groups the associated pixel with the muon track.

decay time t_{decay}, the decay electron is emitted from the muon stop position. In this time, the ionization track drifts a distance $\Delta y = v_{\text{drift}} \cdot t_{\text{decay}}$ (Fig.6.4c). Because the average drift time (~ 10 μs) is long compared to the muon lifetime (~ 2 μs), the ionization track is generally still drifting towards the MWPC when the decay electron leaves the TPC, and the two can intersect. If the electron interaction point in the TPC occurs near the drifting ionization track, that extra energy deposition will arrive at the MWPC at a similar time (Fig.6.4d). When the electron deposits energy along its path, one of several possible scenarios can occur. The possibilities are listed from least to most problematic:

* Case 1: The electron trajectory does not intersect the ionization track, and the amount of energy deposited is less than the EL-threshold. Nothing is observed, and this is not problematic.

* Case 2: The electron trajectory does not intersect the ionization track, but deposits enough energy to trigger the EL-threshold. An EL pixel is observed that is separated from the muon track.

* Case 3: The electron trajectory intersects the ionization track, and deposits enough additional energy to trigger the EL-threshold given that the energy from the muon track is insufficient to trigger the EL-threshold on its own: $E_\mu + E_e > E_{\mathrm{EL}}$. This can add an EL pixel to the muon track, or in its vicinity.

* Case 4: The electron trajectory intersects the ionization track, and deposits enough energy so that the EH-threshold is triggered. This simply requires that the sum of the energy deposited by the muon and the electron on a given anode at a given digitization time exceeds the EH threshold: $E_\mu + E_e > E_{\mathrm{EH}}$, given that $E_\mu < E_{\mathrm{EH}}$.

In fact, the last three cases are all observed in the data. Case 4 is detailed in the next section (6.2.1), which demonstrates how this interference effect distorts the result. The lessons learned can then be applied to the simpler cases. Case 2 and Case 3 are relevant for the EL interference effect described in Section (6.2.3).

6.2.1 EH Interference

Figure 6.5 shows an event display in which the decay electron trajectory (red line) overlaps with the muon track and demonstrates that the processes described in Section 6.2 actually occur in the data. In the plane of intersection, an EH pixel is observed, disconnected from the EH pixels associated with the Bragg peak.[4] In such an event, the energy deposited by the

[4]This event display was chosen because it clearly demonstrates an EH pixel in a location where it is not expected, based on the muon track. The problematic events that will be discussed concern cases where the

electron is added to the energy from the muon track and the sum triggers the EH-threshold, whereas the energy from the muon track alone would only trigger the EL threshold. This is called EH interference.

The reason that this is problematic is because the analysis makes a cut on the number of anodes with EH pixels at the end of the muon track, $NC_{\mathrm{EH}} = 2^{+}$. Via EH interference, the decay electron augments the NC_{EH} parameter of some muon tracks from $NC_{\mathrm{EH}} = 1$ to $NC_{\mathrm{EH}} = 2$, resulting in those tracks being accepted in the analysis. Most importantly, the EH interference promotes those tracks in a complicated function of space and time.

Consider the simplified detector geometry of the TPC and the eSC segments, displayed schematically in Figure 6.6. The eSC segments in the upper region (14-16, 1-3) are located above the position of the TPC. When the decay electron hits these elements, it is not possible for the electron to interfere with the muon track, because the muon track drifts down towards the MWPC and the decay electron travels up. It is possible for a decay electron that hits the midplane eSC segments (4, 5, 12 and 13) to interfere with the muon track. Since the muon track drifts away from the midplane, the geometry only permits EH interference from electrons that decay with $t_{\mathrm{decay}} < 3$ μs. Finally, the eSC segments in the lower region (6-11) are always susceptible to the EH interference. For the midplane and lower regions, the probability for EH interference changes as a function of time. This sort of time-dependent acceptance efficiency wreaks havoc on a precision experiment.

It is instructive to examine the fitted λ distribution as a function of NC_{EH} for all eSC segments summed together. Figure 6.7 demonstrates that the time-dependent EH interference causes a large distortion to λ when each NC_{EH} bin is considered separately. The mechanism responsible for this dependence is a time-dependent shift of events from $NC_{\mathrm{EH}} = i$ to $NC_{\mathrm{EH}} = i + 1$. The change in the number of counts, N_i for $NC_{\mathrm{EH}} = i$ is described by:

$$\Delta N_i(\phi, t) = \kappa_{i-1}(\phi, t) \cdot N_{i-1} - \kappa_i(\phi, t) \cdot N_i \tag{6.2}$$

intersection point is adjacent to the Bragg island, changing the observed NC_{EH}.

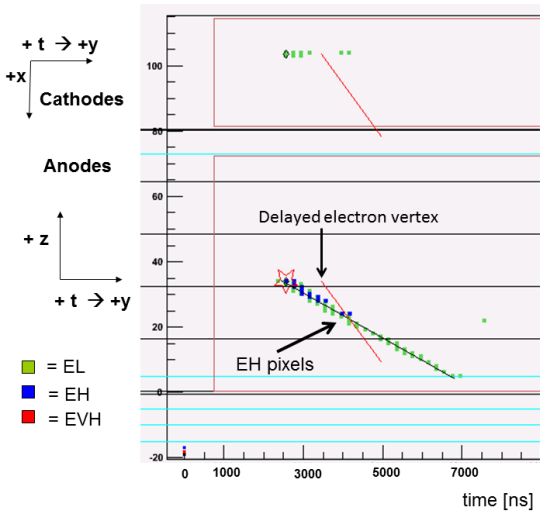

Figure 6.5: A sample event display exhibiting the EH interference mechanism. The red line segments in the anode and cathode spaces represent the reconstructed electron vector. Each electron vector is offset from the muon stop vertex by a time corresponding to the decay time. In the anode space, the electron vector intersects the muon track several anodes upstream of the Bragg island. The energy deposition by the decay electron augments a pulse that would normally only trigger the EL threshold and results in both the EL and EH thresholds being triggered. This is called EH interference.

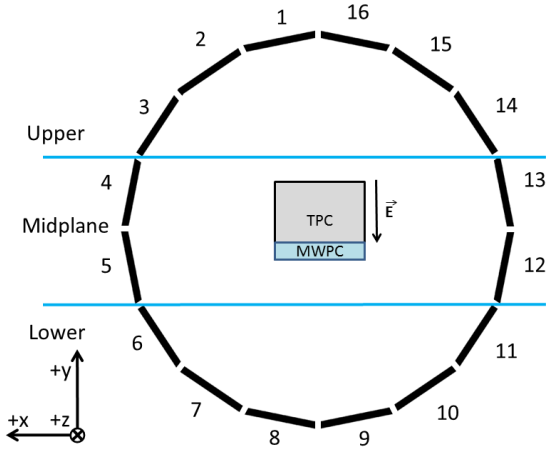

Figure 6.6: The eSC schematic is shown with the TPC. It is not drawn to scale, but is qualitatively representative of the potential interference trajectories. The eSC elements 14-16 and 1-3 are in the upper region, so when these eSC elements are hit, the electron trajectory cannot overlap with the muon ionization track drifting towards the MWPC. Elements in the midplane and lower regions can both be struck by a decay electron that traverses the drifting muon ionization track.

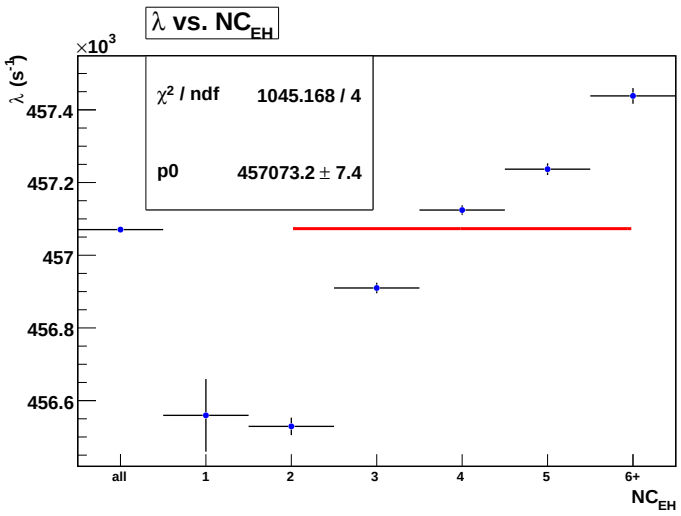

Figure 6.7: Fit results for λ vs $NC_{\rm EH}$, with no cut on eSC segments. The first bin contains the fit to the full data set, $NC_{\rm EH} >= 1$. Bins 1 through 5 scan over $NC_{\rm EH}$, with bin 6^+ containing $NC_{\rm EH} \geq 6$. The observed variation is caused by EH interference.

where $\kappa_i(\phi, t)$ are functions of detector geometry and time. The first term is a source term from the bin to left while the second term is a drain term that describes the flow of events to the bin to the right. Since the κ_i are complicated functions of time, this leads to a time-dependent shift between the bins in $NC_{\rm EH}$. A Monte Carlo model was developed that was able to qualitatively generate this type of variation in the lambda consistency with respect to $NC_{\rm EH}$.

As a check that the variation in λ truly originates from this interference model, the same scan is shown for the upper eSC elements, which are geometrically prohibited from having EH interference. Figure 6.8a shows the excellent consistency of λ with respect to $NC_{\rm EH}$. In the absence of the EH interference effect for the upper eSC elements, the $\mu + p$ scatter contamination in the $NC_{\rm EH} = 1$ bin is easily seen in the form of an increased disappearance rate, as described in Section 6.1. For this subset of eSC segments, it is perfectly reasonable to impose the cut $NC_{\rm EH} = 2^+$ to eliminate $\mu + p$ scatter, since the EH interference does not occur. This strongly supports the initial strategy designed to address $\mu + p$ scatter.

Figure 6.8b is the comparable plot for the lower eSC segments. Here, the EH interference is clearly present, but the average remains consistent with the upper eSC segments. It is

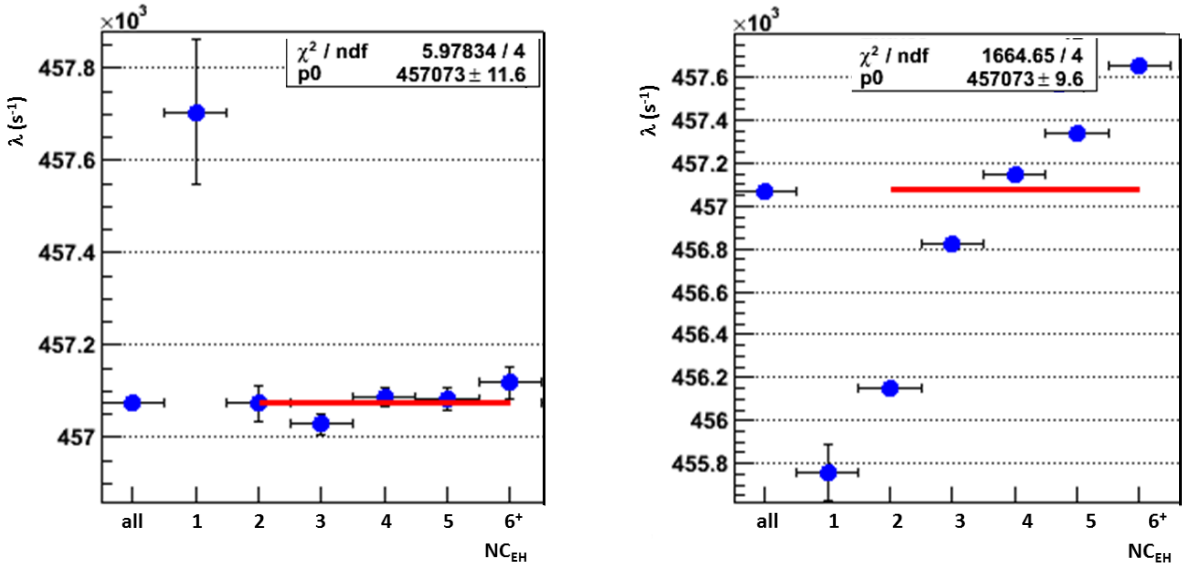

(a) (b)

Figure 6.8: Fit results for λ vs $NC_{\rm EH}$ for (a) The upper eSC segments (14-16, 1-3). The first bin contains the fit to the full data set, with $NC_{\rm EH} = 1^+$. The constant fit to the λ distribution for $NC_{\rm EH} = 2^+$ is consistent with the fit to the full data set (eSC segments 1-16). The constant fit has $\chi^2/\text{NDF} = 1.5 \pm 0.7$, and perfectly describes the data. $NC_{\rm EH} = 1$ is contaminated with $\mu+p$ scatter events that eventually stop in high-Z materials and increase the disappearance rate. (b) The lower eSC segments (6-11). The EH interference effect is clearly present for $NC_{\rm EH}$ bins 1-6$^+$, but the average result of $NC_{\rm EH} = 2^+$ is consistent with the upper segments.

evident that making any selection on $NC_{\rm EH}$ for the lower eSC segments – and the eSC detector as a whole – leads to a systematic shift of λ. It would be preferable to avoid this interference by accepting $NC_{\rm EH} = 1^+$, however the contamination of the $NC_{\rm EH} = 1$ bin by rate-distorting $\mu + p$ scatter events prohibits this approach. The solution is to impose the requirement $NC_{\rm EH} = 2^+$ and correct for the EH interference distortion. This correction procedure will be described in the next section, 6.2.2.

6.2.2 $NC_{\mathrm{EH}} = 1$ Extraction

The strategy implemented is to determine the disappearance rate observed for $NC_{\mathrm{EH}} = 2^+$, $\lambda^{2^+}_{\mu^-}$, and then correct for the EH interference[5]:

$$\lambda_{\mu^-} = \lambda^{2^+}_{\mu^-} + \Delta\lambda_{\mathrm{EH-int}}. \tag{6.3}$$

The μ^+ data provides a powerful method for disentangling the effects of $\mu + p$ scatters and EH interference in the $NC_{\mathrm{EH}} = 1$ bin of the μ^- data. The EH interference effect on the λ vs NC_{EH} distribution is expected to be the same for μ^- and μ^+ data. Additionally, the fit value $\lambda^1_{\mu^+}$ will not contain a high-Z distortion because the μ^+ do not capture. Despite scattering into the surrounding materials, the intrinsic disappearance rate of μ^+ in those materials is λ_{μ^+}. This implies that the difference between the rate in the $NC_{\mathrm{EH}} = 1$ bin, $\lambda^1_{\mu^+}$, and the full fit for μ^+, $\lambda^{1^+}_{\mu^+}$, comes from EH interference. The shape of the λ vs NC_{EH} distribution for μ^+ is used to extract $\Delta\lambda_{\mathrm{EH-int}}$ in equation (6.3). Before making any comparisons in the λ vs NC_{EH} parameter space, the μ^+ data is normalized to the μ^- data to account for Λ_S: $\lambda_{\mu^+} \rightarrow \tilde{\lambda}_{\mu^+}$.

The difference $\tilde{\lambda}^{1^+}_{\mu^+}$- $\tilde{\lambda}^{2^+}_{\mu^+}$ cannot be used trivially to correct $\lambda^1_{\mu^-}$, because the exact shape of the λ vs NC_{EH} distribution depends on the number distribution for NC_{EH}, as described in equation (6.2). The empirically observed number distribution was different for the μ^- data and each of the two μ^+ data sets[6], which is shown in Figure 6.9a.

To extract the correction for $\lambda^1_{\mu^-}$, a linear combination of the two μ^+ data sets is used to describe the μ^- data in the region $NC_{\mathrm{EH}} = 2^+$:

$$\lambda_{\mu^-}(NC_{\mathrm{EH}}) = a_1 \cdot \tilde{\lambda}_{\mu^+_1}(NC_{\mathrm{EH}}) + a_2 \cdot \tilde{\lambda}_{\mu^+_2}(NC_{\mathrm{EH}}) \tag{6.4}$$

[5]The superscript on λ will correspond to the cut imposed on NC_{EH}.

[6]The two μ^+ data sets in run 11 correspond to different settings of the μSR magnet. The resulting NC_{EH} distribution was observed to vary over the course of run 11. Hysteresis in the beamline magnets resulted in slightly different incident beam angles, and slightly different NC_{EH} distributions.

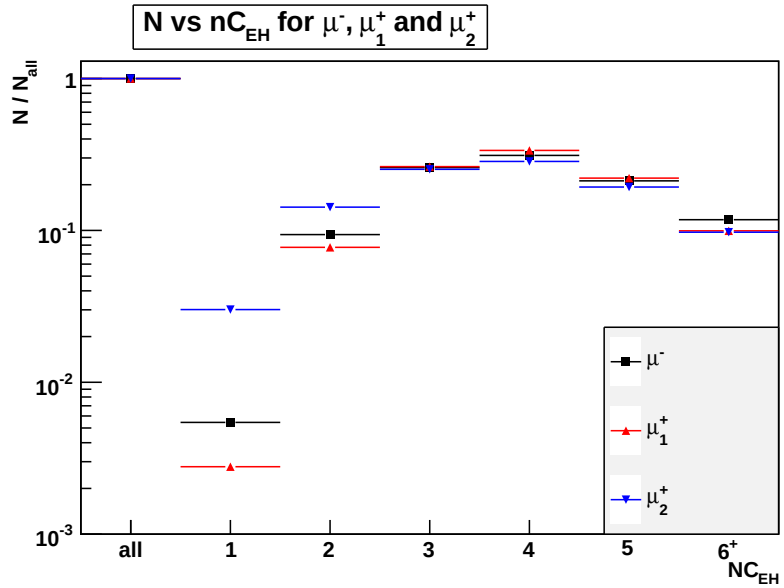

(a)

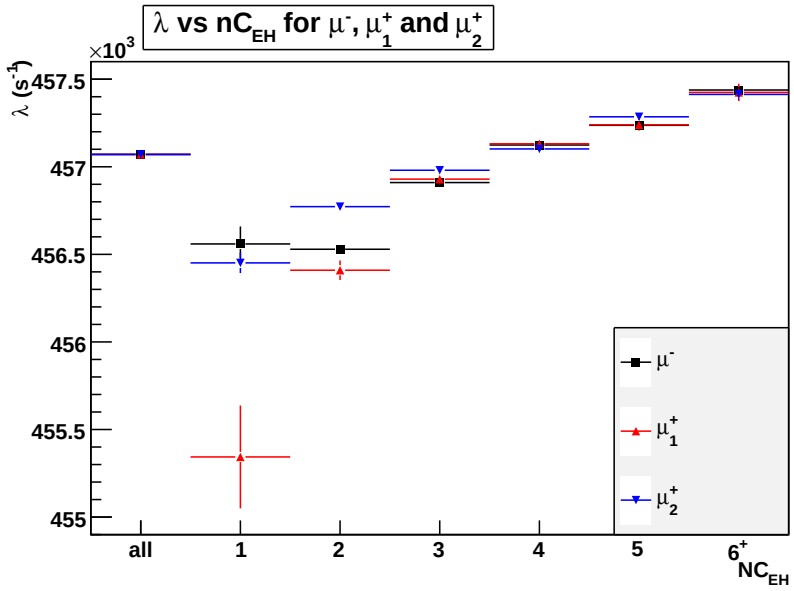

(b)

Figure 6.9: Comparison of $NC_{\rm EH}$ distributions between μ^- and two μ^+ data sets. (a) Comparison of the normalized number distribution N. One μ^+ data set (red) has a slightly higher average $NC_{\rm EH}$ than the μ^- data. The other μ^+ data set (blue) has a slightly lower average $NC_{\rm EH}$. (b) Comparison of the observed λ distribution for the three data sets. In the region $NC_{\rm EH} \geq 2$, the μ^+ data straddles the μ^- data set. It is assumed that, in the absence of $\mu + p$ scattering, the true value of $\lambda^1_{\mu^-}$ should be between the two μ^+ results.

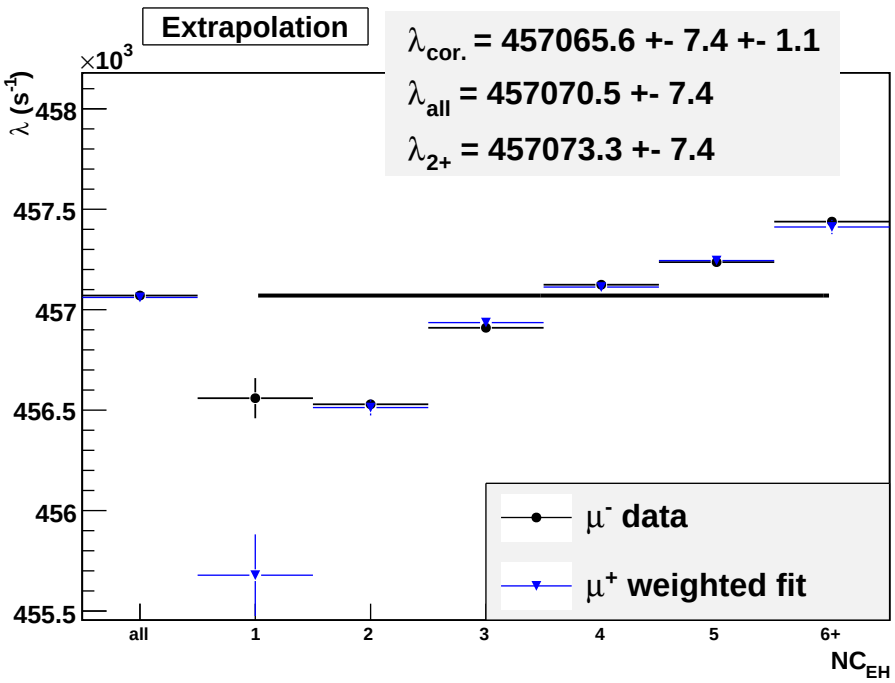

Figure 6.10: Extrapolation results for λ vs $NC_{\rm EH}$. The μ^+ data sets are normalized and then weighted (blue triangles) to reproduce the μ^- data (black circles) over the range $NC_{\rm EH} \geq 2$. This allows the $\mu + p$ scattering effects to be disentangled from the EH interference effects.

The weighting coefficients a_1 and a_2 are determined by fitting the $\tilde{\lambda}_{\mu_1^+}$ and $\tilde{\lambda}_{\mu_2^+}$ to λ_{μ^-} for the five bins with $NC_{\rm EH} \geq 2$ with equation (6.4) and then used to extract the corrected point:

$$\lambda^1_{\mu^-} = a_1 \tilde{\lambda}^1_{\mu_1^+} + a_2 \tilde{\lambda}^1_{\mu_2^+}. \tag{6.5}$$

Figure 6.10 shows the raw λ_{μ^-} vs $NC_{\rm EH}$ in black (squares) and the fitted $\tilde{\lambda}_{\mu^+} = a_1 \tilde{\lambda}_{\mu_1^+} + a_2 \tilde{\lambda}_{\mu_2^+}$ in blue (triangles). The extrapolated $\lambda^1_{\mu^-}$ is combined with the raw data points for $\lambda^2_{\mu^-}$ through $\lambda^{6+}_{\mu^-}$, and the distribution is fit to determine the corrected λ_{μ^-}.

It is then useful to separate the correction for the EH interference from the full results so that the scatter-free data with $NC_{\rm EH} = 2^+$ can be used for the rest of the systematic studies and corrected at the end. To estimate the uncertainty on the method, the extrapolation procedure is repeated with the values of a_1 and a_2 varied by their 1σ errors. The difference between the corrected result and the $\lambda^{2+}_{\mu^-}$ is determined by inserting the corrected λ_{μ^-} and

$\lambda_{\mu^-}^{2^+}$ into equation (6.3):

$$\Delta\lambda_{\mathrm{EH-int}} = \lambda_{\mu^-} - \lambda_{\mu^-}^{2^+} \tag{6.6}$$

$$= 457065.6 \pm 1.1 \text{ s}^{-1} - 457073.3 \text{ s}^{-1}$$

$$= -7.7 \pm 1.1 \text{ s}^{-1} \tag{6.7}$$

where the uncertainty is the systematic uncertainty only. An extrapolation procedural uncertainty of 1.1 s^{-1} is added to the systematics table.

As a cross-check, the corrected λ_{μ^-} is compared to the fit $\lambda_{\mu^-}^{1^+}$, which contains the scattering distortion defined in equation (6.1). In this case $\lambda_{\mathrm{observed}} = \lambda_{\mu^-}^{1^+}$ and the true value comes from the correction procedure above, so $\lambda_{\mathrm{scatter}}$ is approximated:

$$\Delta\lambda_{\mathrm{scatter}} = \lambda_{\mu^-} - \lambda_{\mu^-}^{1^+} \tag{6.8}$$

$$= 457065.6 \pm 1.1 \text{ s}^{-1} - 457070.5 \text{ s}^{-1}$$

$$= -4.9 \pm 1.1 \text{ s}^{-1}. \tag{6.9}$$

The scatter distortion in the run 11 analysis is not expected to differ much from the result extracted in the analysis of Clayton and Banks. In that analysis a correction of -3 ± 3 s^{-1} was made due to $\mu + p$ scatters, which is consistent with this estimate of -4.9 ± 1.1 s^{-1}. In the run 11 analysis, no correction is made for the $\mu + p$ scattering, because the cut on $NC_{\mathrm{EH}} = 2^+$ highly suppresses the acceptance of $\mu + p$ scatters as muon stops. In section 6.1 the fraction of scatters that contaminate $NC_{\mathrm{EH}} = 2^+$ was estimated to be $\leq 12\%$. Combining this fraction with the full scale of the distortion in equation (6.9), the estimate for the maximum contribution to the uncertainty from $\mu + p$ scatters for $NC_{\mathrm{EH}} = 2^+$ is

$$\sigma_\lambda^{\mathrm{scatter}} = 1 \text{ s}^{-1}. \tag{6.10}$$

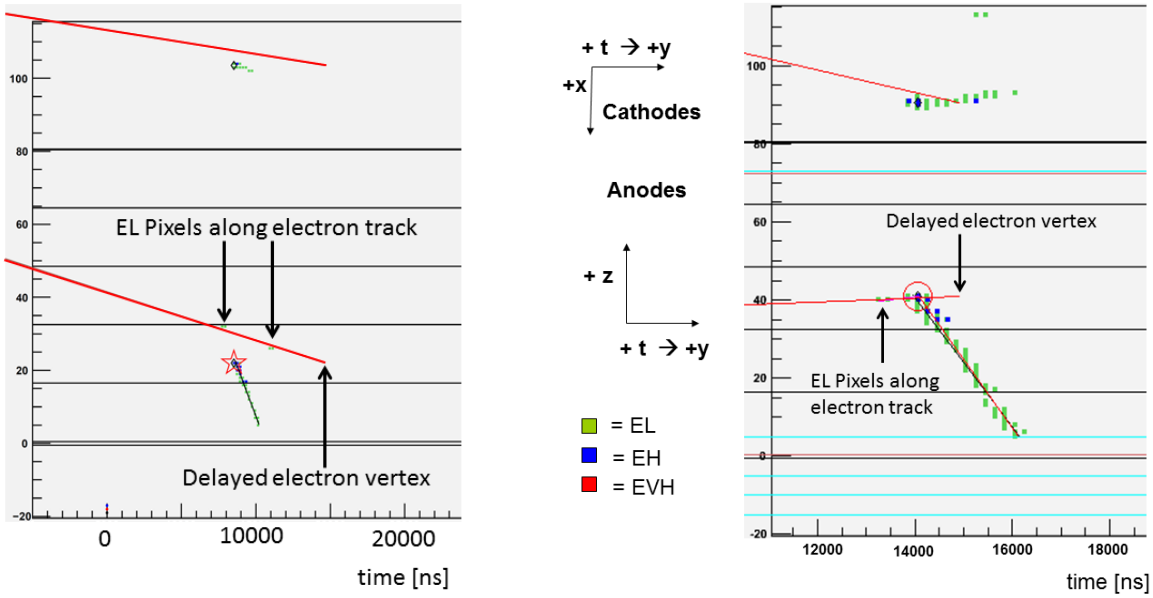

(a) (b)

Figure 6.11: Sample events exhibiting the EL interference mechanism. The red line segments in the anode and cathode spaces represent the reconstructed electron vector. The electron vector is displayed offset from the muon stop location by the decay time (converted into a TPC drift time). (a) EL pixels are observed on two separate anodes at times that overlap with the electron track. (b) The electron vector intersects two EL pixels that are slightly disconnected from the muon track, several pixels to the left of the Bragg island. The energy deposition by the decay electron creates a correlation between h_{track} and the struck eSC segment.

6.2.3 EL Interference

The interaction of a decay electron with the TPC gas can add enough energy to trigger the EL threshold for a pixel in which the energy from the muon is less than the EL threshold; this is EL interference. The lessons learned from the EH interference study can be directly applied to the similar case of EL interference. Namely, there is a correlation between the direction of the electron track and the time-dependent interaction with the muon track. Two event display examples are shown in Figure 6.11a and 6.11b with the reconstructed electron track intersecting extra EL pixels. The trajectory in Figure 6.11a strongly indicates that the decay electron is responsible for creating extra EL pixels in the TPC ROI that are not associated with the muon track.

When the interaction occurs spatially separated from the muon track, there is no interference with the muon stop definition. The analysis records this number of extra EL pixels in the TPC ROI that were unused in the track finder. Figure 6.12 displays λ vs eSC distribution for the condition of exactly one extra EL pixel in the TPC ROI. There is a very strong dependence between the observed rate and the eSC element. The probability that an extra EL pixel is generated by the electron within the TPC ROI is a complicated function of the y_{stop} of the muon. Consider a muon that stops in the top of the TPC, with a drift time $t_{\mathrm{drift}} \sim t_{\mathrm{maxdrift}} \sim 22.5\ \mu$s. Any electron that travels towards the lower eSC segments may interact and produce an EL pixel. However, any electron that travels upward quickly leaves the ROI; even if it subsequently interacts with the gas, it would not be detected as an extra EL pixel in the ROI associated with the muon stop.[7] This time-dependent efficiency for detecting an EL pixel must not couple to the final muon stop definition selected in the analysis; any muon track parameter that couples to it is a potential source of a systematic error. The remaining muon track parameters are discussed in the context of EL-interference.

When the energy deposition occurs near the tail of the muon track, as in the schematic example shown previously in Figure 6.4, it has very minor impact on the muon stop definition. The pixel will be included in the muon track, however the parameter l_{track} will generally remain unaffected. Nearly all muons have tracks that begin at the entrance of the TPC, so the presence of a nearby pixel is unlikely to push l_{track} over the analysis cut threshold. Studies indicate no dependence of the fitted λ on the track length.[8]

The addition of an extra EL pixel to the track will slightly increase the χ^2 of the one-line fit, and occasionally cause the fitter to use the two-line fit. If a two-line fit is used, it may be possible for EL interference to reject the event. In practice, this is not an issue, as the scan of λ vs χ^2 shown in Figure 6.13a demonstrated stability at the chosen cut boundary. Events

[7] This again refers to the intrinsic complexity of the relationship between the TPC drift-time and stop position coordinate, y_{stop}.

[8] The track length is strongly correlated with the anode of the muon stop. A plot of λ vs z_{stop} is shown in Section 7.5.

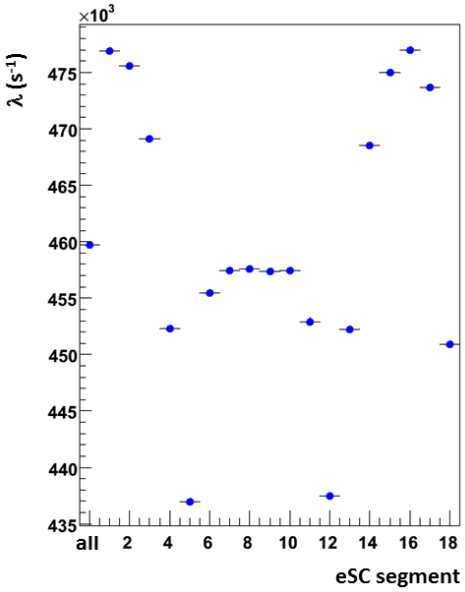

Figure 6.12: Fitted λ vs. eSC segment, when the TPC ROI contains one extra EL pixel, separated from the muon track. The large-scale distortion comes from the time-dependent coupling between the direction and the decay electron depositing a small amount of energy along its path. This plot motivates construction of a muon stop definition that is insensitive to EL interference.

with $\chi^2 < 1$ are distorted via the EL-interference effect, since the presence of an extra EL pixel can cause the event to be reclassified in a different χ^2 bin. The χ^2 cut that is chosen allows the analysis to skip processing the tracks with very large χ^2 without distorting the disappearance rate.

When the extra EL pixel is generated close to the muon stop location, it can interfere with the muon stop definition. The track head parameter, h_{track}, characterizes the extent of the EL pixels in a track beyond the muon stop location. It was designed to identify events that generate an EH pixel, but then continue out through the back of the TPC. Its original role is now mostly covered by the cut on NC_{EH} described in Sections 6.1 - 6.2.2. The presence of EL interference can artificially increase the h_{track} parameter by adding extra pixels past the detected stop location. Figure 6.13b demonstrates that a tight cut on this parameter leads to a distortion. The cut applied, $h_{track} \leq 18$ mm, does not lead to a rate distortion.

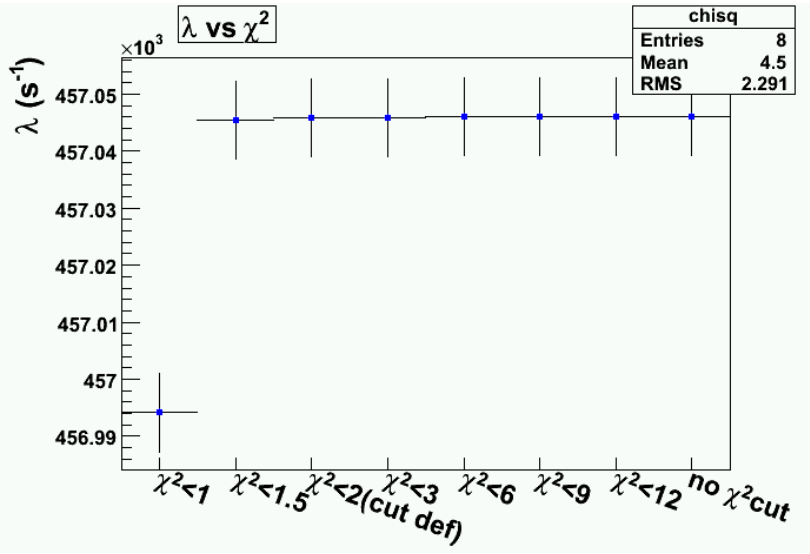

(a)

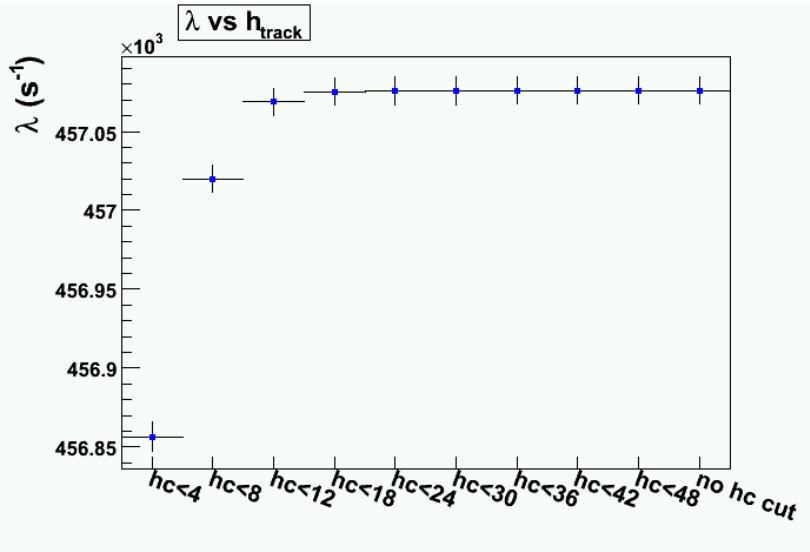

(b)

Figure 6.13: Fitted λ vs muon stop track parameters. Both plots show sensitivity to EL-interference when tight cuts are made on the scanned parameter. (a) The scan vs. $\chi^2_{\text{track}}$of the one- or two-line fit to the muon track demonstrates stability at the chosen definition of $\chi^2_{\text{track}} < 2.0$. The central values of the χ^2_{track} scan are slightly different compared to the nominal result because the scan was performed at an earlier stage of the analysis before the final selection criteria were established.(b) Fit results vs. the track head, h_{track}, of the muon stop (shown here as hc) shows stability for $h_{track} \leq 18$ mm.

The muon stop definition parameters are chosen to be insensitive to the EL interference. There are well motivated physics ideas that may lead an analyzer to cut data based on h_{track}, l_{track} or the number of extra EL pixels in the ROI outside of the muon track. The details of the interference effects prohibits those attempts, because they lead to distortions in the disappearance rate. By relaxing the muon stop definition parameters such that scans near the cut boundary demonstrate stability, the contribution to the uncertainty from EL interference is estimated: $\sigma_{\text{ELint}} = 0\ \text{s}^{-1}$.

6.3 μp Diffusion

Diffusion of μp atoms in the TPC leads to a systematic distortion of the observed disappearance rate because it introduces a time-dependent acceptance of muon-electron pairs. When coupled with the tracking resolution of the electron detectors, this can lead to a significant distortion to the observed disappearance rate. At early times, the μp atom is located at the muon stop position. Over time, the μp atom diffuses with a scale on the order ~ 1 mm/μs, and the average reconstructed impact parameter increases.

The diffusion would not be problematic in the absence of an impact parameter cut in the analysis. However, a cut on the impact parameter, b_{pair}, is applied to reduce backgrounds. The impact parameter cut is also useful for ensuring that the muon stop location is correctly identified within the fiducial volume. If a $\mu + p$ scatter occurs and the muon stop location is misidentified, the reconstructed impact parameter between the electron vector and the identified muon stop will be large. Given these competing aspects, a compromise between a tight cut that reduces backgrounds and suppresses the effects of $\mu + p$ scatter and a loose cut that minimizes μp diffusion distortions must be achieved.

The b_{pair} parameter is plotted in Figure 6.14, and the broad scale of the distribution comes from the electron tracking reconstruction. A detailed analysis of the μp diffusion effect was documented in the run 8 analyses of Clayton and Banks, during which the deuterium

concentration was $c_d = 1.44$ ppm. The μd atoms have a ~ 10 mm/μs scale diffusion due to the Ramsauer-Townsend effect described in Section 3.1.3, so the time-dependent acceptance at the b_{cut} boundary was amplified ten-fold. That was a significant challenge in the run 8 analysis that is no longer present in run 11 due to implementation of the deuterium removal unit (DRU). An upper limit on the deuterium concentration was measured: $c_d < 0.006$ ppm.

The relevant result of the run 8 diffusion analysis was the decoupling of the μd diffusion effects from the μp diffusion, which is expected to be similar for the run 11 data. Several deuterium concentrations were used to isolate the contribution of the μd diffusion. The time-dependent acceptance as a function of impact parameter cut was modeled, and the distortion to the disappearance rate due to μp diffusion was determined.[9] Figure 6.15 shows the fitted λ_{μ^-} as a function of the impact parameter cut. The red curve shows the extracted μp diffusion from run 8, normalized to the run 11 result at $b_{\text{cut}} = 120$ mm. Because this empirically folds in the detector resolution, it is not surprising that the curves are slightly shifted relative to each other. The asymptotic behavior of the diffusion model allows the extraction of the correction: $\Delta\lambda_{\mu p-\text{diff}} = -2.0 \pm 0.5$ s^{-1}. The characterization of the μp diffusion correction as a function of b_{cut} may also prove useful if other systematic effects are better understood by tightening the impact parameter cut.[10]

6.4 Fiducial Volume Definition

The presence of high-Z materials near the edges of the active area of the TPC demands a fiducial volume definition. The TPC fiducial volume is defined so that all accepted muon stops are far away from the materials that can distort the observed rate. The muon stop fiducial volume constraint described in Section 5.3.2 is temporarily relaxed so that muons

[9] The discussion of the model of thermal diffusion from a point source and the model of its effect on the observed disappearance rate is available in Appendix B of Clayton's analysis [60]. The table of fitted values is available in Table 6.6 of the same source.

[10] The effect of the impact parameter cut is being studied for the choice of the electron definition, described in Section 6.6.

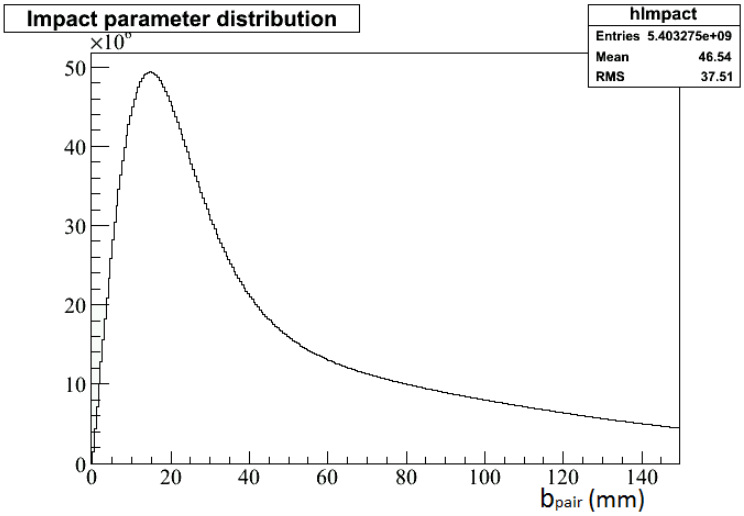

Figure 6.14: Impact parameter distribution. The reconstructed impact parameter is shown for muon-electron pairs that are accepted in the analysis, for a subset of the run 11 production data. The resolution has a broad tail, and μp diffusion causes muon-electron pairs to cross the $b_{\text{cut}} = 120$ mm boundary in a time-dependent manner.

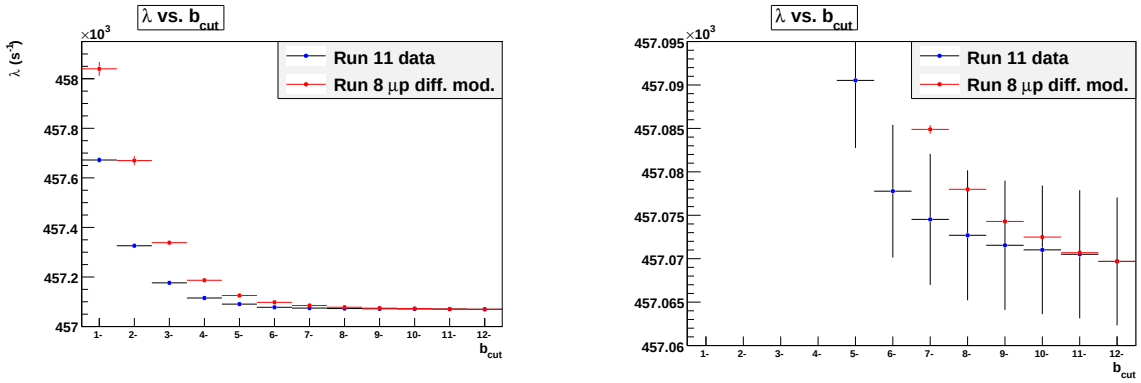

(a) (b)

Figure 6.15: λ vs impact parameter cut shown for run11 data. The extracted μp diffusion component from run 8 is shown for comparison, normalized to $b_{\text{cut}} = 120$ mm.

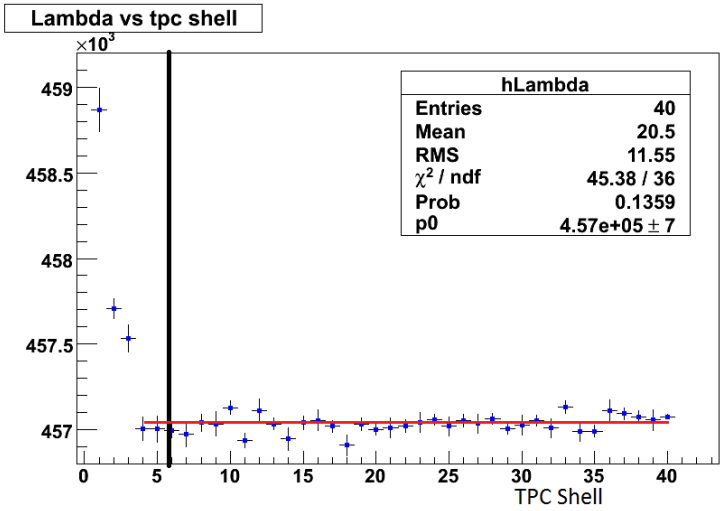

Figure 6.16: Fits for each of the exclusive TPC shells. Shell 1 corresponds to muons that stop in the outermost TPC volume. Larger shell numbers correspond to more central TPC shells. Higher disappearance rates from shells near the edge of the TPC are visible for the outer shells. The vertical line (black) represents the standard fiducial volume cut mapped into shell space.

that appear to stop anywhere in the TPC active area can be studied. A set of exclusive fiducial volume shells are defined, beginning with the outermost sub-volume and ending with a small box in the center of the TPC. The events are sorted in the shells based on the muon stop location. The decay spectrum for each shell is fit separately, and the results of the scan are shown in Figure 6.16. The black vertical line indicates the chosen fiducial volume cut for good muon stops. Large distortions to the disappearance rate are evident for the outermost shells, as expected. Inside the fiducial volume, the distribution of λ values are fit to a constant. The $\chi^2/\text{NDF} = 1.26 \pm 0.24$, which is nearly consistent with 1. The λ values inside the fiducial volume are stable and the consistency with respect to each coordinate $(x_{\text{stop}}, y_{\text{stop}}, z_{\text{stop}})$ will be shown separately in the consistency scans in Section 7.5.

6.5 Noise Cuts

Some TPC regions of interest contain extremely high-multiplicity events (> 1000 hits) as shown in Figure 6.17a. This is usually observed in all planes of the MWPCs in the TPC,

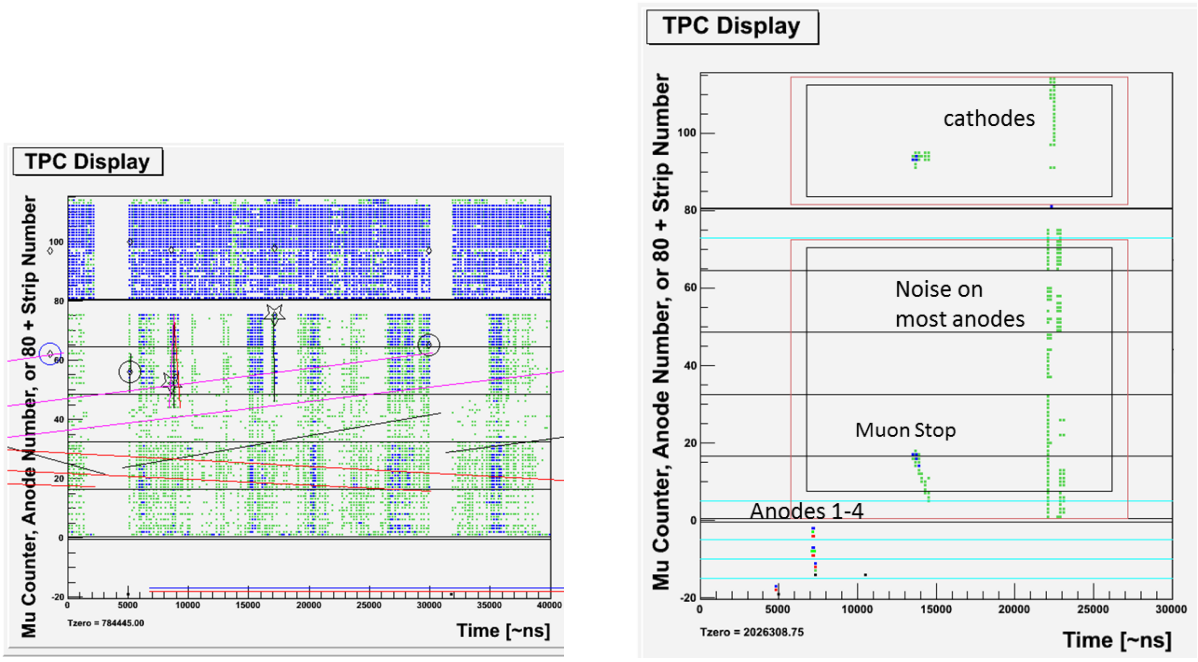

(a) (b)

Figure 6.17: (a) A sample event display of a high-multiplicity event in the TPC. These high-multiplicity events contain $\sim 10^3$ pixels, and usually coincide with high-multiplicity events in the ePCs and μPC. (b) A sample event display containing electronic noise on most anodes.

ePCs and μPC. These events are likely generated by a discharge that affects all detector systems. Cuts are imposed to remove the high-multiplicity events when more than 200 hits are detected in the ePCs, or when more than 100 hits are detected in the μPC. Events are flagged in the TPC when more than 200 hits are detected so that the effects of those cuts can be studied. For the case of the cuts on the ePC hits, the time distributions were studied to ensure that the removed events have the same fit value for λ as the events that were accepted. Additionally, a veto window is implemented following such events to allow for recovery of the detector response and to ensure that pileup protection is performed properly.

The TPC also occasionally has events where hits are observed on many anodes simultaneously for one clock tick, as shown in Figure 6.17b. These topologies do not correspond to the dramatic discharges seen in Figure 6.17a, but rather to some small electronic pickup of noise or RF on the TPC wires, which is then amplified by their sensitive pre-amplifiers.

Figure 6.18: TPC event display for an event flagged with a hit on anode 1. Rejecting events with this characteristic signal leads to a large distortion of the disappearance rate.

Of particular note, anodes 1-4 also detect hits for this type of event. These anodes do not have enough gain to detect incoming muons, as their diameter of 50 μm is larger than the diameter 25 μm of the active anodes 5-72 the TPC.[11] This can be confirmed in the sample events displayed throughout this chapter, (Figures 6.1, 6.5, 6.11), in which the muon track usually begins on anode five. Thus anodes 1-4 have potential to be useful in tagging noise pick-up. Hits on anodes 1-4 are, in fact, not always indicative of the type of noise event shown in Figure 6.17b. Figure 6.18 demonstrates the type of clean event that is flagged because it contains a single EL pixel on anode 1, most likely because the edge anode 1 is more noisy than the rest.

At the initial stages of the analysis, active rejection of events with noise on anodes 1-4 was considered in order to eliminate cases where this pick-up overlaps with the real muon tracks, and thus affects the efficiency of the track finder. In principle, selection cuts of this sort need

[11]This applies to anodes 3, 4, 73 and 74. Anodes 2 and 75 are 100 μm, and the channel labeled "anode 1" is actually connected to a metallic strip on the glass frame of the TPC, and does not correspond to a physical wire. [62]

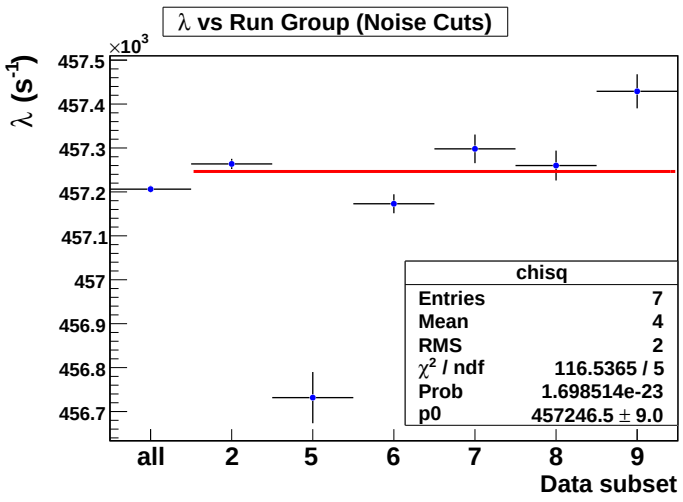

Figure 6.19: λ with respect to several data subsets. Bin 1 contains the fit to the full data set with the noise cut on anodes 1-4 imposed. Different subsets of the data empirically contain different rejection fractions and have a wide range of λ values, as shown in the remaining bins. The fit λ for events that pass this cut are shown here, and a constant fit to their distribution has reduced χ^2 of $\chi^2/\text{NDF} = 23.4 \pm 0.63$.

to be implemented with great care, so as not to introduce distortions to the time spectra. In first order, TPC noise pickup, which is random or even correlated to the μSC signal, should not modify the time distribution, if it does not directly affect the electron detection efficiency. In higher order, one could imagine that known interference effects lead to some correlation with the electron. This could occur if the noise changes the pileup rejection efficiency or if it changes the probability of accepting a muon with an interfering electron crossing its track. These effects are of higher order and are expected to be suppressed. Thus, it came as a surprise that, once events were rejected due to noise signals in anode 1-4, a large variation in λ was observed for subsets of the data. Figure 6.19 shows the λ distribution with respect to these subsets that have different noise levels in anodes 1-4.

A range of studies was performed to identify the origin of the observed discrepancy, including:

* Time distributions of noise pick-up within the TPC

* Time distributions of flagged events vs non-flagged events

* Comparison to μ^+ data

* Geometrical studies to relate the presence of a pixel to a decay electron

* Variation of the subset of muon entrance counters required for muon definition

* Variation of the subset of electron detectors required for electron definition

* Variation of the definition of the number of anodes required to flag the event as noise.

Many correlations were observed, but nothing was identified that had the correct scale to explain the observed discrepancy in 6.19. However, the sum of flagged events and events that pass the cut are extremely consistent as will be shown in Section 7.3. Thus, noise cuts on anode 1-4 are not made in the analysis. The wide range of noise fraction within the subsets for both muon polarities and the excellent agreement within the data sets lends confidence to this approach. A significant set of analysis literature has been produced on this topic, and further studies of these effects are ongoing within the collaboration. It will continue to be investigated prior to the final unblinding.

6.6 Choice of Electron Definition

There is an ongoing effort within the collaboration to study the consistency of the disappearance rate with respect to the electron definition. The strategy to use a subset of the ePC planes in the definition of the electron track was described in Section 5.4.2. A version of the muon-electron decay time histogram is constructed for each definition and Figure 6.20a shows the distribution of fitted λ results for those definitions. Figure 6.20b-d contain regrouped subsets of Figure 6.20a that allow visualization of the allowed set-subset deviation, shown with a red band. The groups in 6.20b-d are strict subsets of the first bin in each plot. The standard impact parameter requirement, $b_{\text{cut}} = 120$ mm is used.[12]

[12]This subset of the full data is consistent with the result in equation (5.8).

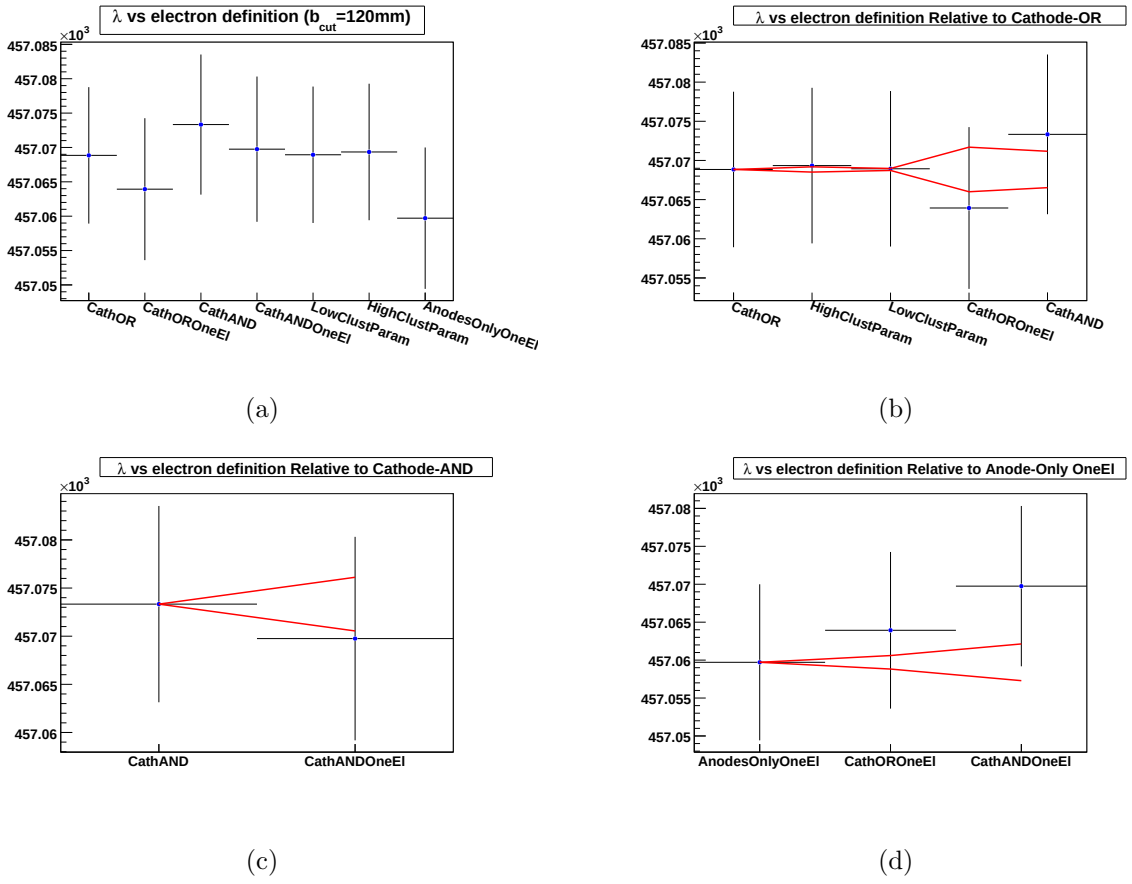

Figure 6.20: Fitted λ vs electron definition for $b_{\text{cut}} = 120$ mm. A subset of run 11 data is used. (a) The variations in the electron definition are shown. (b) The allowed deviation relative to the cathode-OR standard definition are indicated in red. "OneEl" imposes a constraint that only one electron track is present. "HighClustParam" and "LowClustParam" correspond to variations in the ePC track clustering windows, and no dependency is observed. "CathAND" adds the condition that a cluster is found in both cathode planes. (c) The one-electron condition is shown for the cathode-AND data and the allowed deviation is shown in red. (d) The one-electron conditions is shown relative to the least restrictive anode-only definition.

The cathode-OR definition is chosen for the analysis, because it has higher statistics than the cathode-AND definition and contains better background suppression than the anode-only definition. The cathode-OR definition provides the benchmark for comparison within Figure 6.20b. The clustering coincidence window was varied to test the stability of the track forming procedure, and showed excellent consistency. A direct comparison is made to the cathode-AND definition and the difference of 4.9 s^{-1} is larger than the allowed statistical deviation of 2.3 s^{-1} (2.1 σ).

An additional variation of the cathode-OR histogram is constructed that only included electrons from measurement periods containing exactly one electron track ("OneEl"). The difference to the cathode-OR definition is -4.9 s^{-1}, which is larger than the statistically allowed deviation from cathode-OR of 2.8 s^{-1} (1.8 σ). Figure 6.20c shows the same comparison with the single electron requirement for the cathode-AND definition, and the difference (-3.6 s^{-1}) is close to the statistically allowed amount (2.8 s^{-1}). Finally, the cathode-OR and cathode-AND are compared to the anode-only definition, in Figure 6.20d. The disagreement between the cathode-OR and anode-only (4.7 s^{-1}) is much larger than the statistically allowed deviation (1.0 s^{-1}). This is noted with the caveat that the pointing reconstruction in the anode-only definition is poor, as the ePC information only consists of ϕ, and not z. The z coordinate can only be determined by forming a coincidence with a cathode plane. The slight inconsistency in the spread of these results is estimated as a systematic uncertainty, $\sigma_{\text{elec}} = 4$ s^{-1} based on the observed difference in excess of the statistically allowed deviation. This error will be refined for the final MuCap result.[13]

[13]This study reported here has used $\approx$ 75 % of the run 11 μ^- data. The anode-only data is currently only available for the one-electron data and a comparison without this constraint is also desirable. Run 10 μ^- has been fully processed and shows better consistency. The μ^+ data is also being examined. Ongoing collaboration efforts are being made to determine if imposing a tighter impact parameter cut leads to better consistency between the three main definitions, cathode-OR, cathode-AND and anode-only. Additional plots are shown in Appendix B.4.

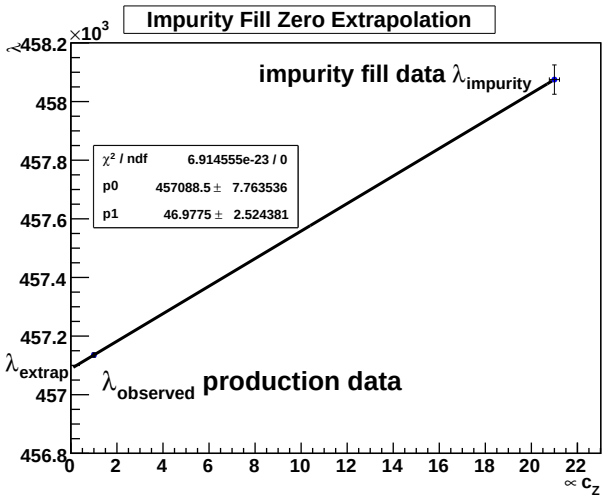

Figure 6.21: A sample zero extrapolation for the impurity correction. The concentration of impurity in the production run and the impurity fill are plotted on the x-axis. The observed disappearance rate is on the y-axis. A fit extrapolates to $c_Z \equiv 0$.

6.7 Impurity Correction

Other analyzers are determining the impurity correction necessary for the run 11 data. The presence of ~ 0.015 ppm of impurities (nitrogen and water) in the hydrogen gas leads to a small increase in the observed disappearance rate. The nuclear recoil of the high-Z capture neutron is occasionally detected in the TPC, and a signal proportional to the number of high-Z captures, $Y(c_Z)$, is extracted.

An impurity-doped target gas was used to measure the rate distortion and apply a systematic correction. The impurities were added with the CHUPS system temporarily disconnected, and several hundred data runs were collected. The two main impurities present in the gas are nitrogen and water, so two separate measurements were made. The nitrogen impurity fill contains a nitrogen concentration $c_{N_2} = 21 \pm 1$ ppm. The water impurity fill uses a water concentration $c_{H_2O} = 3.9 \pm 0.05$ ppm. At higher impurity concentrations the distortions to the disappearance rate are easily measured, and the information is combined with the known impurity concentrations to extrapolate to $c_Z \equiv 0$, as shown in Figure 6.21.

In the initial MuCap result [14], the data contained ~ 0.050 ppm of impurities and the

correction on the observed disappearance rate was determined to be $\Delta\lambda_Z = -19.2 \pm 5.0\ \mathrm{s}^{-1}$. The same method will be used for the run 11 final result and a correction of $\Delta\lambda_Z \sim -6.5 \pm 2\ \mathrm{s}^{-1}$ is expected.

6.8 Entrance Counter Inefficiency

The presence of multiple muons in the TPC can lead to a systematic error if the entrance counters fail to detect both muons. The TPC event display is shown in Figure 6.22 for an event in which two muons clearly enter the TPC. One muon, μ_A, stops in the fiducial volume of the TPC and the other, μ_B, leaves the TPC active area through the side of the TPC. This is visible in the cathode track space and indicated in red. Outside the active area of the TPC, μ_B may stop in some of the surrounding high-Z materials. If the muon entrance counters fail to detect both muon entrances, this event will survive the pileup protection.[14] If the analysis identifies μ_A as a good muon stop and creates a muon-electron pair using the decay electron e_B, a distortion in the observed rate will occur.

The pileup protection imposed in the entrance counters suppresses these events at a 10^{-5} level. A systematic study is underway to artificially increase the muon entrance detection inefficiency, which reduces the pileup efficiency. This allows for the numerical extraction of the distortion to λ as a function of the inefficiency. No correction is applied, but an uncertainty contributes to the systematics table. The systematic uncertainty due to the muon entrance counter inefficiency is estimated: $\sigma_{\mathrm{ineff}} = 2\ \mathrm{s}^{-1}$.

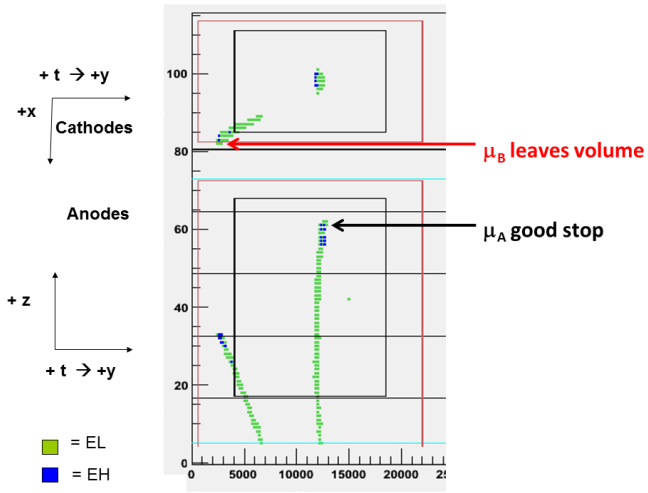

Figure 6.22: An event display is shown with 2 muons entering the TPC in the same ROI. μ_A appears to stop in the fiducial volume. μ_B appears to exit through the side of the TPC (visible in cathode portion). In the absence of pileup protection, the decay electron from μ_B contributes to the pair decay spectrum.

6.9 Summary of Cut Optimizations

This chapter has explained the systematic effects present in the run 11 analysis and justified the choices of the cuts applied to the production data. The subtle interaction of the decay electron with the TPC gas motivates a muon stop definition which is insensitive to small variations in the track details. The primary task is to ensure that the selected muons that stop in the fiducial volume do not have a time-dependent acceptance. The optimized cut choices are summarized in Table 6.1.

[14]Pileup protection does not use the TPC track information. While the example in this event display clearly contains two separate events, trying to impose pileup protection when the tracks overlap is much more difficult. Such an attempt would result in a height-dependent pileup rejection efficiency, and potentially a time-dependent pileup rejection efficiency. Given the sensitivity of the result to the sort of interference effects examined in this chapter, localized TPC pileup protection is not implemented.

Parameter	Optimized Cut Value	Topic	Section
NC_{EH}	≥ 2	$\mu + p$ scatter, EH interference	6.1 - 6.2.2
h_{track}	≤ 18 mm	EL interference	6.2.3
l_{track}	≥ 32 mm	EL interference	6.2.3
χ^2_{track}	≤ 2	EL interference	6.2.3
x_{stop}	$-52 \leq x_{\mathrm{stop}} \leq 52$ mm	high-Z captures, EL interference	6.1, 6.2.3
y_{stop}	$-40 \leq y_{\mathrm{stop}} \leq 40$ mm	high-Z captures, EL interference	6.1, 6.2.3
z_{stop}	$-66.4 \leq z_{\mathrm{stop}} \leq 137.6$ mm	high-Z captures, EL interference	6.1, 6.2.3
elec def	cathode-OR	Electron definition	6.6
b_{pair}	≤ 120	μp diffusion	6.3

Table 6.1: Optimized cut ranges for various parameters

Chapter 7

Data Consistency

7.1 Overview

The disappearance rate (λ_{μ^-}) extracted from the fit of the muon-electron pair histogram in Figure 5.14 will be compared to the precision measurement of the positive muon decay rate (λ_{μ^+}) that was improved by the recent MuLan measurement. Following the prescription of the lifetime method, equation (3.11) will be used to determine the capture rate, Λ_S.

A set of consistency checks are constructed prior to the comparison with λ_{μ^+}, to ensure that the value of λ_{μ^-} is correct. Several analysis parameters are varied to test the stability of the observed disappearance rate. The fitted value of λ **should not** depend on the parameter being studied. If λ varies with small variations of the test parameter, the cause should be identified. The internal consistency of the data is necessary to confirm that analysis choices presented in Chapter 6 do not affect the reported value of λ_{μ^-}. Consistency checks proved to be a powerful tool that exposed some unanticipated systematics during the early stages of the analysis.

During data accumulation, an automated run database records many experimental conditions, such as PSI proton beam current and TPC HV. Experimenters also record any modifications to the experiment[1] so that systematic runs are properly identified and studied separately. For the production data set, several quality controls are imposed:

* Manual checks: The electronic logbook was revisited to exclude runs with known

[1]One example is the sign of the current in the μSR magnet that was used for the μ^+ measurement. For systematic studies, the field is inverted occasionally, and this is recorded manually.

experimental instabilities noted by the shift takers (e.g. DAQ crash, detector failure).

* Beam Polarity: The beam must be tuned for μ^-.

* TPC HV: The TPC HV must be 5100 V. The TPC HV is recorded automatically and runs that are taken while the TPC voltage is different or changing are not considered in this analysis.[2]

* PSI Proton Current: The primary beam current must be non-zero. PSI reports the proton beam current, which is recorded in the DAQ. Runs without beam contain only cosmic data and are not considered. Occasionally the proton beam shuts off during a run, so the statistics in a few runs are much lower than the average.

The runs that satisfy these requirements are processed and the decay times from the muon-electron pairs are histogrammed.

7.2 Consistency vs. Run Numbers

Each data file is assigned a run number and is fitted separately to test the stability of λ over the run 11 data collection period. A change in the experimental conditions (e.g. gas purity) could manifest as a gradual change in the fitted λ. Each run contains $\sim 10^6$ muon-electron pairs, and each spectrum is fit with equation (5.4). The nominal fit range of 160-19000 ns is used whenever possible, however some runs cannot be fit over that range due to lack of statistics. At least thirty counts are required in each bin to satisfy the assumption that the bin errors are gaussian.

Figure 7.1a shows the fit results for each production run: $\lambda_i \pm \sigma_i$. Many systematic runs and μ^+ runs are interspersed with the production data, resulting in missing run numbers.

[2] An automatic safety watchdog program lowers the HV if a sustained current is observed in the TPC, to prevent damage. The shift person is responsible for restoring the TPC voltage to the production setting. The DAQ generally continues during this procedure, so runs that are taken while the TPC HV is being restored must be identified by software.

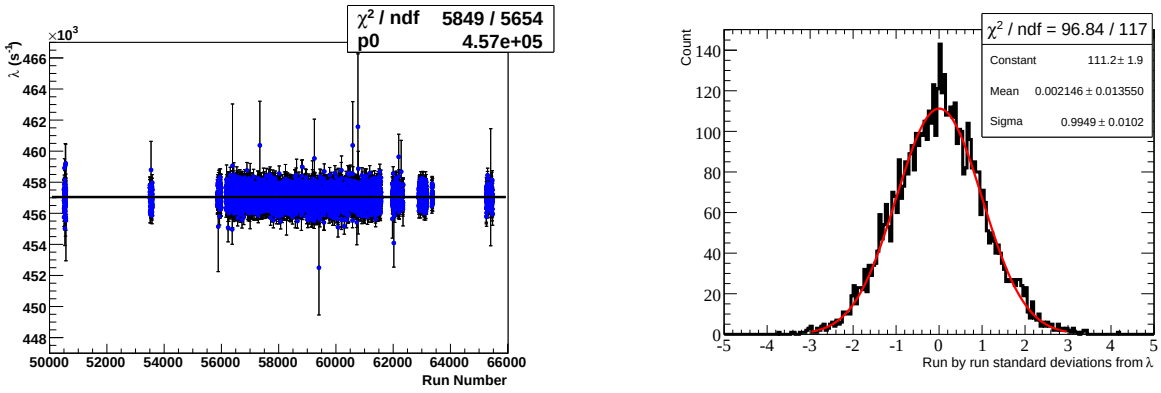

(a) (b)

Figure 7.1: (a) Individual fits for each run number. Runs without data points correspond to systematics runs, μ^+ runs and runs that fail quality control tests. Low-statistic runs with $\sigma_i > 5000$ s^{-1} are excluded from the global fit. The reduced χ^2 of the constant fit is $\chi^2 = 1.03 \pm 0.02$, which indicates the individual runs are consistent. (b) The λ_i extracted for each run is subtracted from the mean of the distribution $\bar{\lambda}$ and normalized by the statistical uncertainty, σ_i: $(\bar{\lambda} - \lambda_i)/\sigma_i$. The distribution is well described by a gaussian.

The λ_i distribution is fit with a constant, and the mean of the distribution is consistent with the fit to the sum of the data. The $\chi^2/\text{NDF} = 1.03 \pm 0.02$, is acceptable. A normalized fit distribution is created by subtracting each fit value (λ_i) from the mean of the distribution ($\bar{\lambda}$) and dividing by the statistical uncertainty of that point(σ_i): $(\bar{\lambda} - \lambda_i)/\sigma_i$. The results are histogrammed in Figure 7.1b and fit with a gaussian distribution. The fit result has a mean of 0.002 ± 0.013 and a sigma of 0.9949 ± 0.01, which demonstrates that the individual runs are statistically consistent with the mean. The data was collected over several weeks, and no obvious trend is observed on this timescale.

7.3 Consistency vs. Run Groups

Run groups are constructed based on the operating high voltage (HV) values of ePC1 and ePC2 and are defined in Table 7.1. The highest stable operating voltage was used for ePC2, and this varied by up to 90 V during run 11. While no macroscopic structure is seen in the consistency vs. run number, a correlation with ePC operating condition is possible.

Run Groups	ePC1 HV [V]	ePC2 HV [V]	TPC HV [V]
2-4	2640	2740	5100
5-6	2640	2780	5100
7	2640	2730	5100
8	2640	2760	5100
9	2640	2770	5100
10	2630	2790	5100
11	2640	2700	5100
12	2640	2790	5100

Table 7.1: Run groups are defined for different high-voltage settings. The production data requires the TPC HV=5100 V. ePC1 was generally stable (2630-2640 V), while ePC2 required operating at lower voltages at the end of the run (2700-2790 V). The first two entries contain a large number of runs, so they were subdivided further chronologically to make the data transfer more manageable. Run group 11 has fewer than 10 runs and is slightly off the pictured scale, however the statistical uncertainty is very large.

Each group of runs was summed and fit with equation (5.4), and the results are shown in Figure 7.2. A constant fit to the distribution of λ vs run group has a $\chi^2/\text{NDF} = 0.38 \pm 0.45$, which is smaller than expected and corresponds to a 2σ outlier. It is a bit surprising that there is not more statistical variation between the individual run groups, but it is not problematic. The consistency of the fitted lambda with respect to the run group, indicates no dependence on the ePC HV setting. The constant fit is consistent with the fit to the sum of the data, shown in this plot as run group 1.

7.4 Fit Range Stability

Varying the choice of fit range provides sensitivity to potential distortions that occur on the time scale of the measurement period. Small distortions in the muon decay spectrum may be identified that would be absorbed into a slightly larger χ^2 in the full fit. The consistency of the three fit parameters as well as the goodness-of-fit χ^2 parameters are all examined.

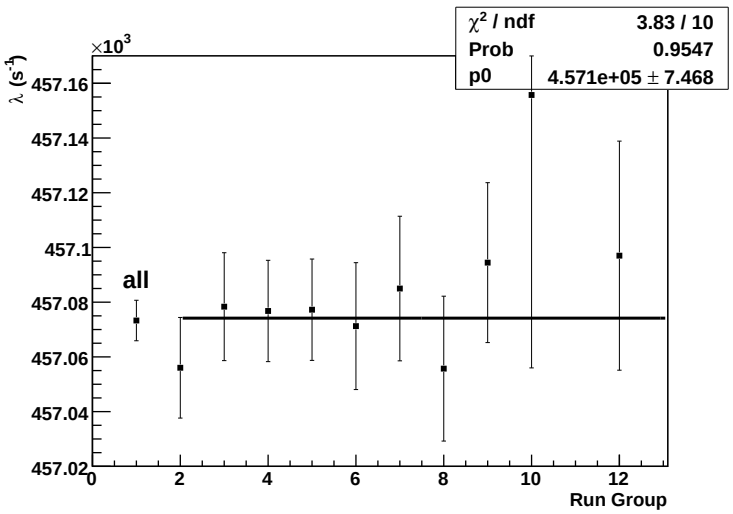

Figure 7.2: Fits to each of the run groups. Run group 1 contains the fit to the full data sets. Each subsequent run group (2-12) contains the fit of files with common TPC, ePC1 and ePC2 high voltage values. The variation of the individual subsets is smaller than expected ($\chi^2/\text{NDF} = 0.38 \pm 0.45$).

7.4.1 Start Time Scan

The start time of the fit is varied from 160-6000 ns. In each fit, the stop time is held constant at 19000 ns. Figure 7.3a shows the scan of the λ parameter, and Figure 7.3b shows the corresponding χ^2/NDF for each fit. The fits are highly correlated since each successive point excludes one additional time bin with respect to the point to its left. A red band is drawn that indicates the 1σ statistically allowed deviation with respect to the standard fit time at 160 ns. The fit results are perfectly consistent with respect to the start time.[3] The χ^2/NDF is marginally high until $t_{start} = 480$ ns, at which point it becomes consistent with 1. Based on the stability of this scan, the recommended start time is 160 ns.

7.4.2 Stop Time Scan

The stop time is varied from 16000 to 22000 ns, while fixing the start time at 160 ns. Figure 7.4a shows the stability of λ over this fit range and Figure 7.4b shows the stability of the

[3]If the experiment were performed many times, about one-third of the fit results would wander outside of the band.

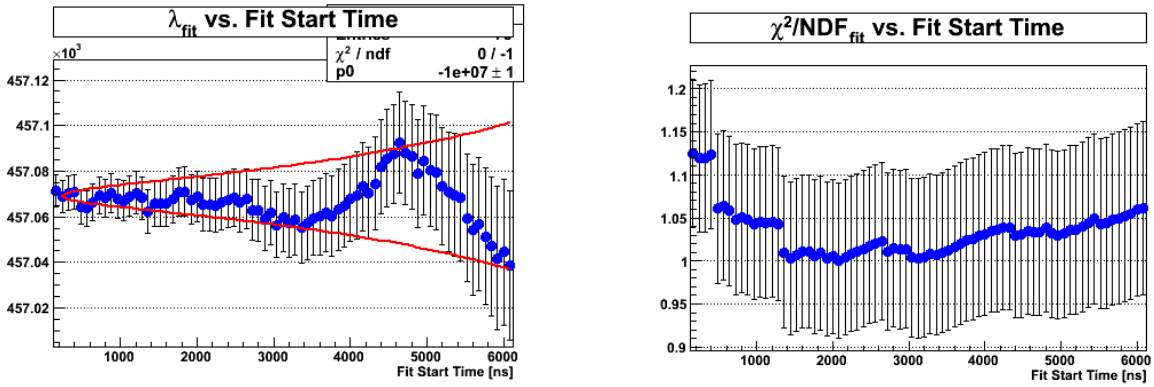

(a) (b)

Figure 7.3: (a) Scan of the fit start time, with the stop time held constant at 19000 ns. The red band represents the statistically allowed set-subset deviation between bins. The fitted λ is completely stable over this range. (b) The χ^2 of the individual fits. Slightly later start times (480 ns) result in better χ^2, however, the λ is stable and the statistical power is greater with earlier start times.

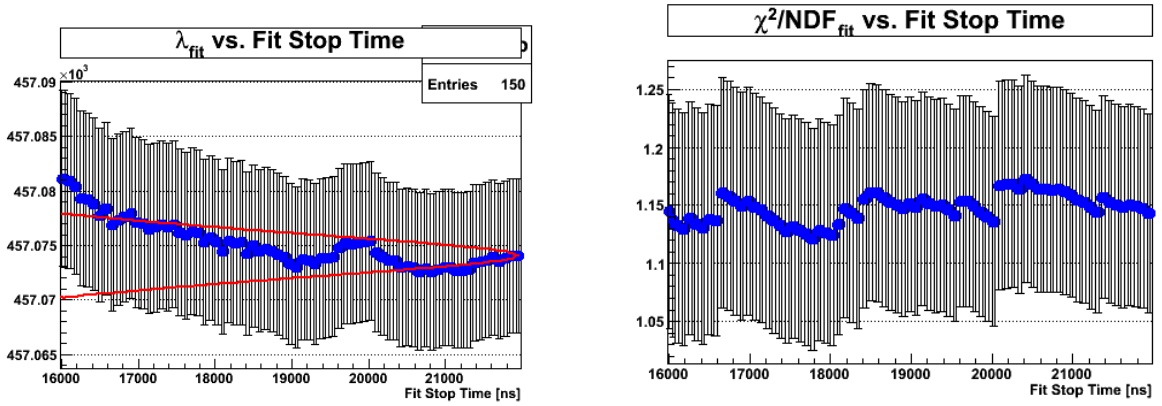

(a) (b)

Figure 7.4: (a) Scan of the fit stop time for a fixed start time of 160 ns. The red band represents the statistically allowed set-subset deviation between bins. (b) The χ^2 of the individual fits. No significant variation is observed.

χ^2/NDF over the same range. The statistically allowed deviation is again shown in red and the fitted lambda values are perfectly consistent. The χ^2/NDF scan is also completely stable, albeit slightly high since the 160 ns start time was used. The recommended stop time used in the analysis is 19000 ns, which allows stable fits on the individual eSC segments that will be described in section 7.6. The stability of both start- and stop-time scans indicate that the fit is stable over the measurement period and chosen fit range.

7.5 Stability vs. Stop Position

The stability of the observed disappearance rate as a function of the muon stop position was shown for the TPC shells in Section 6.4. The consistency of the fitted lambda is examined here as a function of each of the stop position coordinates, x_{stop}, y_{stop} and z_{stop}. λ is plotted with respect to each dimension separately and requires the nominal fiducial cuts in the other two dimensions in Figures 7.5a-c. The χ^2/NDF for the fits with respect to x and z are perfect ($\chi^2_x/\text{NDF} = 1.09 \pm 0.50$, $\chi^2_z/\text{NDF} = 1.01 \pm 0.30$) and the variation with respect to y is acceptable ($\chi^2_y/\text{NDF} = 1.38 \pm 0.42$) . The TPC shell is selected to exclude events that stop close to the edges, and this variation is apparent at the boundaries of y and z.

Studies have been performed to test the stability of λ with finer binning. The observed deviation is higher than allowed when λ is plotted with respect to stop anode number (z); the fit to λ has a ($\chi^2/\text{NDF} = 1.55 \pm 0.18$), which is a 3σ outlier. However, the stopping distributions have also been examined and slight fluctuations in the gain of the individual anodes and cathodes are observed. Figure 7.5d shows the number of events as a function of the anode number, and a 5-10% variation is observed for the central anodes. The largest variations are observed on adjacent anodes, indicating that some events are likely being reshuffled between bins. The data are consistent with the fit near the fiducial volume boundaries (anode 17 and anode 68), so this is unlikely to introduce a bias at the boundaries. The stability in lambda that is observed when the data is rebinned, as in Figure

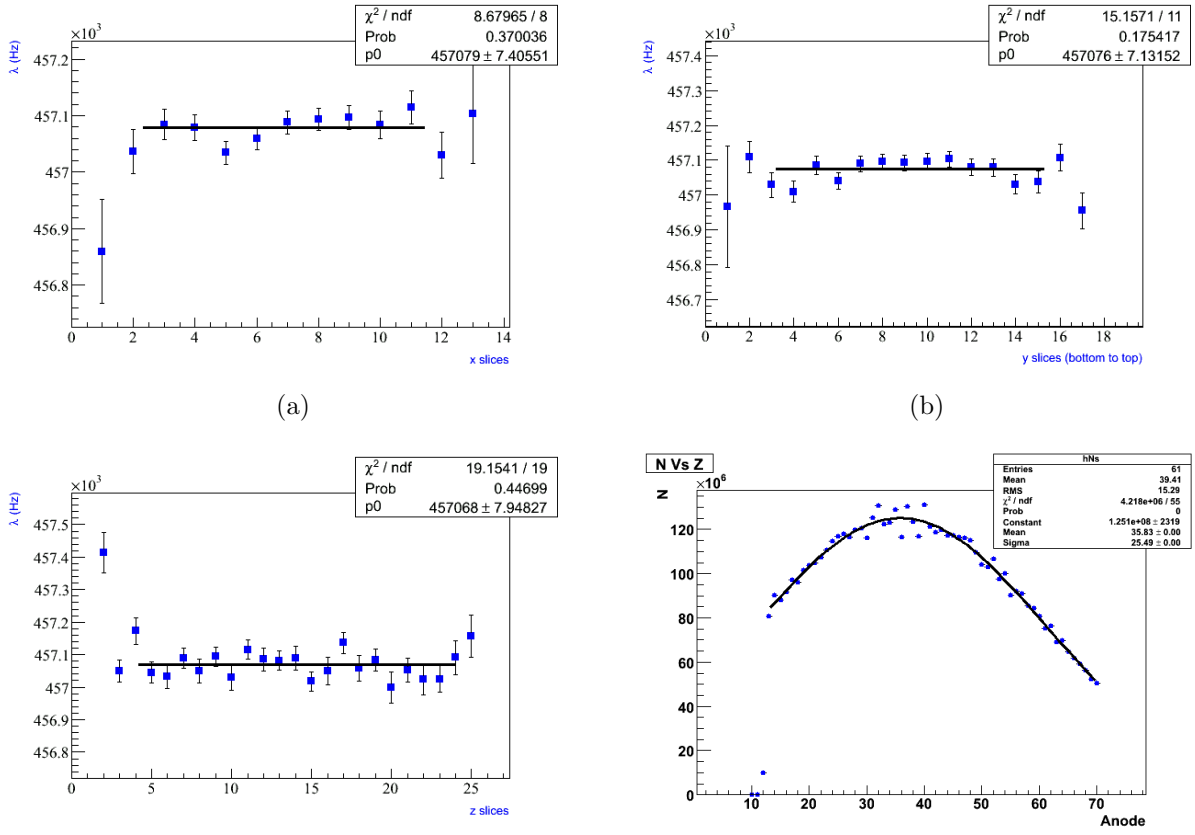

Figure 7.5: Fitted values with respect to the muon stop coordinates. λ is plotted with respect to (a) The transverse coordinate x_{stop} is binned into 13 slices. The outer slices are excluded. (b) The vertical stop coordinate y_{stop} is binned and fit over the central range. (c) The stop anode corresponding to z_{stop} is binned and the central range is selected. (d) N is plotted with respect to the stop anode. A deviation near the center occurs indicating that some anodes are slightly more likely to be considered the stop anode than their neighbors. No fiducial volume cuts in z are applied for this study.

7.5c, indicates that these fluctuations are not a concern.

7.6 Consistency vs. eSC Detector Element

The consistency of λ with respect to the azimuthal angle of the electron played an important role in the understanding of several subtle systematic effects that were discussed in Section

6.2. The direction of the decay electron is uncorrelated with the decay time.[4] If the analysis definitions remove all coupling to time- and angle-dependent acceptance efficiencies, the fitted λ will not exhibit any angular dependence. This is observed by subdividing the data based on the number of the eSC element in the electron track. Figure 7.6a shows the fitted number of events (N) for each eSC element. There are a few notable features. There is a large inefficiency for elements 10 and 11 which comes from the inefficient ePC2 anodes. The smaller inefficiency in elements 6 and 7 is the result of shadowing by the TPC frame. In principle a similar inefficiency is present for elements 10 and 11, however this is only evident in the raw eSC hit rates.

Figure 7.6b shows the fitted background (B) in each eSC element, normalized to N. The plot is not zero-suppressed, and the large variation comes from the cosmic background. Elements 1, 8, 9 and 16 have the largest cross-sectional view of the cosmics. Cosmic rays are observed to comprise approximately half of the total background.[5]

The muon-electron pair decay spectrum is fit for each eSC element and the results are shown in Figure 7.7. The distribution is fit with a constant, which is in perfect agreement with the fit to the sum of the data. The χ^2/NDF is 15.1/15, which indicates that the final fit result is independent of the trajectory of the electron tracks. The λ vs eSC element consistency check was a powerful tool in diagnosing the complicated interference effects in the TPC. With the cut optimizations chosen in the analysis, this λ distribution has been completely stabilized.

7.7 Summary

Chapter 6 introduced a variety of subtle effects that could potentially distort the observed disappearance rate. This chapter has demonstrated that the optimization of the cuts in the

[4]This is different from the positrons from free μ^+ decay, whose decay direction is correlated to the net polarization of the μ^+, which precesses in the imposed μSR field. The μ^- become depolarized upon entering the singlet state of the μp atom.

[5]See Appendix B.3 for the treatment of the cosmics in the fitting.

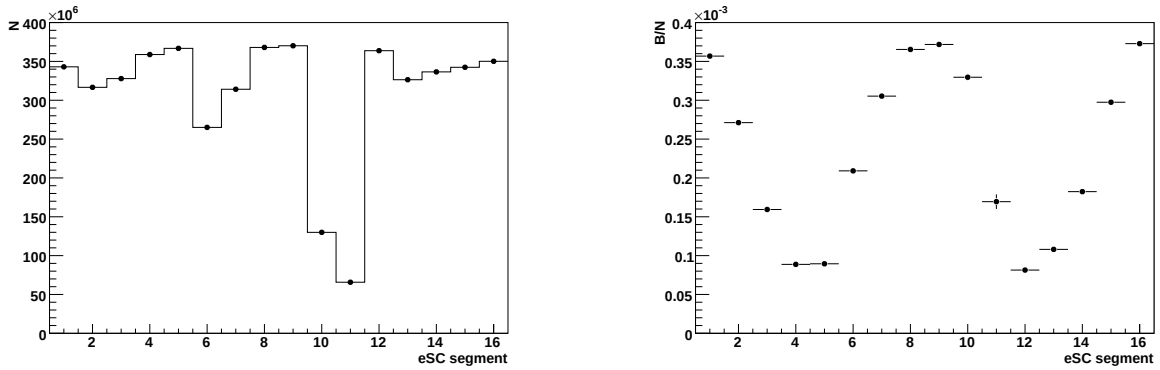

(a) (b)

Figure 7.6: (a) Fitted N distribution vs. each eSC segment. The deficiency at eSC segments 10 and 11 corresponds to the disconnected anodes in ePC2. Additionally, a shadowing of the TPC frame accounts for a symmetric non-uniformity that affects elements 6, 7, 10 and 11. (b) The ratio of the fitted background to the number of hits. A cosmic background is clearly evident, with the elements with a vertical normal vector having a higher cosmic flux. This is accounted for in the fitting method.

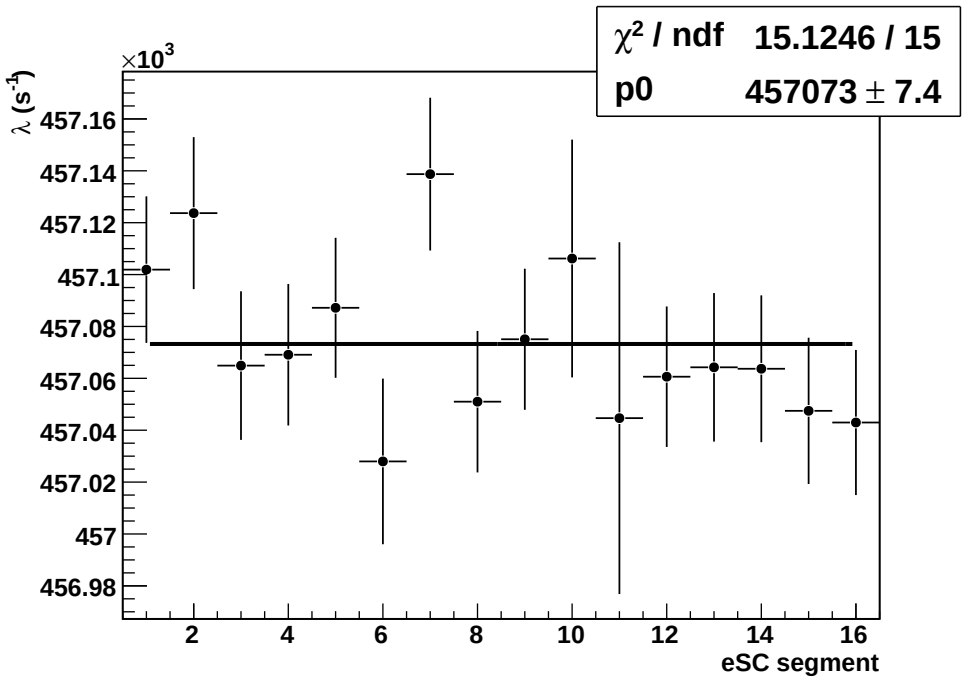

Figure 7.7: Fits to the individual eSC segments. No azimuthal dependence is observed, as the χ^2/NDF is consistent with one. The fit to the sum is compatible with the average of the individual fit results.

muon stop definition and the electron track definition has produced a stable result. The consistency of λ has been stabilized with respect to the analysis parameters.

Chapter 8

Results and Discussion

The focus of this thesis has been the development and the demonstration of methods necessary to analyze the MuCap experiment with a precision commensurate with the statistical precision achieved for the full data set. This implies that the systematic uncertainties in the muon disappearance rate, λ_{μ^-}, should be restricted to 5 s^{-1} for each run 10 and run 11. The combined statistical and systematic precision of the full data set corresponds to a 15 ppm uncertainty in the muon lifetime and a 1.2% uncertainty in Λ_S. This precision will result in a 6.5% determination of g_P. To achieve these results, the systematic uncertainties needed to be reduced by a factor of two with respect to the initial MuCap publication result.

In Section 8.1, the uncertainties of the analysis are compiled, and they are well within the goal. The independent data set with comparable statistics from run 10 has been analyzed using this framework by PDRA Peter Winter, and, as shown in Section 8.2, indicates excellent consistency. The combined data set contains about two times the statistics analyzed in this thesis. The collaboration is finalizing some systematics studies in addition to those addressed in this thesis. Once these studies are completed, the result will be unblinded to extract g_P. Section 8.3 describes the final steps involved in this extraction. Section 8.4 concludes with an outlook of the physics impact of the expected high precision result.

8.1 Uncertainties

Several of the key systematic issues necessary to correctly determine the negative muon disappearance rate were discussed in Chapter 6, and Table 8.1 summarizes the findings. This

Source	Correction (s^{-1})	Uncertainty (s^{-1})	Projected Unc.(s^{-1})	
$\mu + p$ scattering	–	1	1	This work
EH interference	-7.7	1.1	1.1	This work
EL interference	–	0	0	This work
μp diffusion	-2	0.5	0.5	This work
Electron definition†	–	4	3	Collaboration
Pileup efficiency†	–	2	2	Collaboration
high-Z impurities†	-6.5	4	2	Collaboration
Total Systematics	-16.2	6.2	4.4	
Statistics	–	7.4	7.4	This work

Table 8.1: Systematic corrections and uncertainties on λ_{μ^-} for the run 11 analysis. The current estimates for the uncertainties of several parameters are listed in addition to the projected uncertainties when the collaboration finishes the systematic studies (indicated by a †).

table contains two types of terms: corrections and uncertainties. Some effects, such as EH interference, introduce corrections because the distortion to the observed rate is explainable and correctable. Procedural uncertainties are also applied for these effects. Upper limits for other systematic uncertainties are included for effects in which no distortion is directly observed. In the case of $\mu + p$ scattering, the need to correct for the inclusion of muon stops in high-Z materials is eliminated by implementing the cut on NC_{EH}. The uncertainty term for $\mu + p$ scattering in Table 8.1 comes from the limit on the $\mu + p$ scatter events that occupy the $NC_{\mathrm{EH}} = 2$ bin in the data.

The full data set for run 11 has been analyzed, resulting in a statistical uncertainty of 7.4 s^{-1}. The issues of $\mu + p$ scattering, EH interference, EL interference and μp diffusion were directly addressed in this thesis. The systematic issues associated with the electron definition, pileup inefficiency and the high-Z impurity contamination in the gas were summarized in Chapter 6. There are ongoing efforts within the collaboration to finalize the uncertainties associated with these effects, and the corresponding terms are denoted by a † in the table.

8.2 Unblinding

8.2.1 Comparison of Run10 and Run11 Data Collection

This thesis has described the analysis of the run 11 production data. The run 10 data was processed recently in a parallel analysis by Peter Winter after making some fine-tuned adjustments on the cut parameters, relevant for that data set. There are several differences in the data collection for run 10 relative to run 11:

* TPC HV : The TPC operated at a higher voltage (5.45 kV) in run 10 than in run 11 (5.1 kV), which results in higher gain. The tracks are more densely populated.

* Noise: There was considerably less noise in the TPC during run 10 than in run 11.

* ePC2 HV sector: A region of ePC2 that was disconnected during run 11 worked properly during run 10.

* Impurities: The impurity concentrations (N, H_2O) were higher in run 10 than in run 11.

A comparison of the consistency of the observed disappearance rates in run 10 and run 11 serves as an additional cross-check that the analyses have correctly accounted for the systematic effects in the data. Estimates of the remaining systematic corrections and their uncertainties are made independently for each run, and the procedures that will be used to finalize those results have been defined by the analysis team.

8.2.2 Relative Unblinding of μ^- data

The clock frequencies in run 10 and run 11 were chosen independently, so each run has a unique blinding conversion factor. The collaboration agreed to perform a relative unblinding of the two data sets in February 2011. An individual external to the collaboration was entrusted with the task of producing a relative conversion factor so that the two data sets

can be directly compared in a common, blinded space. He reported the ratio of the clock frequencies for run 10 and run 11 to be $r = f_{10}/f_{11} = 1.0011976718$. This ratio is then directly included as a fixed parameter in fits of the run 11 data. This converts the fitted results for run 11 to the blinded space of run 10 by using a fit function analogous to equation (5.4):

$$N(t) = N_0 \cdot w \cdot \lambda \cdot r \cdot e^{(-\lambda \cdot rt)} + B. \tag{8.1}$$

Each run is fit and λ is extracted. The systematic corrections contain small differences between run 10 and run 11. Each set of corrections is applied, and the rates, in the common blinded space, are determined to be:

$$\lambda_{\mu^-}(\text{Run 10}) = 456514 \pm 7.1_{\text{stat}} \pm 10_{\text{syst}}\ \text{s}^{-1} \tag{8.2}$$

$$\lambda_{\mu^-}(\text{Run 11}) = 456521 \pm 7.4_{\text{stat}} \pm 10_{\text{syst}}\ \text{s}^{-1} \tag{8.3}$$

The difference in λ_{μ^-} between run 10 and run 11 is 7 s^{-1} and the statistical uncertainties of each run are comparable. The systematic errors presented here are to be interpreted as the scale of all known and remaining corrections for comparison purposes.[1] The central values may still change based on the exact findings of the final systematic corrections, but should remain within the quoted range. This comparison demonstrates excellent consistency across the wide range of experimental differences outlined above.

Combining both data sets results in a statistical uncertainty of $\delta\lambda_{\mu^-} = 5.1_{\text{stat}}\ \text{s}^{-1}$. Additionally, the systematic uncertainty on λ for each data set will be $\delta\lambda_{\mu^-} \approx 4.4_{\text{syst}}\ \text{s}^{-1}$. Since most of the systematics are correlated between the two data sets, a conservative sum of $\delta\lambda_{\mu^-} \approx 4.4_{\text{syst}}\ \text{s}^{-1}$ is used for the systematic uncertainty of the combined data set.

[1] For example, the high-Z impurity correction is a well defined procedure that will result in a small systematic uncertainty. However, at the time of the unblinding, the precise value of the correction was not determined, so the uncertainties were inflated to cover the range of possible results.

8.2.3 Relative Unblinding of μ^+ data

The same procedure is performed with the μ^+ data. Each run is subdivided into two data sets corresponding to the orientation of the applied magnetic field. The fit contains additional terms for the muon precession as described in Section 3.2. The λ here is reported with a separate analyzer offset, so that it can not be compared with λ_{μ^-} to extract Λ_S:

$$\lambda_{\mu^+}(\text{Run 10 A}) = 455333 \pm 22.5_{\text{stat}} \pm 5_{\text{syst}}\ \text{s}^{-1} \tag{8.4}$$

$$\lambda_{\mu^+}(\text{Run 10 B}) = 455301 \pm 17.3_{\text{stat}} \pm 5_{\text{syst}}\ \text{s}^{-1} \tag{8.5}$$

$$\lambda_{\mu^+}(\text{Run 11 A}) = 455343 \pm 15.4_{\text{stat}} \pm 5_{\text{syst}}\ \text{s}^{-1} \tag{8.6}$$

$$\lambda_{\mu^+}(\text{Run 11 B}) = 455345 \pm 10.3_{\text{stat}} \pm 5_{\text{syst}}\ \text{s}^{-1} \tag{8.7}$$

The corrections are simpler, since there are no capture processes for μ^+ that could distort the observed rates. Additionally, the individual data sets are smaller and the statistical uncertainties dominate. The μ^+ data sets also demonstrate consistency between run 10 and run 11. When unblinded, the μ^+ result will be compared to the world average as a consistency check.

The final unblinding procedure will reveal the clock frequencies for run 10 and run 11 and the two data sets will be refit with the appropriate conversion factors. The analyzers will remove the separate offsets for λ_{μ^-} and λ_{μ^+} and the observed rates will be reported.

8.3 Extraction of g_P

To determine g_P from the observed disappearance rate, a few steps are still required. First, the observed μ^- disappearance rate must be compared to the free muon decay rate. The lifetime method defined the relationship between the capture rate and the disappearance rate in Equation (3.11):

$$\lambda_{\mu^-} \approx \lambda_{\mu^+} + \Lambda_S.$$

For the experimental conditions of MuCap, two additional corrections are applied:

$$\lambda_{\mu^-} = (\lambda_{\mu^+} + \Delta\lambda_{\mu p}) + \Lambda_S + \Delta\Lambda_{pp\mu}. \tag{8.8}$$

The first new term, $\Delta\lambda_{\mu p}$ corrects for the fact that the μ^- is not a free particle, but decays from a bound state. This correction has the well-established value $\Delta\lambda_{\mu p} = -12.3\ \mathrm{s}^{-1}$ [14,63]. The second term accounts for the fact that molecules form slowly in the MuCap target. Although the density of the hydrogen was chosen to suppress the transition to the molecular states, the full treatment requires a small correction to reflect the fact that the μp atoms do not remain purely in the singlet state. The term $\Delta\Lambda_{pp\mu}$ can be computed based on the muon kinetics presented in Section 3.1.1. At the hydrogen density in MuCap, $\phi = 0.011$, $\Delta\Lambda_{pp\mu}$ is given by:

$$\Delta\Lambda_{pp\mu} = -23.5 \pm 4.3 \pm 3.9\ \mathrm{s}^{-1}, \tag{8.9}$$

where the uncertainties are separated to emphasize the individual contributions for the muon chemistry parameters λ_{of} and λ_{op}. A parallel analysis of argon-doped systematic data is nearly complete that will improve the precision of λ_{of}, reducing its contribution to the uncertainty in Λ_S from $4.3\ \mathrm{s}^{-1}$ to $\approx 2.0\ \mathrm{s}^{-1}$. The combined data set systematic uncertainty of $\delta\lambda_{\mu^-} \approx 4.4\ \mathrm{s}^{-1}$ and the updated molecular uncertainties of $2.0\ \mathrm{s}^{-1}$ and $3.9\ \mathrm{s}^{-1}$ yield a total systematic uncertainty of $\delta\Lambda_S = 6.2_{\mathrm{syst}}\ \mathrm{s}^{-1}$. Because the molecular capture rates depend on the value of Λ_S as described in Section 3.1.1, a 3.2% inflation of the uncertainties is required for self-consistency.[2] Thus the uncertainty on Λ_S for the combined run 10 and run 11 data is expected to be

$$\delta\Lambda_S = \pm 5.3_{\mathrm{stat}} \pm 6.4_{\mathrm{syst}}\ \mathrm{s}^{-1}. \tag{8.10}$$

The publication of the run 8 analysis reported $\Lambda_S = 725 \pm 13.7_{\mathrm{stat}} \pm 10.7_{\mathrm{syst}}\ \mathrm{s}^{-1}$, based on the comparison to the decay rate of the positive muon $\lambda_{\mu^+} = 455162.2 \pm 4.4\ \mathrm{s}^{-1}$ [64].

[2] The central value of the $\Delta\Lambda_{pp\mu}$ correction will also change as a function of the MuCap measurement of λ_{μ^-}. The value used here is based on the MuCap run 8 result.

The value of g_P was determined using a procedure similar to the description in Section 2.4: $g_P = 7.3 \pm 1.1$ [14]. Since the publication of this data, the MuLan collaboration has reported a new measurement of the positive muon lifetime with 1 ppm precision: $\tau_{\mu^+} = 2196980.3 \pm 2.2$ ps [8]. This corresponds to a free decay rate of $\lambda_{\mu^+} = 455170.2 \pm 0.46$ s^{-1}, which is an 8 s^{-1} shift from the value previously used to extract g_P. Additionally, the measurement of λ_{μ^+} is so precise that it is no longer an appreciable contribution to the uncertainty of Λ_S. Recomputing g_P in light of this shift yields $g_P = 7.8 \pm 1.1$, bringing the experimental value into even closer agreement with the theoretical predictions of chiral perturbation theory $g_P^{\mathrm{ChPT}} = 8.26 \pm 0.23$.

Accounting for all corrections in Table 8.1, and following the procedure described in equations (8.8) and equation (2.18), MuCap plans to report a new value of Λ_S and g_P:

$$\Lambda_S = \Lambda_S^{\mathrm{MuCap}} \pm 5.3_{\mathrm{stat}} \pm 6.4_{\mathrm{syst}} \text{ s}^{-1}, \tag{8.11}$$

$$g_p^{\mathrm{MuCap}} = g_P^{\mathrm{Theory}} + 92.59 \left(1 - \sqrt{\frac{\Lambda_S^{\mathrm{MuCap}}}{\Lambda_S^{\mathrm{Theory}}}}\right), \tag{8.12}$$

where the contribution to the uncertainty of g_P from the experimental uncertainty $\delta\Lambda_S^{\mathrm{MuCap}}$ is anticipated to be $\delta g_P^{\mathrm{MuCap}} \approx 0.54$.

8.4 Discussion and Outlook

The methods necessary to produce a 7% determination of g_P have been developed and described in this thesis, and the collaboration is anticipating its final unblinding during 2011. The previous MuCap result indicated excellent agreement with the predictions of chiral perturbation theory, and with the anticipated uncertainty of $\delta g_P^{\mathrm{MuCap}} \approx 0.54$ on the final result, a precise comparison with theory is possible. The lack of sensitivity to λ_{op} makes the interpretation of such a comparison unambiguous. This is essential in order to clarify the long-standing controversial experimental situation with respect to this weak nucleon form

factor. As the predictions for g_P rest on the basic symmetries of low energy QCD, their understanding will be directly probed by this measurement of the singlet capture rate Λ_S and determination of the proton's pseudoscalar coupling.

Appendix A

Glossary

The words, phrases and acronyms that are commonly used throughout this document are listed below.

anode-only	ePC definition requiring only an anode cluster and no cathode information.
BNL	Brookhaven National Laboratory.
b_{pair}	The distance of closest approach between the reconstructed electron vector and the muon stop location.
BR	Branching Ratio.
Bragg peak	The peak in the dE/dx curve for low energy muons stopping in the hydrogen gas.
cathode-AND	ePC definition requiring a three-fold coincidence between a cluster in the anode plane and a cluster in each of the two cathode planes.
cathode-OR	ePC definition requiring a three-fold coincidence between a cluster in the anode plane and a cluster in either of the two cathode planes.
χ^2	The chi-square is a goodness of fit parameter that parametrizes how well a fit hypothesis represents the data.
χ^2/NDF	The χ^2 of a fit divided by the number of degrees of freedom.
χ^2_{track}	The χ^2 of the linear fit to the muon track.

ChPT	Chiral Perturbation Theory. An effective field theory that reflects the chiral symmetry of QCD. ChPT constructs a systematic, low-energy expansion in orders of q/Λ_χ, when the external momenta, q are small compared to the scale of chiral symmetry breaking, Λ_χ.
CHUPS	Circulating Hydrogen Ultra-High Purification System. A continuous filtering system which reduced elemental impurities in the hydrogen gas during data collection.
CVC	Conserved Vector Current. A hypothesis equating the vector current in the weak interaction to the vector current in the electromagnetic interaction.
DAQ	Data acquisition. The set of hardware, electronics and computers that are used to record the data from the detectors.
DRU	Deuterium Removal Unit. The DRU is used prior to data collection to remove isotopic impurities from the protium gas via a cryogenic distillation column.
EH	High energy threshold applied to the TPC analog signals. This corresponds to the peak in the dE/dx distribution at the end of the muon track.
EL	Low energy threshold applied to the TPC analog signals. This is set just above noise such that the charge deposition from the ionization track created by the incoming muon triggers it.
ePC	Electron Projection Chamber. Wire chambers that record spatial information about the outgoing electron.
eSC	Electron Scintillating counter. A segmented cylindrical detector that records the time of the outgoing electron. Used with the ePCs to form a hodoscope for electron tracking.

EVH	Very high energy threshold applied to the TPC analog signals. This is set well above EH and corresponds to the nuclear recoil energy of rare muon captures on high-Z impurities in the gas.
FNAL	Fermi National Accelerator Laboratory or Fermilab.
h_{track}	The track head. h_{track} is the length of the line segment that extends beyond the stop location in the muon track.
High-Z	Refers to any element other than hydrogen.
Hit	A hit is a signal generated by a discriminator corresponding to an event above threshold in a counter.
Kicker	A beamline element that uses an electrostatic field to deflect the incoming muon beam during the measurement period.
l_{track}	The length of the fitted track in anode space.
λ_{op}	The transition rate between the ortho- and para-molecular states.
$\lambda_{pp\mu}$	The molecular formation rate.
λ_{μ^-}	The disappearance rate of negative muons in the hydrogen target.
λ_{μ^+}	The decay rate of positive muons (or free negative muons).
Λ_S	The capture rate of μp atoms in the singlet hyperfine spin configuration.
Measurement period	The 25 μs period immediately after the arrival of the muon when decay electrons are detected. The kicker suppresses the beam during this period.
MORE	Muon On REquest is a mode of operating the kicker. A signal is observed in the μSC counter and a logic unit triggers the deflection of the kicker to prevent subsequent muons from entering the target for a 25 μs period.
MuCap	Muon Capture Experiment.

μPC	Muon Projection Chamber. The μPC is a wire chamber that images the incoming muon beam.
μSC	Muon Scintillating Counter. The μSC is a scintillator that records the times of the incoming muons.
MWPC	Multiwire Proportional Chamber.
NC_{EH}	Number of continuous EH anodes at the end of the muon track.
NCSA	National Center for Supercomputing Applications at the University of Illinois.
NPL	Nuclear Physics Laboratory at the University of Illinois.
OMC	Ordinary Muon Capture. $\mu^- + p \rightarrow n + \nu_\mu$.
Pixel	A pixel is generated in the TPC when a TDC discriminator is over threshold for a specific anode (cathode) at a specific TDC digitization time-slice. Pixels are shown in the event display. The pixels can be mapped to a physical location $(\mathrm{anode}, t) \leftrightarrow (z, y)$ and $(\mathrm{cathode}, t) \leftrightarrow (x, y)$.
PCAC	Partially Conserved Axial Current.
PMT	Photomultiplier tube.
ppb	Part per billion.
ppm	Part per million.
Protium	Hydrogen with one proton and no neutrons, depleted of deuterium and tritium isotopes.
PSI	The Paul Scherrer Institut. In Villigen, Switzerland, PSI is the location of the MuCap experiment.
QCD	Quantum Chromodynamics. A quantum field theory that describes the interaction between color-charged particles (quarks, gluons) and gluons, the force carrier of the strong interaction.

QED	Quantum Electrodynamics. A quantum field theory that describes the interaction between electrically charged particles and photons, the force carriers of the electromagnetic interaction.
RMC	Radiative Muon Capture. Similar to OMC with an additional γ produced. $\mu^- + p \rightarrow n + \nu_\mu + \gamma$.
ROI	Region of interest. The 25 μs time window after an accepted muon entrance.
Tail	The tail is the set of pixels leading up to a muon stop location.
TPC	Time Projection Chamber. The TPC is the imaging target which records spatial and temporal information about the incoming muon's stop location.
V-A	Vector minus axial vector coupling of the weak interaction.

Appendix B

Analysis Supplement

B.1 Noise

The MWPCs in the MuCap experiment occasionally experience noise events that overwhelm the physics signals. These events are caused by discharges that affect all detector systems. The cuts on these high-multiplicity events are described in Section 6.5. In addition, the following procedure is implemented to address a specific type of noise on a small number of TPC anodes.

Throughout the run, some anodes in the fiducial volume developed significant levels of noise. Figure B.1 shows an example event display in which anode 40 contains many extra pixels. The track finder groups these spurious hits on the noisy anode along with the main muon track. Problems arise when the linear fit produces a poor χ^2 and the fitter tries the two-line fit method. The noisy anode is viewed as a second line segment extending from the muon stop location, and artificially large track head values are recorded.

Section 6.5 demonstrated the dangers of cutting events based on noise on anodes 1-4. Therefore, it is important to mitigate the effects of the observed noise on the anodes without cutting events. To address this problem, a hit profile of the anodes is determined on a run-by-run basis. During a good run, most anodes have a similar number of hits. The number of hits that are unused in the muon track is plotted as a function of run and anode in Figure B.2a. The TPC electronics is divided into five sectors, and each sector has a common threshold, tuned separately. If an anode contains > 5 times the average number of hits compared to the rest of its sector during a given run file, it is subsequently masked during

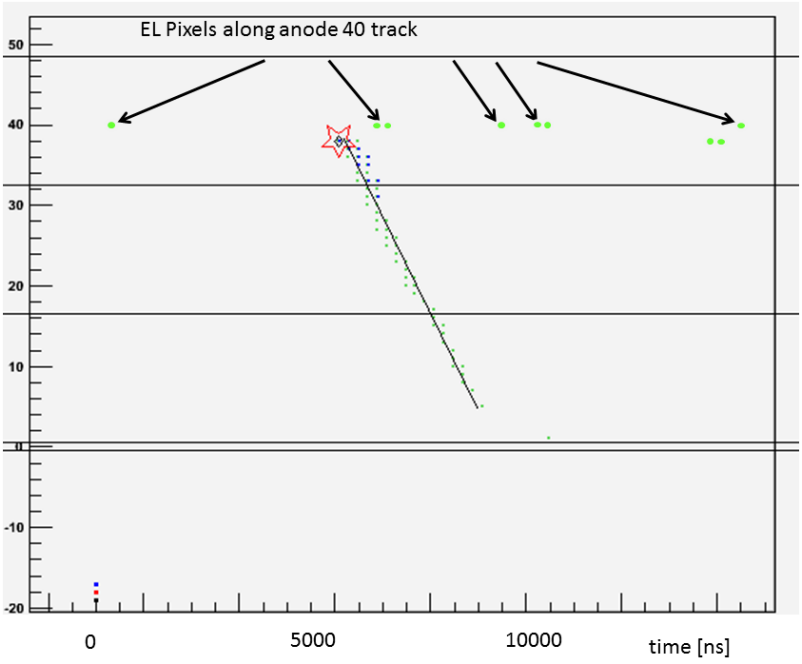

Figure B.1: TPC event display. Noise is present on anode 40 throughout the ROI, and is unrelated to the muon track.

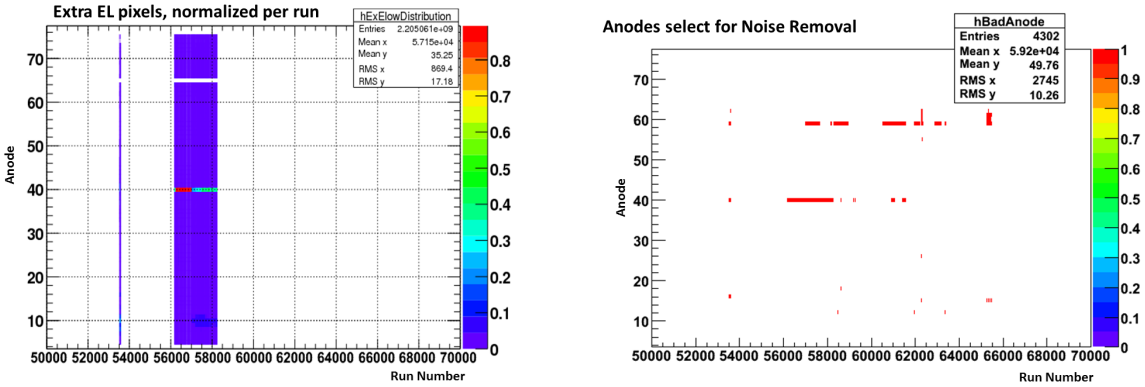

(a) (b)

Figure B.2: Distributions used to identify noisy anodes. (a) For a subset of the data, a 2-D histogram of the normalized hits vs. anode vs. run is displayed. In this subset of the data, anode 40 was very noisy in the region around run 56000, accounting for nearly 90% of the unused pixels in the TPC. (b) A distribution of the anodes that are identified as outliers from (a). Anode 40 and anode 59 contain the most noise, and are suppressed in the track fitting on a run-by-run basis.

the track fitting for that run. The noisy anode is still used in the island finding, but the pixels do not contribute to the χ^2 of the one- and two- line fits. Figure B.2b shows the distribution of anodes that were masked during run 11 in this manner.

This compromise between using and ignoring the pixels on the noisy anodes allows the pixels to contribute to the track finding if the hits are real, without pulling the fit or penalizing its χ^2 if the hits are spurious.[1] The noise does not distort the result, but it causes the analysis to call the computationally-expensive advanced track fitting algorithms. Studies confirm that this method of masking the noisy anodes does not distort the observed disappearance rate.

B.2 Next-nearest-neighbor Algorithm

The next-nearest-neighbor algorithm is typically employed when identifying clusters of pixels in a MWPC plane. A pixel is generated when a discriminator is over threshold on a given wire at a given time. Figure B.3 shows a schematic representation in pixel space for a seed pixel (blue square). The immediate neighbors (green circles) and next-neighbors (green triangles) are added to the cluster containing the seed pixel. The algorithm then treats any newly added pixels as seeds. The procedure terminates when no more neighbors or next-neighbors exist.

B.3 Fitting the Cosmic Background

During the analyses of the previous data set, Clayton [60] and Banks [61] observed the presence of cosmic rays in the data. The procedure they developed to address the cosmic rays is briefly summarized here.

The presence of the cosmic rays is clearly visible in the run 11 data. Figure B.4 shows

[1] This method is very similar to masking a noisy wire in the analysis and splicing together the other sections of the TPC. However, it is preferable to leave the anode in place, in case hits are not detected.

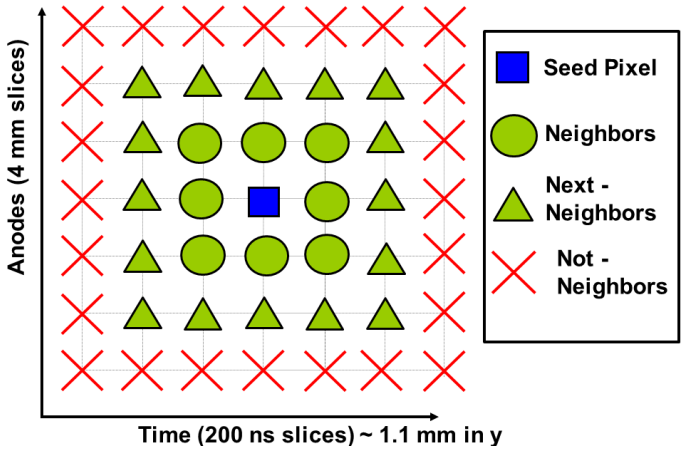

Figure B.3: A schematic representation of the TPC pixels is depicted. A seed pixel is represented by a (blue) square. The neighbors are depicted by the (green) circles, and the next-neighbors are depicted by the (green) triangles. Any of these pixels would be grouped together as part of one muon track. In the absence of an appropriate neighbor or next-neighbor pixel, the pixels that contain a (red) X would not be grouped with the seed pixel.

the distribution of B/N in the λ vs eSC segment plots. The highest background rates are for the horizontally oriented elements (1, 8, 9 and 16) and the lowest for the vertically oriented elements (4, 5, 12 and 13), as defined in Figure 5.11.

The cosmic background is uniform with respect to the muon arrival, so the decay spectrum acquires an additional background term B_{cosmic} which can be absorbed into the background term in the fit function described in equation (5.4): $B = B' + B_{\text{cosmic}}$. The existence of the cosmics in the data is not inherently problematic for the fitted λ. However, since the cosmics can penetrate two independent eSC elements, two separate electron tracks are sometimes formed and potentially paired with a muon arrival. This leads to an underestimate of the errors of each bin. When the contents of a bin are independent, the error of that bin i with N_i events is expressed $\sigma_i = \sqrt{N_i}$.

The analysis identifies that $\approx 50\%$ of the background comes from through-going cosmics. The errors on each bin are then adjusted to account for the artificially inflated background counts, B_i: $\sigma_i \rightarrow \sqrt{N_i + 0.5 \cdot B_i}$. In practice, the fits require two iterations. The first

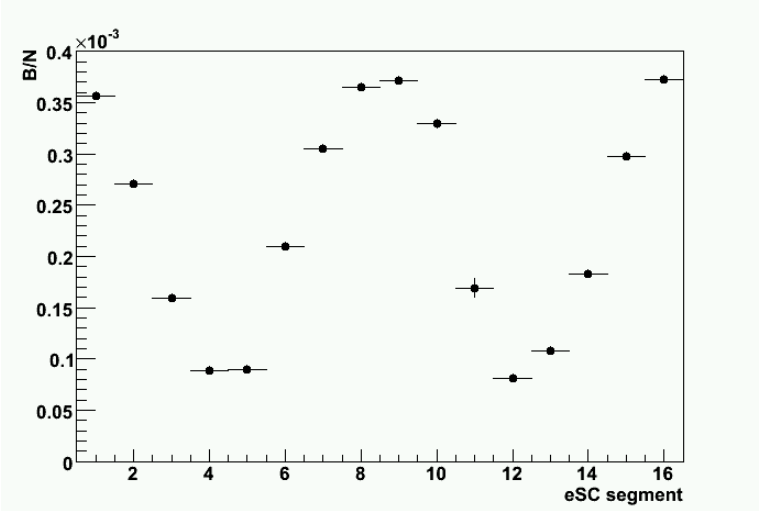

Figure B.4: The ratio of the fitted background to the number of hits for a subset of the data. A cosmic background is clearly evident, with the elements with a vertical normal vector having a higher cosmic flux. The cosmic component of the background is estimated and the individual bin errors on the decay spectrum are increased to account for the correlated hits.

iteration determines the flat background. The second iteration adjusts the errors and refits the data. Adjusting the bin errors to account for the double counting of the cosmics decreases the χ^2/NDF of the fit without affecting λ. The cosmic fraction was varied and λ remains stable.

B.4 Electron Definition

Section 6.6 discussed the consistency of λ with respect to the electron definition for an impact parameter requirement $b_{\text{pair}} \leq 120$ mm, which is the standard cut tracking requirement imposed in the analysis. Additional studies are ongoing to estimate the final uncertainty contribution based on the consistency with respect to the electron definition. One promising approach investigates the effect of tightening the impact parameter to reduce the contribution of background events. The same plots that were shown in Figure 6.20 are reproduced here for $b_{\text{cut}} = 60$ (Fig. B.5) and for no impact parameter cut (Fig. B.6).

Comparing panel (d) of these figures demonstrates the improved agreement between the

electron definitions for tighter impact parameter cuts. If a tighter impact parameter cut is ultimately imposed, a different μp diffusion correction will need to be applied, as described in Section 6.3.

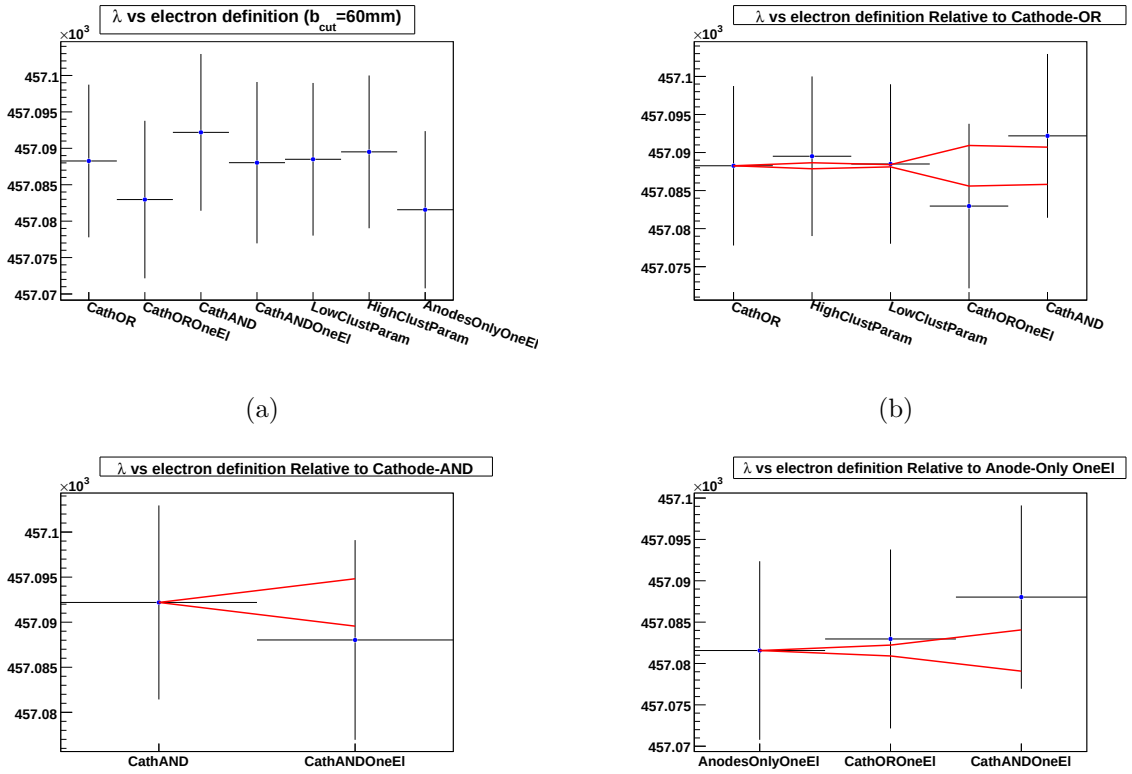

(a) (b)

(c) (d)

Figure B.5: Consistency of λ vs electron definition for $b_{\text{cut}} = 60$ mm. (a) The variations in the electron definition are shown. (b) The allowed deviation relative to the cathode-OR standard definition are indicated in red. "OneEl" imposes a constraint that only one electron track is present. "HighClustParam" and "LowClustParam" correspond to variations in the ePC track clustering parameters, and a slightly higher dependency is observed than for $b_{\text{cut}} = 120$ mm. "CathAND" adds the condition that a cluster is found in both cathode planes and is close to the statistically allowed deviation. (c) The one-electron condition is shown for the cathode-AND data and the allowed deviation is shown in red. (d) The one-electron condition is shown relative to the least restrictive anode-only definition. The deviation is smaller than for $b_{\text{cut}} = 120$ mm.

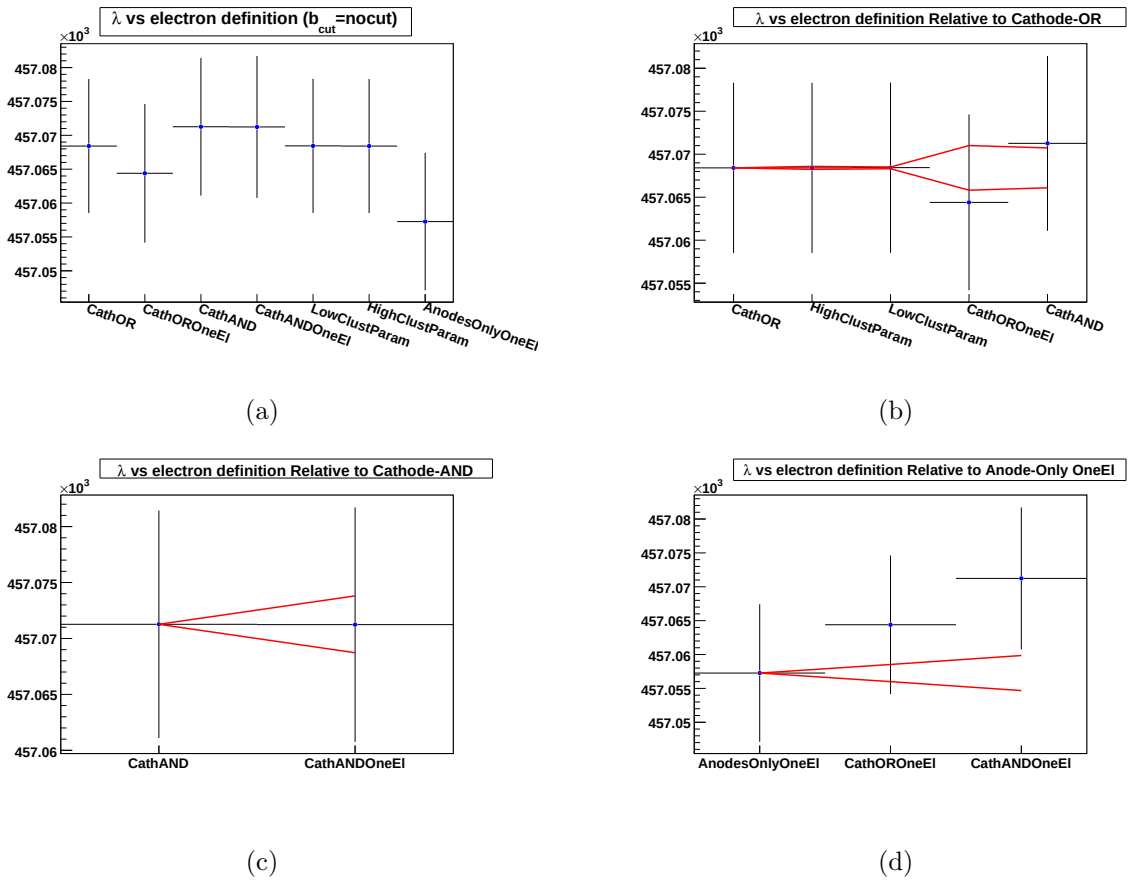

(a) (b)

(c) (d)

Figure B.6: Consistency of λ vs electron definition for no impact parameter cut. (a) The variations in the electron definition are shown. (b) The allowed deviation relative to the cathode-OR standard definition are indicated in red. "OneEl" imposes a constraint that only one electron track is present. "HighClustParam" and "LowClustParam" correspond to variations in the ePC track clustering parameters, and no dependency is observed. "CathAND" adds the condition that a cluster is found in both cathode planes and the agreement with "CathOR" is good. (c) The one-electron condition is shown for the cathode-AND data and the data points are perfectly consistent. (d) The one-electron condition is shown relative to the least restrictive anode-only definition. The deviation is significantly larger than for $b_{\text{cut}} = 60$ mm and larger than $b_{\text{cut}} = 120$ mm.

References

[1] C. D. Anderson and S. H. Neddermeyer. Cloud chamber observations of cosmic rays at 4300 meters elevation and near sea-level. *Phys. Rev.*, 50(4):263–271, 1936.

[2] H. Yukawa. On the interaction of elementary particles I. *Progress of Theoretical Physics Supplement*, 1:1–10, 1955.

[3] R. E. Marshak and H. A. Bethe. On the two-meson hypothesis. *Phys. Rev.*, 72:506–509, 1947.

[4] M. Gell-Mann (subject) and G. West (interviewer). *The state of physics at MIT (Part 1)*, 1997. http://www.webofstories.com/play/10576.

[5] M. Riordan. *The Hunting of the Quark: A True Story of Modern Physics*. Simon and Schuster, Inc., New York, NY, 1987.

[6] K. Nakamura et al. The review of particle physics (PDG). *J. Phys. G*, 37:75021, 2010.

[7] D. H. Frisch and J. H. Smith. Measurement of the relativistic time dilation using μ-mesons. *American Journal of Physics*, 31:342–355, 1963.

[8] D. M. Webber et al. Measurement of the positive muon lifetime and determination of the fermi constant to part-per-million precision. *Phys. Rev. Lett.*, 106(4):041803, 2011.

[9] W. J. Marciano. Fermi constants and "new physics". *Phys. Rev. D*, 60(9):093006, 1999.

[10] T. Gorringe and H. W. Fearing. Induced pseudoscalar coupling of the proton weak interaction. *Reviews of Modern Physics*, 76:32 – 82, 2004.

[11] P. Kammel and K. Kubodera. Precision muon capture. *Annual Review of Nuclear and Particle Science*, 60(1):327–353, 2010.

[12] A. Czarnecki, W. J. Marciano, and A. Sirlin. Electroweak radiative corrections to muon capture. *Phys. Rev. Lett.*, 99:032003, 2007.

[13] J. H. D. Clark et al. Ortho-para transition rate in μ-molecular hydrogen and the proton's induced pseudoscalar coupling g_p. *Phys. Rev. Lett.*, 96:073401, 2006.

[14] V. A. Andreev et al. Measurement of the muon capture rate in hydrogen gas and determination of the proton's pseudoscalar coupling g_p. *Phys. Rev. Lett.*, 99(3):032002, 2007.

[15] M. Raidal et al. Flavour physics of leptons and dipole moments. *Eur. Phys. J.*, C57:13–182, 2008.

[16] C. Amsler et al. The review of particle physics (PDG). *Physics Letters B*, 667, 2008.

[17] G. W. Bennett et al. Final report of the muon e821 anomalous magnetic moment measurement at BNL. *Phys. Rev.*, D73:072003, 2006.

[18] R. M. Carey et al. The new (g-2) experiment: A proposal to measure the muon anomalous magnetic moment to ± 0.14 ppm precision. *DOE proposal*, 2010. http://gm2.fnal.gov/public_docs/proposals/Proposal-APR5-Final.pdf.

[19] E. de Rafael. Present status of the muon anomalous magnetic moment. *Nuclear Physics B: Proceedings Supplements*, 186:211–217, 2009.

[20] A. Romanino and A. Strumia. Electron and muon electric dipoles in supersymmetric scenarios. *arxiv:hep-ph/0108275v2*, 2001.

[21] T. Mori et al. Search for $\mu^+ \to e^+\gamma$ down to 10^{-14} branching ratio. *PSI proposal*, 1999. http://meg.web.psi.ch/docs/prop_psi/proposal.pdf.

[22] J. Hisano and D. Nomura. Solar and atmospheric neutrino oscillations and lepton flavor violation in supersymmetric models with right-handed neutrinos. *Phys. Rev. D*, 59(11):116005, 1999.

[23] R. H. Bernstein et al. Proposal to search for $\mu^- N \to e^- N$ with a single event sensitivity below 10^{-16}. 2008.

[24] A. de Gouvêa, S. Lola, and K. Tobe. Lepton-flavor violation in supersymmetric models with trilinear r-parity violation. *Phys. Rev. D*, 63(3):035004, 2001.

[25] J. E. Sonier et al. New muon-spin-rotation measurement of the temperature dependence of the magnetic penetration depth in $YBa_2Cu_3O_{6.95}$. *Phys. Rev. Lett.*, 72(5):744–747, 1994.

[26] R. Pohl et al. The size of the proton. *Nature*, 466:213–215, 2010.

[27] P. Mohr, B. Taylor, and D. Newell. CODATA recommended values of the fundamental physical constants: 2006. *Reviews of Modern Physics*, 80, 2008.

[28] *Muon Colliders*. http://map.fnal.gov/muon-collider/research-goals.shtml.

[29] K. Gnanvo et al. Detection and imaging of high-Z materials with a muon tomography station using gem detectors. *arXiv:1011.3231v2*, 2010.

[30] K. Nagamine et al. Probing magnetism in human blood by muon spin relaxation. *Physica B: Condensed Matter*, 374-375:444 – 447, 2006.

[31] K. Grotz and H. V. Klapdor. *The Weak Interaction in Nuclear, Particle and Astrophysics*. IOP Publishing Ltd, Bristol, England, 1990.

[32] C. S. Wu et al. Experimental test of parity conservation in beta decay. *Phys. Rev.*, 105(4):1413–1415, 1957.

[33] V. Bernard., L. Elouadrhiri, and U. Meissner. Axial structure of the nucleon. *J. Phys. G: Nucl. Part. Phys.*, 28:R1–R35, 2002.

[34] S. Ando, F. Myhrer, and K. Kubodera. Ordinary and radiative muon capture in liquid hydrogen reexamined. *Phys. Rev. C*, 65(4):048501, 2002.

[35] V. Bernard, T. R. Hemmert, and U. G. Meissner. Ordinary and radiative muon capture on the proton and the pseudoscalar form factor of the nucleon. *Nucl. Phys. A*, 686, 2001.

[36] S. Ando, F. Myhrer, and K. Kubodera. Capture rate and neutron helicity asymmetry for ordinary muon capture on hydrogen. *Phys. Rev. C*, 63:015203, 2001.

[37] G. Bardin et al. A novel measurement of the muon capture rate in liquid hydrogen by the lifetime technique. *Nuclear Physics A*, 352:365–378, 1981.

[38] A. Alberigi-Quaranta. Muon capture in gaseous hydrogen. *Physical Review*, 177:2118–2132, 1969.

[39] R. Hildebrand. Observation of μ^- capture in liquid hydrogen. *Phys. Rev. Lett.*, 8:34–37, 1962.

[40] E. Bleser et al. Muon capture in liquid hydrogen. *Phys. Rev. Lett.*, 8:288–290, 1962.

[41] J. S. Cohen. Slowing down and capture of negative muons by hydrogen: Classical-trajectory monte carlo calculation. *Phys. Rev. A*, 27(1):167–179, 1983.

[42] Nucleonica Wiki. http://www.nucleonica.net/wiki.

[43] D. D. Bakalov, M. P. Faifman, L. I. Ponomarev, and S. I. Vinitsky. μ-capture and ortho-para transitions in the muonic molecule ppμ. *Nuclear Physics A*, 384(3):302 – 322, 1982.

[44] T. Suzuki et al. Total nuclear capture rates for negative muons. *Physical Review C*, 35:2212–2224, 1987.

[45] A. Adamczak and J. Gronowski. Diffusion radius of muonic hydrogen atoms in h-d gas. *Eur. Phys. J. D*, 41(3):493–497, 2007.

[46] W. M. Yao et al. The review of particle physics (PDG). *J. Phys. G*, 33, 2006.

[47] W. J. Marciano. Muonium lifetime and heavy quark decays (lessons learned from muonium). *arXiv:hep-ph/0403071v1*, 2004.

[48] D. V. Balin et al. High precision measurement of singlet $p\mu$ capture in H_2 gas. *PSI proposal R-97-05*, 1996.

[49] PSI website. http://www.psi.ch/science/large-scale-facilities.

[50] M. J. Barnes and G. D. Wait. A 25-kV 75-kHz kicker for measurement of muon lifetime. *Plasma Science, IEEE Transactions on*, 32(5):1932 – 1944, 2004.

[51] D. M. Webber. A part-per-million measurement of the positive muon lifetime and a determination of the fermi constant. PhD thesis, University of Illinois at Urbana-Champaign, 2010.

[52] J. Egger et al. The 10 bar hydrogen time projection chamber of the MuCap experiment. *Nucl. Instrum. Meth. A*, 628:199–203, 2011.

[53] I. Alekseev et al. Deuterium removal unit for the mucap experiment. Presented at the NHA Annual Hydrogen Conference, Sacramento, 2008.

[54] M. Suter et al. Advances in particle identification in ams at low energies. *Nuclear Instruments and Methods in Physics Research Section B: Beam Interactions with Materials and Atoms*, 259(1):165 – 172, 2007. Accelerator Mass Spectrometry - Proceedings of the Tenth International Conference on Accelerator Mass Spectrometry.

[55] V. A. Ganzha et al. A circulating hydrogen ultra-high purification system for the MuCap experiment. *Nucl. Instrum. Meth. A*, 578:485–497, 2007.

[56] V. A. Andreev et al. Muon capture on the deuteron – the MuSun experiment. 2010.

[57] MIDAS website. http://midas.psi.ch.

[58] J. R. Klein and A. Roodman. Blind analysis in nuclear and particle physics. *Annu. Rev. Nucl. Part. Sci.*, 55:141–163, 2005.

[59] P. Kammel. Private communication, 2010.

[60] S. M. Clayton. Measurement of the rate of muon capture in hydrogen gas and determination of the proton's pseudoscalar coupling. PhD thesis, University of Illinois at Urbana-Champaign, 2007.

[61] T. I. Banks. A measurement of the rate of muon capture in hydrogen gas and determination of the proton's induced pseudoscalar coupling g_P. PhD thesis, University of California, Berkeley, 2007.

[62] M. Hildebrandt. Private communication, 2009.

[63] H. Überall. Decay of μ^- mesons bound in the k shell of light nuclei. *Phys. Rev.*, 119(1):365–376, 1960.

[64] D. B. Chitwood et al. Improved measurement of the positive muon lifetime and determination of the fermi constant. *Phys. Rev. Lett.*, 99:032001, 2007.